Synthesis of Amorphous Oxide Electrolyte Nanoparticles for All-Solid-State Battery by Induction Thermal Plasma

王, 怡冉

出版情報：Kyushu University, 2023, 博士（工学）, 課程博士
バージョン：
権利関係：

Synthesis of Amorphous Oxide Electrolyte Nanoparticles for All-Solid-State Battery by Induction Thermal Plasma

令和五年度　博士論文

九州大学大学院工学府 化学システム工学専攻

第 5 講座 WANG YIRAN

Contents

1. Introduction

1.1 General Introduction of Plasma

Solid transform into liquid after heating and further become gas with continuous heating. The gas would be ionized upon further heating and finally form into plasma. Plasma consists of ions, electrons, atoms, and molecules. Plasma is sometimes called the "fourth state of matter" [1].

Plasma occurs commonly in nature. The most known matter in the universe is the ionized state, namely, many known matters exist as plasma in the universe [2]. The solar corona, solar wind, nebula, polar, and earth's ionosphere are considered plasma. **Figure 1.1** shows the domains of plasma as the function of temperature and electron density. Irving Langmuir introduced the term plasma for the first time. He thought the ionized gas near electrodes contains ions and electrons in about equal numbers except for the sheaths, which leads to the space charge being very small. Furthermore, he suggested using plasma to describe the balanced charges of ions and electrons [3]. Not any ionized gas can be called plasma from the suggestion of Irving Langmuir, because quasineutral is a significant index. Therefore, the definition of plasma shows the following: A plasma is a quasineutral gas of charged and neutral particles exhibiting collective behavior [1]. Benjamin Franklin conducted a significant experiment to verify the plasma formed in nature with lighting. This interesting experiment also illustrates people's strong interest in plasma.

Plasma also can be generated in the laboratory easily with various methods current, called man-made plasma. Plasma can be produced by direct current (DC), alternating current (AC), or radio frequency (RF) sources at high pressure (> 10 kPa). The plasma temperature can achieve a relatively high level around $2\times10^3 \sim 2\times10^4$ K with electron densities ranging from 10^{21} to 10^{26} cm^{-3}. Above plasmas are characterized by high energy density and equality between heavy particles (T_h) and electrons (T_e) temperature. These plasmas are called thermal plasma or equilibrium

plasma [4,5].

Another type of plasma is cold plasma or non-equilibrium plasma because this plasma is not thermodynamic equilibrium and $T_e > T_h$. The temperature range of heavy particles is from 298 K to 373 K, while the electrons have much higher temperature from 5000 K to 10^5 K [6]. Meanwhile, non-equilibrium plasma systems are in most cases operated at low pressures (< 10 kPa) and have lower electron density from 10^9 to 10^{10} cm^{-3}. Most electrons have kinetic energy below 20 eV. Glow discharge and low pressure RF discharge are common measures to obtain cold plasma [7,8]. **Figure 1.2** presents the typical ranges of electron temperature rang with electron density for non-equilibrium and equilibrium plasma.

There is a wide application of plasma, such as coating, waste treatment, metallurgy, and material synthesis, in the industry owing to their unique superiorities. However, the hydrodynamics, complex electric and magnetic fields lead to plasma becoming a complicated subject. Therefore, further and continuous study of plasma is necessary both for theoretical research and commercial applications.

1.2 Thermal Plasma

1.2.1 Complete Thermal Equilibrium

There are temperature dependencies that exist in an ideal thermal plasma, such as excited states of atoms, ionization degree, electron density and internal heat exchange by radiation. Complete thermodynamic equilibrium (CTE) is a significant index for ideal thermal plasma [9]. The velocity and energy distribution of particles in thermal plasma conform to Maxwell-Boltzmann distribution:

$$f_j = n_j \left(\frac{m_j}{2\pi \mathrm{K} T}\right)^{3/2} \exp\left(-\frac{m_j v^2}{2\mathrm{K} T}\right) \tag{1-1}$$

where n_j and m_j are number density and mass of particle of j, respectively. Boltzmann constant is presented as K. T and v represent temperature and velocity, respectively. Simultaneously, the number density of heavy particles in the excited state also satisfies the Boltzmann distribution. The excitation temperature is same for all excited states and equal to the temperature in Maxwell distribution. There is a relationship between number density of particles in different states:

$$\frac{n_i}{n_j} = \frac{g_i}{g_j} \exp\left(-\frac{\Delta E}{\mathrm{K}T_{ex}}\right) \tag{1-2}$$

here, n_i and n_j represent the number density of particles in an upper i and lower state j. g_i and g_j are the statistical weights, respectively. Energy difference between i and j state is presented as ΔE, excitation temperature is presented as $T_{ex.}$

Number density of particles in thermal plasma should satisfies law of mass action during chemical reactions process, such as dissociative-recombination reactions and ionization-recombination reactions. The law can be described as Saha Equation in gas ionization reactions:

$$\frac{n_{r+1} n_e}{n_r} = \frac{2z_{r+1}}{z_r} \frac{(2\pi m_e \mathrm{K}T_{reac})^{3/2}}{\mathrm{h}^3} \exp\left(-\frac{E_{r,i}}{\mathrm{K}T_{reac}}\right) \tag{1-3}$$

where n_r and n_{r+1} are the number density of particles in the r-th and $(r+1)$-th state of ionization, z_r and z_{r+1} are the partition function of two particles; $E_{r,i}$ is the ionization energy and T_{reac} is the ionization temperature; m_e and h are electron mass and Planck constant, respectively. Ionization decrease should be considered in high temperature and high number density. Similar equation for atom dissociation reactions also can be obtained according to above. In thermal equilibrium, T_{reac} is the temperature of dissociation and has the same value for all possible reactions involved. Simultaneously, T_{reac} equals T_j in Maxwell distribution and T_{ex} in Boltzmann distribution.

The electromagnetic radiation for thermal plasma is obeyed the Planck law of black body radiation, namely the relationship between radiation intensity B_v and frequency f is described as the following equation:

$$B_v = \frac{2h\nu^3}{c^2} \frac{1}{\exp\left(\frac{h\nu}{KT_{rad}}\right)} - 1 \quad (1\text{-}4)$$

where c is the speed of light and T_{rad} is the black body radiation temperature. There is a relationship among the temperature in complete thermal equilibrium plasma which is presented as following:

$$T_h = T_e = T_{ex} = T_{reac} = T_{rad} \quad (1\text{-}5)$$

Actual thermal plasma is difficult to satisfy above requirements, especially for the electromagnetic radiation. The measured radiation intensity of thermal plasma is much lower than black body radiation intensity because plasma cannot be treated as black body with the broad wavelength region. Plasma even is treated as optically thin, that is the plasma cannot absorb radiation. Hence, the T_{rad} would lower than other temperature in plasma. Besides, thermal conduction, thermal convention and diffusion of vapor components also lead to the deviation of thermal equilibrium in plasma.

1.2.2 Local Thermal Equilibrium

Laboratory and industrial plasma are difficult to achieve the complete thermal equilibrium, local thermal equilibrium (LET) is introduced to describe the thermal plasma. Plasma can be treated as optically thin in LET which is different from CTE, that is, plasma radiation intensity does not equal black body radiation intensity at the same temperature. The LTE can be achieved by energy state transition and chemical reactions in thermal plasma dominated by collision. A detailed equilibrium exists between the collision process and its reverse process. The temperature and concentration gradient also should be relatively low in order to allow the LET. The temperature in thermal plasma should follow the relationship:

$$T_e = T_h = T_{ex} = T_{reac} \quad (1\text{-}6)$$

The Maxwell distribution, Boltzmann distribution and Saha equation are still available. Hence, the process in thermal plasma except radiation is still temperature depended. The plasma should be kept at relatively higher level of number density (> 10^{23} m^{-3}) and vapor pressure (≥1 atm), aiming to achieve the high collision frequency between electron and heavy particles.

1.2.3 Thermal Plasma Generation

Arc discharge and high frequency inductive coupling discharge are the main methods to generate thermal plasma with temperature over 10^4 K in laboratory. Microwave discharge and laser heating are other common methods [4].

I. Direct Current Arc Plasma

Arc discharge is considered a convenient method to generate thermal plasma. The arc consists of arc column, cathode region, and anode region. The arc column occupies a temperature as high as 10^4 K and is electrically neutral, showing a thermal plasma state [10]. The arc for thermal plasma generation has a high current density which can reach 10^7 ~ 10^8 A/m^2. Arc plasma is usually generated at atmosphere pressure, the energy that electron obtains from electric field is much lower than gas ionization energy. Thus, the gas ionization mechanism for plasma is thermal ionization rather than field ionization.

Cathode and anode region take account of small percentage of the arc volume and are not electrically neutral. There are two types of electrodes for direct current (DC) arc plasma generator. The mental, such as tungsten, with high melting point is used as cathode called thermionic cathode. Electrons thermionically emit from the cathode and enter anode which is usually made by graphite passing through arc column. The arc plasma generator with thousands of watts or tens of kilowatts always uses thermionic cathode [11]. Another type is called non-thermionic cathode, the cathode

and anode are made of the same material which the mental has high thermal conductivity and low melting point. Temperature-aided emission is considered the electron emission theory. The high-power plasma generator always selects non-thermionic cathode [12].

The DC arc plasma generators can work as following method. **Figure 1.3(a)** shows the first form which the cathode and anode are inside of the plasma generator, the plasma flows out of the generator after gas is heated by the inside arc. This type of arc is called non-transferred arc and is usually utilized in plasma spray and arc gas heaters [13,14]. **Figure 1.3(b)** shows another generator which the inside anode only assists with arc generation. The workpiece would be worked as the main anode during the working. Arc welding, plasma cutting and non-ferrous metal melt are the main application of this arc which is named transferred arc.

Free-burning arc is a simple gaseous discharge contrasted to above two types because there is no limitation in it. The interaction of arc current and its magnetic field lead to the induced plasma jet in high-intensity arc region of variable cross section. The gas surrounding cathode is drawn by the electromagnetic filed and ejects to anode region. A stagnation layer would be formed in front of anode, then the free-burning arc with bell is formed [15]. The free-burning arc only can be stable in the short distance between cathode and anode. **Figure 1.3 (c)** shows the diagram of free-burning arc. Welding, arc furnaces, switchgear, and arc heaters are important industrial applications for free-burning arc [16].

II. Alternating Current Arc Plasma

The power supply for arc generation can use alternating current (AC) besides DC. The arc power source affects the polarity of the electrical current that runs through the electrode. The AC arc is more efficient and reliable in contrast to DC arc. Because it does not need to utilize AC-DC

current rectification which takes accounts for around 30% of the overall capital and operation cost of most plasma installations [17].

Multiphase AC arc is the most major part of AC arc, its schematic diagram is presented in **Fig. 1.3(d)**. There are several arcs coexist in a large discharge chamber volume, which leads to a large arc volume. Meanwhile, the multiphase alternating current also allows the continuous plasma even during the zero-current crossing. Above advantages promise the multiphase AC arc is treated as an appropriate method in waste treatment, pyrolysis, gasification, and nanoparticle synthesis [18–21].

III. Radio Frequency Induction Thermal Plasma

The plasma generated by arc is polluted by metal due to the erosion and melting of electrodes, which negatively influences plasma application to some extent [22–25]. Radio frequency (RF) thermal plasma can offer a pure environment owing to coupling discharge [26,27]. The electrons move in an opposite direction in opposite periods of alternating electric field, the length that electron moves in a half period can be obtained. The electron in discharge region would collide with other particles instead of arriving at electrodes, when the distance between two electrodes over this length. The discharge can be maintained in a situation that provides additional electric filed, simultaneously, electrode can locate outside of discharge tube [1].

Capacitive coupling is one of the methods to generate RF plasma, the anode and cathode exist out of discharge tube. The advantage of capacitive coupling is maintaining discharge under relative lower power. While the plasma generated by capacitive coupling discharge is non-thermal plasma [28,29].

Thermal plasma is always generated by inductive coupling discharge due to its high efficiency. The plasma generated by this method is called RF induction thermal plasma. Reed reported that

thermal plasma was generated with atmosphere pressure and flow gas first time in 1961 [27]. The RF induction thermal plasma has already been widely used in various fields, such as spraying, nanoparticle synthesis and spectrum analysis [30–33]. The torch consists of a quartz tube and copper coil, the diagram is shown in **Fig. 1.3(e)**. The power supply offers high frequency current passing through the coil, which leads to magnetic field generation. This magnetic field would be couple with the plasma in the quartz tube. The sheath gas injects into plasma torch would be conductive after ignition. The excitation current which passes through coils would produce an alternating magnetic field, further leading to the alternating electric field. The current would be generated in the conductive gas in the quartz tube and produce Joule heat. The thermal plasma can be maintained with the appropriate discharge conditions, meanwhile, the continuously injecting cold gas is heated to form thermal plasma [27]. Since RF induction thermal plasma is electrodeless discharge and has a flexible atmosphere (Ar, He, H_2, O_2 and N_2), it is treated as an ideal method to produce material with high purity and heating sample for spectrum analysis [34,35].

Skin effect is a basic process of screening out electromagnetic fields by plasma. Skin depth is a significant index for induction thermal plasma and expressed as:

$$\delta = (\pi \xi_0 \sigma f)^{-1/2} \tag{1-7}$$

where δ is skin depth, ξ_0 is magnetic permeability. The conductivity σ is 2700 S/m around 10^4 K for Ar plasma. The δ is around 1.53 mm and 5.6 mm for f is 4 MHz and 3MHz, respectively. Skin depth decreases with frequency increase based on the above results, simultaneously, plasma Joule heat would concentrate on the narrow region when frequency increase. Coupling effect would be optimal when the discharge radius is 1.5 times skin depth according to experience [4,36]. The ratio of discharge radius to coil radius is another index for coupling efficiency, the enhanced efficiency can be obtained at higher value [37].

The minimum power to maintain discharge is affected by frequency, generator diameter, and gas pressure. Low frequency and large diameter result in high minimum power, high vapor pressure has the same effect. Argon is an excellent candidate to ignite induction plasma because of its lowest minimum power value. Mixture plasma can be obtained by injecting other gas into Ar plasma after ignition.

IV. Microwave Plasma

Microwave discharge also plays a critical role in thermal plasma generation. There is a wide range in pressure and frequency of microwave plasma. The microwave plasma can be sustained with frequency from 1 MHz to 10 GHz, the discharge pressure ranges from 10^{-3} Pa to hundreds of kPa [38]. Electrons are also responsible for energy absorption from electric field same as arc and coupling discharge. The low pressure microwave discharge (< 10 kPa) would generate non-thermal plasma. Because the kinetic equilibrium deviation is caused by poor collision between electrons and heavy particles [39]. Thermal plasma can be obtained at high pressure conditions (> 10 kPa). Electromagnetic surface wave and traveling wave discharge are two selections for microwave plasma devices, the latter is stable, reproducible and quiescent contrasted to the former [40,41].

1.2.4 Thermal Plasma Application

Advanced technology always drives advanced productivity. Thermal plasma technology as an efficient and progressive method has a wide application in industry and daily life ascribing to its unique superiorities. The application mainly focuses on two areas: material processing and treatment of waste. Several mature sciences with considerable economic activity have already been established for material processing. The object of waste treatment is recovering the products

with higher added value and decomposing the toxic wastes in the waste treatment region [42]. Specific details will be described in the following.

I. Metal Melting and Remelting

Thermal plasma is used as an effective source for heating process, the metal can be melted under inert gas atmosphere (He or Ar) with a wide pressure range. The maximum temperature can be over 15000 K which allows metal and alloy to melt totally. Meanwhile, the evaporation of metal and alloy can be inhibited under plasma process, and enhance the possibility of complex alloy material synthesis. A wide range of plasma process is possible and mature technology has already been applied to industry [43,44].

Metallurgical industry is one of the important applications of plasma melting. High concentration and thermal efficiency, excellent heat and mass transfer, and adequate residence time allow transferred arc device to be utilized in metallurgy widely. Synthesis of high purity synthetic silica, ultrafine high purity ceramic powders and production of high purity titania slag from ilmenite have already been achieved [45–47].

II. Plasma Cutting and Welding

Plasma cutting is a melting process that cuts through electrically conductive materials by accelerated jet of hot plasma. Arc would be generated between cathode and the workpiece which is used as the anode. Recombination of particles takes place when plasma hits the workpiece and emits heat simultaneously [48]. The workpiece would be melted by emitted heat and gas flow ejects it from the cut [49]. Argon, nitrogen, or mixture of Ar and H_2 are the common plasma generation gas for cutting. Inert gas prefers to cut workpieces made of reactive alloys. In addition, the inert gas can be replaced by air, the cathode material also should be replaced by hafnium or

zirconium [50]. Compressed air is more competitive to cut carbon-manganese and stainless steel up to 20 mm contrasted to oxygen-fuel cutting [51]. The subject of plasma cutting is various, such as aluminum and its alloy, nickel and its alloy, and titanium. These materials cannot be cut by oxygen-fuel cutting due to the low satisfactorily [52,53]. Robert M. Gage developed this cutting method in 1957 which promoted material processing to great extents.

The arc is formed between a pointed tungsten cathode and the workpiece which is used as anode during plasma welding process. The plasma arc is separated from the shielding gas because the electrode is placed within torch body. Coalescence is produced by the heat from the arc. Inert gas is utilized during this welding for plasma generation or shielding the arc plasma [48,54]. Robert M. Gage developed this method in 1953 and allowed the precision operation on both thin and thick metals.

III. Plasma Spraying Coating

Plasma spraying technology is a coating process in which material melted by thermal plasma is sprayed on the surface of workpiece. This technology allows thin coating (from several to 20 mm) formation and high rate deposition on a large area contrasted to conventional fabrication methods, such as electroplating, physical and chemical vapor deposition. There is a wide range of coating material options, especially for the high melting point material, owing to the high temperature of thermal plasma [55]. Metal, alloys ceramic, plastic, and composition are all available for coating material [56]. The material particles are fed into the torch and heated to melting state, then accelerated towards to substrate. The whole spraying process is the accumulation of numerous sprayed particles. The surface of substrate is in low temperature state, which can achieve flammable substrate coating [57,58].

This technology appeared in the 1960s and was developed in the 1980s due to plasma torch improvement. Simultaneously, plasma spraying was devoted to implementation of robust sensors which work in hard environments. Now plasma spraying is mainly applied to processing high-added value coatings [59].

IV. Plasma Spheroidization and Densification

Spherical particles have lots of superiorities in industry applications. The sphere state improves powder flowability, increases powder packing density, eliminates particle internal cavities and fractures, changes surface morphology, and enhances powder purity [60]. Hence, spherical particles are ideal options for various industry fields, such as powder metallurgy and thermal spraying. The RF induction thermal plasma is considered an efficient method for spheroidization because the high temperature and long residence time promise particles evaporate completely [61]. Particles coalesce faster than coagulate and spherical particles are formed at high temperature during particle growth [62]. The high temperature ensures that spheroidization and powder densification occur simultaneously. Agglomerates are injected into thermal plasma and form densified powder after sintering. There is a wide range of subjects from metals (eg. W, Mo) to high technology ceramics. Plasma densification costs less time, restrains grain growth and tailor heat transfer compared to conventional method, which provides more possibilities to obtain sintered particles with desirable structure [5].

V. Waste Treatment

Waste treatment is another critical application in thermal plasma besides material processing. Since conventional methods for waste treatment, such as landfills and ocean dumpsites, become less and less available, searching for new methods is urgent. Incineration has been utilized

increasingly due to most waste is combustible [63]. However, this method results in plenty of fossil fuel consumption and hazardous gas and slag production, which means no complete treatment of waste [64].

Thermal plasma provides a controlled heat source to melt feedstock and to maintain a high temperature molten bath. The high temperature allows chemical bond destruction and substance vaporization, which decreases slag production. Moreover, thermal plasma treatment also achieves energy production and recuperation of by-products during processing [65]. Namely, waste can be regarded as a green energy source. The synthetic gas which is consisted of H_2 and CO can be obtained from municipal solid waste during the plasma treatment [66,67]. This synthetic gas is more easily to achieve completed combustion compared to methane, simultaneously, also can be used to generate electricity [68]. Waste gas treatment of acetylene production by thermal plasma has already been a commercial application [69].

VI. Nanoparticle Synthesis

The research and development at the atomic, molecular, or macromolecular scales are defined as nanotechnology. Nanoparticles that have a diameter of less than 100nm are the most important component for nanotechnology [70]. The properties of material consisting of nanoparticles are different with their bulk and molecular material owing to their tiny size, in particular for electronic, magnetic, optical, biomedical, catalytic, and energy [71–75]. Therefore, nanoparticle synthesis is a field that attracts people's attention. Biological synthesis, co-precipitation, thermal decomposition and reduction, micelle synthesis, hydrothermal synthesis, and laser pyrolysis technique are common methods to obtain nanoparticles [76–78].

Thermal plasma is used to synthesize nanoparticles due to the high chemical reactivity, high enthalpy, and steep temperature gradient [79]. Furthermore, thermal plasma also allows

spheroidization and densification simultaneously. Above superiorities indicate thermal plasma is a promising method to obtain nanoparticles with better morphology and narrow size distribution. **Figure 1.4** is the diagram of nanoparticles synthesized by thermal plasma. Various nanoparticles have already been synthesized by thermal plasma and more details will be described in the following.

1.3 Synthesis of Nanoparticle by Thermal Plasma

Thermal plasma is applied widely as an efficient and advanced fabrication method of nanoparticles. Different types of nanoparticles are synthesized by different thermal plasma according to their respective properties to ensure the high quality of products.

1.3.1 Method for Synthesis of Nanoparticles

I. Transferred DC Arc Plasma

Transferred DC arc plasma considered an efficient heat source is widely utilized in metal nanoparticles with a diameter of less than 50 nm synthesis [80]. The chemical composition of electrode is same as the target material for this device, the arc plasma is generated by evaporating electrode directly. In addition, most of target material can be used as electrode for transferred DC arc plasma torch. These situations lead to the application of transferred DC arc plasma spreading rapidly. A series of research related to generation rate of nanoparticles and physical properties of electrode was conducted [81]. Sixteen metals are selected as electrodes and the experiment results indicate that Mn, Ag, and Al are easy to obtain nanoparticles, while Mo, Ta, and W are difficult to form into nanoparticles. According to experiment results and thermodynamic calculations, the research concludes that the driving force of nanoparticle generation relates to vaporization heat and melting point of metal. Meanwhile, adding diatomic gas, such as N_2 and H_2, benefits to metal

vapor generation. Further research also investigates the morphology of electrode, revealing spherical shape has a positive on evaporation [82].

II. Non-transferred DC Arc Plasma

The consumption of electrode during nanoparticle synthesis process in transferred arc plasma results in the discontinuous fabrication. Non-transferred DC arc plasma torch is introduced to solve this problem. Different from transferred arc the electrode in this setup is only for generating and maintaining thermal plasma. The raw material is injected into thermal plasma flame during plasma process [83]. The injection port is usually located in the torch exit, which is similar to plasma spraying device [84]. However, this results in the evaporation of raw material incomplete, further influencing the quality of fabricated nanoparticles negatively. Some researches show that the raw material particles are far from a full evaporation state in non-transferred arc torch [85].

III. Multiphase AC Arc Plasma

The DC power supplies are used to generate DC arc plasma, this situation requires converting AC power to DC power. Conversion from AC to DC results in higher energy cost [86]. Synthesis of nanoparticles by AC arc plasma attracts lots of interest in order to achieve the goal of energy saving. The AC arc plasma can be generated directly by the AC power. Single-phase and three-phase are two usually utilized power supplies. However, the intermittent discharge caused by the polarity transition results in a momentary zero current [20]. The synthesis process is limited by the zero current, further affecting the nanoparticle quality. Multiphase AC arc plasma is introduced aiming to improve this problem. The advantages of multiphase AC arc plasma, such as high energy efficiency, large plasma volume, low gas velocity, and low cost, allow it

appropriate for synthesize large amounts of nanoparticles [87]. While the erosion of electrodes would pollute the synthesized nanoparticles and decrease the purity of products.

IV. Induction Thermal Plasma

Ratio frequency induction thermal plasma attracts lots of attention because it can prevent incomplete heating of raw material and also can eliminate electrode pollution. Different from arc discharge, RF plasma discharge is generated by coupling instead of electrode discharge. In addition, the larger plasma flow and continuous discharge also contribute to unit and spherical nanoparticle generation [80]. Electrodeless discharge offers an ideal environment for high purity nanoparticle synthesis. The unique structure of RF plasma torch allows axial injection of raw material alone the centerline, which leads to more effective heating. The RF induction thermal plasma is popularized rapidly in nanoparticle fabrication according to above description, and various products with high performance have already been obtained [88,89].

1.3.2 Nanoparticles synthesis by thermal plasma

I. Metal

Properties change would occur when metal particle diameter decreases to less than 50 nm because of the size effect [80]. Since the electron confinement of metal particles increases with diameter decrease, new properties are observed with the metal to insulator transition [90].

Iron nanoparticles offer very potent magnetic and catalytic properties, while their systematic research is difficult to conduct until the advanced fabrication method occurs [91]. Nanoscale Fe particles have already been synthesized by RF thermal plasma [92]. The raw material with diameter ranging from 25 μm to 37 μm was injected into thermal plasma because full evaporation can be achieved by Fe particles with this diameter range [93]. The size of fabricated nanoparticles

is 6 ~ 12 nm with different feed rates and residence time. Increased feed rate and residence time lead to larger particle synthesis. Prepared nanoparticle morphology was also detected by electron microscopy. Three typical types of morphology are observed, they are spherical, rhombic dodecahedral bounded by twelve (110) planes, and octahedron-shaped, respectively. Particles with different morphologies are collected from different locations in the synthesis device, which indicates the temperature distribution and residence time affect structure of fabricated nanoparticles to some extent.

Silver nanoparticles were synthesized by DC arc thermal plasma successfully [94]. Silver nanoparticles are widely used in antimicrobial and electronics as a versatile material [95,96]. The plasma reactor consists of tungsten cathode and graphite crucible for holding metallic silver block. The fabricated sliver nanoparticles have a cubic (*fcc*) structure according to XRD spectrum. Crystallite size estimated by Scherer formula is around 25 nm. The TEM images reveal that there is no agglomerate condition in product and the size distribution is from 20 nm to 150 nm. This variation in diameter has a positive effect on thick film technology because the small particles can be used as “neck joints” for large particles.

There is an obvious increase in burn rate and detonation properties for Al particles with a size scale decrease from micro-scale to nano-scale [97]. In addition, passivation is an integral step for Al nanoparticle fabrication due to the reactivity of Al. Conventional method allows synthesized Al nanoparticles expose to air to slow oxidation to form thickness Al_2O_3 coating layer. However, this oxide layer impairs Al nanoparticle properties. Organic passivating layer can enhance powder properties in energetic system application [98]. Passivation Al nanoparticles with organic coating were fabricated by transferred arc thermal plasma [99]. The diameter of fabricated nanoparticles is around 27 nm, the oxide percentage decreases to 3% which is much lower than powder obtained from other methods. The organic layer is identified by FTIR analysis.

Multi-layer ceramic capacitors (MLCCs) play an important role in current society. Extensive application has already been achieved by Ni-base electrode-MLCC rather than Pd-base electrode MLCC. The volumetric capacitance which relates to stacking number and capacitive area of electrolyte layers is an index for MLCC property. The properties of Ni nanoparticles can affect above indices according to research [100]. Nickle nanoparticles were fabricated by inductivity coupled thermal plasma with different feeding rates and quenching rates successfully [101]. The raw material was selected as $Ni(OH)_2$ micro-powders with a mean size is 17 μm. Physical phase transition and chemical reaction occur simultaneously during plasma process. Fabricated nanoparticles show a tinier diameter with quenching gas injection with a mean value of 30 nm. The products show well spherical morphology without quenching gas.

The complex reaction environment results in lots of uncertainty during plasma process, especially for induction thermal plasma. The synthesis process is affected by particle number density, diameter and specific surface. Understanding more details of the synthesis process benefits nanoparticle synthesis and further application. Quenching gas flow rates and powder feed rates effect were investigated by numerical simulation, the Al, Ti, Au and Pt are selected as subjects [89,102]. These researches indicate that, for all metals, the enhanced quenching gas flow rates lead to particle number density and specific surface increase while the mean diameter decrease. Moreover, the higher powder feed rates cause larger mean diameter and smaller specific surface.

II. Alloy

Alloy nanoparticles evoke lots of interest because of their tunable optical, electronic and catalytic properties over a broad range by adjusting element composition [103]. Thermal plasma as an efficient fabrication method is applied to alloy nanoparticle synthesis.

Nano-scaled magnetic alloy is widely used as smart dampers, drug delivery vehicle, degradation catalyst, magnetic storage device and microwave shielding [104,105]. Magnetic property is sensitive to alloy composition. Iron nickel alloy nanoparticles with different iron percentages (from 25% to 75%) were synthesized by transferred DC arc thermal plasma [106]. Since nucleation and particle growth occur at high temperature, the disordered phase (*fcc*) γ-FeNi is obtained. Poor crystallinity is observed in Fe-rich nanoparticles. Diameter range of products from 20 nm to 40 based on TEM images. High crystallinity leads to high saturation magnetization and the best magnetic performance is shown in $Fe_{0.5}Ni_{0.5}$.

Another promising candidate for magnetic material is Fe-Co alloy which owns high saturation magnetization, large permeability, and low coercivity [107]. Conventional fabrication methods, such as polyol, thermal decomposition, and sol-gel, are difficult to wash the surfactants completely from the surface of as-synthesized nanoparticles. This situation impairs the magnetization per total mass [108]. Induction thermal plasma can improve this problem. A series of Fe-Co alloy nanoparticles have already been prepared by a new induction thermal plasma setup, namely, low oxygen induction thermal plasma. The new setup allows nanoparticle fabrication under inert gas atmosphere, further achieving direct synthesis of bare metal particles [109,110]. The experiment results show that the diameter of products is around 90 nm and all products present a low oxygen degree.

The unique superiorities of induction thermal plasma are attributed to novel alloy nanoparticle synthesis, especially appropriate to rare-earth alloy nanoparticle synthesis. The Sm-Co alloy was synthesized successfully by low oxygen induction thermal plasma as a permanent magnet material [111]. The property evaluation of permanent magnet material is based on remanent magnetization and coercivity, these indices are controlled by the microstructure of material. In addition, high coercivity can be achieved by particle diameter refinement [112]. The Sm-Co alloy can be used

as permanent magnet material according to the report, simultaneously, this alloy can acquire high coercivity by high anisotropy field of Sm-Co [113,114]. Micrometer scale raw material with molar ratio 5:1 was injected into Ar plasma. The synthesized nanoparticles have a spherical morphology and the mean size is 61 nm.

III. Oxide

Oxide nanoparticles, especially metal oxide nanoparticles, are attractive for a large variety of applications including bactericidal agents, catalysis, sensors, optoelectronic material, and environmental remediation [115–117]. There are various metal oxide nanoparticles have already been acquired by DC thermal plasma and RF induction thermal plasma.

Copper oxide nanoparticles show good antibacterial and have already been synthesized by thermal plasma [118]. Atomic compositions for Cu and O are calculated as 54.18% and 45.26% based on EDS results, respectively. This is because there are few Cu and Cu_2O nanoparticles existed as by-products. Prepared nanoparticles show a diameter range from 22.4 nm to 94.8 nm. The TEM images indicate the CuO nanoparticles have an approximate equi-axes shape with no sharp edges. Simultaneously, almost all particles have only one unique grain.

Nanosized alumina attracts attention ascribing to its application in engineering ceramics, catalysts, semiconductor packing materials and eco-materials. Aluminum powders were selected as raw material, nanosized Al_2O_3 particles were synthesized after Ar-O_2 RF induction thermal plasma processing [119]. Feed rate was fixed at 1667 mg/min and radial quenching gas was injected from shoulder of reactor. The experiment results demonstrate that smaller nanoparticles with narrower diameter distribution are synthesized by enhanced quenching gas flow rates. However, excessive quenching rates impair nanoparticle growth.

Titanium dioxide nanoparticles are known as function material and they are utilized in sun protection creams, textile fibers and wood preservatives, have already been synthesized by induction thermal plasma [62]. Ilmenite was selected as raw material because of its the low-price and easily obtain. The raw material is evaporated completely in high temperature area, then vapor phase reactions occur. The TiO and FeO vapor are synthesized at first, the TiO_2 and $(FeO)_2(TiO_2)$ liquid are formed with the temperature decrease. These tiny droplets would be solidified in lower temperature region and finally form nanoparticles. Since the weight of TiO_2 nanoparticles is lighter than nanoparticles containing Fe, the particles collected from the top of chamber are considered TiO_2. The XRD spectra indicate the phase of products are anatase and rutile TiO_2.

Partially shielded 4*f*-orbital of rare earth oxides attracts much attention. Gate dielectrics and photo catalytic application lead to Nd_2O_3 nanoparticles being used in industry in order to improve the electrical properties [120]. Micro-sized $Nd(OH)_3$ powders were injected into center of Ar plasma plume by Ar. The XRD spectra indicate that the product is hexagonal Nd_2O_3. Morphology of products was detected by TEM and the images show the prepared nanoparticles exhibit a faceted morphology with good uniformity in size and shape. All particles are smaller than 100 nm and most particles are around 20 nm although the product has a wide diameter range.

IV. Nitride

Titanium nitride nanoparticles have a wide application in various regions, such as composition material production, nanostructured coating, mechanical property improvement of alloy and metal [121]. Nanosized TiN particles have already been synthesized by DC arc thermal plasma [122]. Single-phase TiN nanoparticles were obtained after sedimentation. Titanium hydride with size range from 1μm to 100 μm were injected into thermal plasma, nitrogen was used to generate plasma. Micro-sized and nano-sized particles are obtained simultaneously. Micro scale particles

contain TiN, Ti_6O and Ti based on XRD spectra. These particles have a laminar structure on surface. This resulted from the insufficient residence time of molten titanium nitrogenation. Nano-sized particles show the single phase, identifying as TiN based on the XRD spectra. The experiment results also indicate that decreasing diameter of raw material would allow more TiN nanoparticles synthesis. The mean size of TiN nanoparticles is around 20 nm.

The iron-nitrogen system has been studied for a long time due to its remarkable mechanical and magnetic property. Recently, this research focuses on iron nitride nanoparticles because of the high saturation magnetization and high coercivity [123]. Moreover, the FeN nanoparticles are also used as the precursors for γ-FeN_x which has "giant magnetic moment" [124]. Iron nitrides nanoparticles were prepared by RF thermal plasma [125]. Iron powder with size lower than 10 μm was injected into thermal plasma by Ar, argon and hydron were used as sheath gas to generate plasma. Nitrogen and ammonia were used as nitrogenization source. The results show there two phases exist in product, the α-phase and γ-phase present the 55 nm and 27 nm diameter, respectively.

Aluminum nitride nanoparticle attracts interest ascribing to its high intrinsic thermal conductivity, high electrical insulation and similar thermal expansion coefficient to silicon [126]. Purity of AlN nanoparticle is an important index for their property. Ratio frequency induction thermal plasma is an ideal method for fabrication of AlN nanoparticle with high purity because of the electrodeless discharge. Spherical Aluminum powder with 3 ~ 8 μm size distribution was selected as the raw material. Nitrogen was used as sheath gas and nitrogenization source. The experiment results reveal that AlN nanoparticles are synthesized successfully, while a few Al remains as by-product. The percentage of by-product would decrease with N_2 flow rate and input power increase, meanwhile, the reduced reaction pressure also benefits high purity of product.

V. Boride

Titanium boride nanoparticles have already been synthesized by RF induction thermal plasma successfully [127]. There is a wide application of titanium boride nanoparticles in physics, chemistry and engineering, including electromagnetic shielding, wear-resistant coating, solar control windows interaction with IR and UV lights. The TiB_2 nanoparticles show better properties than TiB based on the research [128]. However, the high melting point of raw material results in a dilemma about the synthesis of phase controlled TiB_2 nanoparticles with high purity using conventional methods. The high temperature and electrodeless discharge of RF induction thermal plasma provide an ideal method for TiB_2 nanoparticle fabrication. The difference between nucleation B and Ti leads to the feed rate becoming an important index. The mass fraction of TiB_2 decreases with feed rate increase in the boron-rich condition, while the boron-poor condition presents an opposite tendency.

The increasing demand for industrial applications in information storage, magnetic fluids and catalysts lead to the research interest in cobalt boride nanoparticles, in addition, cobalt borides also play a significant role in hydrogen storage and fuel cells [129]. Colloidal synthesis is a common method to obtain cobalt boride nanoparticles, however, there are still some challenges, such as the cleaning of liquid colloidal, complex operation, and high costly. Cobalt boride nanoparticles were synthesized by the RF induction thermal plasma with C/B mole ratio of 1, 2 and 3 [130]. The synthesized CoB and Co_2B nanoparticles have a diameter range from 18 nm to 22 nm. Enhanced feed rate leads to more CoB and Co_2B nanoparticles generation, meanwhile, this also leads to larger diameter of products.

Nickel boride and tungsten boride nanoparticles were also prepared by DC arc thermal plasma [131]. The former is regarded as an efficient catalyst for selection reduction of halides and nitro compounds [132]. The latter has a potential application in rock milling and mining because of its

superior hardness [133]. The experiment result demonstrates that exposure time in high temperature region affects crystallinity. Lower crystallinity is observed in nickel boride because the Ni has a lower nucleation temperature. While the higher nucleation temperature of W provides longer condensation time of W and B, further the higher crystallinity is achieved.

VI. Carbide

The high melting point, great hardness, good mechanical stability, and low work function allow ZrC nanoparticles to become an advanced ceramic and to apply in mechanical and nuclear industry [131,132]. Common fabrication methods, such as self-propagating high temperature synthesis, mechanical alloying and reaction sintering, cannot produce ultrafine powders with high purity. Nanosized ZrC particles were synthesized by RF induction thermal plasma successfully [135]. The $ZrCl_4$ was used as raw material. Sheath gas was a mixture of CH_4 and H_2, where CH_4 was also carbon source. Conversion rate of ZrC rises with H_2 flow rate increase, all synthesized nanoparticles smaller than 100 nm.

Titanium carbide nanoparticles were synthesized by induction thermal plasma [136]. The TiC nanoparticle is widely used for cutting tools, polishing paste, abrasive, and wear-resistance material because of its high melting point, high hardness, and good thermal conductivity [137,138]. Titanium dioxide is used as raw material for conventional synthesis methods for TiC nanoparticles. The product size is affected by raw material size to great extents, namely, nanosized TiC is synthesized by nanosized TiO_2. There is no such size limitation in thermal plasma synthesis. Carbon source and raw material were CH_4 and Ti powder, respectively. Experiment results indicate all TiC nanoparticles are smaller than 100 nm, enhanced input power benefits TiC synthesis. Simultaneously, the feed rate should be lower than 5 g/min and molar ratio of Ti/CH_4 should be set as 1.

Tungsten carbide is regarded as a candidate in refractory and anti-corrosion material ascribing to its high melting point, high hardness, and excellent wear resistance [139]. Simultaneously, it would show good catalyst property when size reduces to nanoscale [140]. It is difficult to obtain uniform size distribution particles using common methods, such as ball milling and spray conversion process. Tungsten carbide nanoparticles prepared by DC thermal plasma can improve above dilemma [141]. Multi-wall carbon nanotubes, amorphous carbon and CH_4 can be used as carbon source, the molar ratio of W/C was fixed at 2/3. The experiment results demonstrate that the main product is W_2C and WC, by-product is WC_{1-x}. The main product transforms from W_2C to WC_{1-x} with W/CH_4 molar ratio increase.

VII. Silicide

Metal silicide nanoparticles exhibit a wide application in electronic, magnetic, optical, catalyst and mechanical properties with different constitute metals, stoichiometries and crystal structures [142]. Since the high melting point of raw material, metal silicide nanoparticles are always synthesized by high-temperature methods [143]. Thermal plasma satisfies the high temperature demand completely. Formation mechanism of different metal silicide nanoparticles has already been studied computationally, four systems, Cr-Si, Co-Si, Ti-Si, and Mo-Si, were selected as the subjects [144,145]. The simulation results demonstrate that the product particle size is around 10 nm and the silicon content is related to nucleation and condensation phase.

Saturation pressure and precursor fraction effect on synthesized metal silicide nanoparticles were also studied computationally [114,146]. The small difference in saturation vapor pressure for metal and silicon can lead to a narrow range in composition because of the almost simultaneous co-condensation of metal and silicon. In addition, a huge gap in saturation vapor pressure results in a greater time lag for co-condensation for metal and silicon during particle

growth process. The greater time lag for co-condensation further results in a wide range of composition in product.

VII. Amorphous

Amorphous hydrogenated carbon nitride film is used as wear-resistant film for coating magnetic disks [147]. Common fabrication method is chemical vapor deposition. However, the film property is closely related to deposition processing. Power feed, gas pressure, gas flow rate, and substrate bias and temperature influence the final result to great extents [148]. The RF thermal plasma can improve above problems. Nitrogen and methane are used as N and C sources, respectively. Optical emission spectra indicate that the CN peak is observed in N_2-CH_4 plasma. Increasing N_2 in gas mixture can suppress C_mH_n species and enhance CN and CHN species. The experiment also reveals that CN and CNH species would not influence film growth directly.

Spherical particles of ternary metal oxide show lots of desirable application, such as photoluminescence, microwave application and optical property [149]. Amorphous alumo-silicate nanoparticles with spherical morphology have already been prepared by RF thermal plasma [150]. Mixture of SiO_2, Al_2O_3 and KOH was injected into thermal plasma, the molar ratio of Si/Al and K/Al was fixed at 4 and 1, respectively. There is an obvious amorphous peak in XRD spectra, simultaneously, the crystalline peaks belonging to Al_2O_3 and SiO_2 are also detected. Composition of products was identified by EDS, showing that peaks of Al, Si, K and O were all detected. Spherical morphology of prepared particles was observed by TEM and SEM.

Amorphous Si nanoparticles are believed as a reliable strategy to improve cycling performance in lithium ion batteries due to volume variation. Microscale Si powder was fed into induction thermal plasma with 250 mg/min, argon used as counter quenching gas was injected into reaction chamber to enhance quenching rate during plasma process [151]. The XRD spectra reveal SiO_2

and crystalline Si are also synthesized as by-products besides amorphous Si. Amorphous degree increases with quenching gas flow rate increase, while the mean diameter of product shows an opposite tendency. Simultaneously, the agglomerate percentage also witnesses a growth with quenching gas flow rate increase.

Amorphous lithium compounds are treated as a candidate for solid electrolytes. The high lithium content is necessary in order to achieve high ion conductivity and energy density. Mechanical milling and sol-gel are common methods to obtain amorphous nanoparticles with high Li content. However, time-consuming and complex operation put a dilemma during fabrication process. Induction thermal plasma which is characterized by rapid quenching rate, large volume, and electrodeless discharge is considered an ideal method to prepare amorphous high Li content compounds with high purity.

Amorphous LiSiPON nanoparticles were fabricated by induction thermal plasma, particle spheroidization was achieved simultaneously [34]. Mixture of Li_2O, Si_3N_4, $Li_4P_2O_7$ and Li_4SiO_4 was injected into thermal plasma, argon and nitrogen was used to generate plasma. Stoichiometry of LiSiPON amorphous nanoparticles is investigated by EDS, confirming as $Li_{2.8}Si_{0.8}P_{0.2}O_{2.5}N_{0.66}$.

1.4 All-Solid-State Battery

There is an increasing demand for clean energy in current society because of the energy crisis and carbon neutrality. Electricity is a promising replacement for fuel owing to its high efficiency and environment friendly. Lithium ion battery is the most widely used storage device in industry and daily life. While the rapid development of electric vehicle and flammability of lithium ion battery urges the pursuit of high energy density and safe battery. Recently, the research point transforms to all-solid-state battery (ASSB) which all the battery material is solid state. Especially,

the electrolyte is solid state instead of liquid. The difference between Li ion battery and ASSB is presented in **Fig. 1.5 (a)**.

The high energy density can be achieved by ASSB because of the solid state battery material in ASSB. The relationship between volumetric and gravimetric energy density for different batteries is shown in **Fig. 1.5 (b)**. Moreover, the Li ion battery also exists a serious safety issue. The lithium dendrites grown during cycling causes the short current of battery and finally results in an explosion. Moreover, liquid electrolyte would be decomposed over 300 K and release flammable gas. These limitations of liquid electrolyte lead to a narrow battery safety window that is lower than 4V. No leakage and non-flammable in ASSB allow the safety window to enlarge to 5V ascribing to the solid electrolytes. The safety window between the two types of battery is presented in **Fig. 1.6 (a)**. The superiorities of ASSB allow it to become an excellent selection for next generation battery.

1.4.1 Ion Transition Mechanism in Solid

Solid state leads to the ion transition mechanism in solid being totally different from liquid. The potential energy profile of mobile ions can be considered flat due to the uniform surrounding and the fast exchange between solvating molecules and solvent molecules. While the ion diffusion in solid needs to pass through bottleneck points which set an energy barrier. **Figure 1.6 (b)** shows the different potential energy profile in liquid and solid. The low energy barrier usually leads to high ionic mobility and ion conductivity. Hence, understanding the mechanism not only benefits improving the dilemma in current research but also promotes novel and efficient solid electrolyte development.

Fast ion conductor (FIC) is considered a candidate for solid electrolyte, because FIC maintains high ion conductivity over extended temperatures and chemical activities, simultaneously,

remains electronic insulating [152]. The FIC has high ionic conductivity and low activation energy below the melting point. There are two structural features of ion conductor: (1) highly ordered structure array, which can form tunnels, layers, or three-dimensional network localized on one of the ion sublattices; (2) highly disordered complementary sublattice, where the number of equivalent sites exceeds the number of available ions to fill them. Ion transition pathway plays a critical role in ion conductors based on the above features. Various solid electrolytes have already been fabricated following this critical rule, and the results indicate that there are two types of solid electrolytes roughly [153].

First type of solid electrolyte achieves ionic conductivity relies on point defects, including alkali and alkaline earth halides and some oxides. Ions only mobile among point defects in solids, such as vacancies or interstitial ions, this situation leads to an intrinsic conductivity associated with the point defect concentration. Simultaneously, extrinsic conductivity can be achieved by introducing impurities to create point defects in ionic or cationic sublattices. Extrinsic conductivity is related to the solid activation energy. Secondly, ion transit by disorder of sublattice of one of the ions, including α-AgI and β-Al_2O_3 [154]. Crystal lattice is constructed by one ionic species, many available energetically equivalent sites occur in mobile species sublattices. Meanwhile, those sites are separated by weak potential barriers.

I. Ion Conductivity in Solid

The ion conductivity can be expressed as **Eq. 1-8** with the assumption that the conduction occurs predominantly for a single ionic species:

$$\delta=n(Z_e)\mu \tag{1-8}$$

where n is the concentration of ion with charge Z_e and the mobility μ. A diffusion model is introduced in order to insight more details. The diffusion mode is characterized by isolated jump

with random walk of mobile species. Meanwhile, ions are visualized as vibrating within a potential well of energy E_m as a characteristic vibrational frequency v_0. Assuming Boltzmann statistics, the diffusion constant D is given by:

$$D=\alpha d^2 v_0 \exp(-E_m/kT) \tag{1-9}$$

where d is the ion jump distance, α is geometrical factor and k is Boltzmann constant, T is temperature. According to Nernst-Einstein equation, mobility μ can be expressed as:

$$\mu=\frac{Z_e D}{kT} \tag{1-10}$$

so, the ion conductivity is given by:

$$\delta=\frac{n(Z_e)^2\alpha d^2 v_0}{kT}\exp(-E_m/kT) \tag{1-11}$$

which shows temperature-depended ion conductivity following Arrhenius equation as found in solid conductors.

The structure defects are the nonnegligible ion passage, the most conventional ion conductors rely on this passage. In addition, the ion concentration depends on the defect formation. Schottky defect (cation-anion vacancy pair) and Frenkel defect (cation or anion vacancy-interstitial pair) are two major defects for ion conductor, and **Fig. 1.7 (a)** is the illustration of mainly structure defects in solid. In either case, the defect concentration, namely the mobile ion concentration, is given by:

$$n=n_0 \exp(-E_d/kT) \tag{1-12}$$

where E_d is 1/2 defect-pair formation energy, n_0 is the ion total amount. The fraction of mobile ion can be written as n/n_0. Since the value of E_d is usually large, while the value of n/n_0 is quite small. Thus, the ion conductivity is given by:

$$\delta=\frac{n_0(Z_e)^2\alpha d^2 v_0}{kT}\exp-(E_m+E_d)/kT \tag{1-13}$$

$$=\frac{n_0(Z_e)^2\alpha\beta d^2 v_0}{kT}\exp(-E_m/kT) \tag{1-14}$$

where β is the value of n/n_0.

II. Ion Transition Mechanism in Crystalline

The ion conductivity is strongly related to crystal defects, such as point defects, line defects, planar defects and volume defects. Since point defects are the most closely associated property according to experiment results, the transition mechanism is discussed based on point defects. **Figure 1.7 (b)** displays the schematic diagram of ion migration mechanism in solid. Carrier type, diffusion pathway and diffusion type are three factors that govern the ion transition mechanism in crystalline solid [155]. The classical microscopic approach of ion transition is a famous diffusion model in ionic crystals adapted by Stevel. This mode makes a point that the cations moment is random with the isolated jumping from one Coulombic well to another.

There are four typical crystal structures that show high ion conductivity. The crystal that has a γ-Li_3PO_4 framework structure is considered a promising candidate for solid electrolyte, reaching ion conductivity as high as 1.6×10^{-4} S/cm at room temperature [156]. This crystal usually experiences a phase transition (γ→β→α) with temperature increase, the ion transition is related to the tetrahedron arrangement which affects cations position [157]. These three inequivalent cation positions occur with phase transition from γ to β, which results in the cation sublattice disorder. Meanwhile, the tetrahedrons in β-phase present a zig-zag arrangement which allow cations to locate in tetrahedron and octahedron, further promoting interstitial cation diffusion and finally achieving ion transition.

The second structure is characterized by rhombohedral unit cell consisting of corner-shared tetrahedron and octahedron. Two octahedrons and three tetrahedrons share one oxygen atom and form a lantern structure, which builds a three-dimension network structure. A cation pathway is formed by this structure and cations are mobile in solid. The ion conductivity is not very high in

this crystalline structure, while in isovalent or aliovalent substitution of some element, such as Ti, the enhanced conductivity reaches as high as 1.0×10^{-3} S/cm at room temperature [158].

Crystalline with a perovskite structure ABX_3 shows a high potential application in solid electrolyte. This structure has a cubic unit cell consisting of A-ion at corner, B-ion at center and oxygen at the face-center. The coordination number of A-ion and B-ion is 12 and 6 respectively, they are corner-shared with each other. Smaller cation introductions would change Li and vacancies concentration simultaneously. Concentration and interaction of vacancies allow the ordering of Li or vacancies in the planes perpendicular to *c*-axis. Lithium ions are mobile in *ab* plane by those vacancies. Large rare-earth or alkaline-earth metal ion in A site can increase ion conductivity [159,160].

The last type is garnet crystal who possesses a general chemical formula of $A_3B_2(XO_4)_3$ and a face-centered cubic structure. Coordination number for A, B and X is 8, 6 and 4, respectively. Cation is located in both tetrahedron and distorted octahedron in this structure. Moreover, there is also a phase transition with temperature increase. The high temperature phase shows a higher ion conductivity because it always has a disordered cation sublattice and a three-dimension network structure formed by face-shared tetrahedron and octahedron.

III. Ion Transition Mechanism in Amorphous

Ion conductivity is affected by several factors, such as the mobile carrier concentration, based on **Eq. 1-13**. However, the total disorder structure of amorphous results in difficultly to specify these factors. Because the surrounding environment of the same type of ion in amorphous is likely different, a single characteristic migration energy or attempt frequency cannot be found, those properties should be expressed by distribution. The measured value is considered as either the average value or the highest potential barrier that the ions encounter during diffusion.

Plenty of attention has already been conducted and an assumption is put forward [153]. All of the alkali ions are treated as mobile ions, because each ion is surrounded by many nearly equivalent vacancies which allow ion migration. Those vacancies build the ion pathway. In addition, some researchers think those alkali ions should be dissociated from their original site linked to non-bridge oxygen (NBO) before the migration, and the ion jumps from one NBO to another NBO [161]. It is difficult to define the point defect because a defect can only exist in relation to an ordered structure for amorphous. Thereby, the above model is often regarded as Frenkel disorder which is a character of glass.

Warburg discovered the nature of cationic conductivity in 1884 and showed that good conductivity is obtained in the system consisting of alkali ions (Li, Na or K) and glass former oxides (SiO_2, B_2O_3 and P_2O_5). Those systems present similar ion conduct in crystalline with lattice defects with the following characters. Amorphous also has exclusive conductivity which is caused by lattice disorder or introduced impurities but the value is always low. Electrons are limited by the low coherence length which results from potential fluctuation caused by disorder. Those amorphous occupies low activation energy from 1 to 0.5 eV which promises the higher ion conductivity contrasted to crystalline. Summarizing and comparing the experiment results with crystalline, researchers think that amorphous has a same indirect interstitial mechanism of ion diffusion to crystalline, namely, the ions mobile in amorphous is relying on a pathway built by structure disorder [162].

The ion conductivity of amorphous is depended on the nature and concentration of its composition. The ion conductivity of silicate and borate glass increases with alkali ion concentration increase owning to the activation energy decline. Meanwhile, the larger alkali ion would lead to the higher activation energy, further reducing the ion conductivity [152]. Because

the strain energy is risen to squeeze larger alkali ion by restricted opening in amorphous. Divalent alkali ion addition would result in higher activation energy and lower conductivity.

1.4.2 Material for All-Solid-State Battery

All battery material is solid state in ASSB, this is the largest discrepancy with conventional lithium ion battery. The strong interfacial resistance between solid electrode and electrolyte caused by the poor connection impairs the ion transition to great extents although there are no side reactions of solid electrolyte dissociation, which reduce cycling life-span and poor performance [163]. Therefore, the ASSB material research concentrates on improving interfacial connection and enhancing energy density.

I. Anode Material

Lithium metal is considered a promising anode material for ASSB because of its high specific capacity and low electrochemical energy [164]. Meanwhile, the inorganic solid electrolytes utilization can avoid leakage and flammability [165]. While lithium dendrites would be formed during the cycling, resulting in the lithiation/delithiation amount decline [166]. The short current would occur when the current is over the critical current density of electrolyte [167]. Above situations are caused by the insufficient interfacial contact between Li anode and solid electrolyte. The high electronic conductivity also results in those problems [168]. In addition, lithium metal can react with H_2O, O_2, and CO_2 in atmosphere, which causes a challenge for storage and assembly. Artificial protection layer between Li anode and solid electrolyte is introduced to improve this dilemma. Various layers are investigated, such as Li_2CO_3, Al_2O_3, Li_2O, and Li_xSiS_y, the Li anode becomes more stable in air after the artificial layer utilization [169–172].

Addition of other metals to Li anode to form alloy anode is one method to improve Li anode property. Because the anode material based on electrochemical alloy reaction allows Li ion to move inside the anode material rather than concentrating on the surface, providing a more stable interface between electrolyte and anode [173]. There are two types of electrochemical alloy reactions, one is the reconstitution reaction and the other is solid-solution reaction [174]. The former would experience a phase transition which results in additional activation energy. Much less structure change during solid-solution reaction, which allows reaction to occur with a low charge-discharge voltage hysteresis at a potential close to Li/Li^+ redox couple [175]. The general formula of alloy anode material is Li_xM, where M can be Si, Sn, Mg, Ag, and so on. Until now various Li alloy anode materials have already been prepared [174,176,177].

Carbon group anode materials are an important series for ASSB anode. Carbon materials such as graphite show a low potential and a charge/discharge efficiency of over 90%, simultaneously, it also has a layer structure that can allow Li ion insertion and extraction. However, the theoretical capacity of around 372 mAh/g is too low to satisfy large devices [178,179]. The SiS_2-based glass solid electrolyte is not compatible with graphite anode during the experiment [180]. Another candidate in carbon group is the Si anode, the high gravimetric capacity, low voltage window, low price, and abundance lead to Si being considered an ideal material both in science and industry [181]. While the pulverization of Si anode caused by the volume change during cycling and unstable interface limits its application, coating artificial layer and double-wall nanotube utilization are proven to improve these problems [182,183].

II. Cathode Material

The cathode material of ASSB is usually a composite electrode. The cathode consists of electrode active material, solid electrolyte, and conductive agent which is used for ion and

electron transition. However, the inevitable interface also affects cathode properties negatively as mentioned above.

The oxides, such as $LiCoO_2$, $LiFePO_4$, and $LiMnO_2$, are put in high hopes and used as promising cathodes due to high electrode potential [184,185]. A space-charge layer is formed between solid electrolyte and cathode. Sulfide-based material is always selected as the solid electrolyte because of its high ion conductivity. Since the massive discrepancy of chemical potential between sulfide and oxide, the Li ion would transit from electrolyte to electrode which causes the Li ion to be depleted of electrolytes interface and a space-charge layer is formed. Moreover, the such space-charge layer would be strengthened when cathode material is mixed-conduct oxide, namely, the oxide also achieves electron conduct besides ion conduct. The space-charge layer on cathode can vanished by decreasing the Li concentration gradient between cathode and electrolyte. The concentration gradient of Li ion can be resolved by the electron conduct, further achieving the equilibrium of Li ion transiting from electrolyte to cathode additionally, finally, the enlarged space-charge layer of electrolyte would be formed [186].

Introducing thin oxide film which is characterized by ion conduction and electrode insulation to cathode surface was proven to prevent space-charge layer efficiency. This thin film forms two interfaces, one is the interface between cathode and introduced layer. This interface can reduce space-charge layer because there is a small difference in chemical potential between two oxides. Another is the interface between solid electrolyte and introduced layer, the space-charge layer is also suppressed owing to electron insulation. Various oxide artificial thin films have already been developed, such as $Li_4Ti_5O_2$, $LiNbO_3$, and Li_3BO_3, these experiment results indicate that the electrochemical property of ASSB is enhanced [186–188].

Continuous research is conducted to obtain high-performance cathode material aiming to improve electrochemical properties of ASSB. The $LiNi_xCo_yMn_zO_2$ (NCM, with x+y+z=1) is

developed as a promising cathode material in industry application. There are several ratios for three elements, such as NCM 433 (x:y:z=4:3:3), NCM 532, NCM 622, and NCM 822 [189]. Compared to conventional oxide cathode, the NCM occupies a high energy density (>200 mAh/g at 4.3-4.6 eV) [190]. The fixable ratio and synergistic effect of three elements lead to NCM being compatible with Ni, Co, and Mn advantages simultaneously. Nickel ions are used as electroactive species and provide higher capacity, cobalt ions enhance rate performance and processing ability and Mn ions with 4^+ valence can maintain structure stability [191].

III. Electrolyte Material

Sulfide and oxide are two main candidates for solid electrolytes. Various solid electrolytes with different compositions and structures have already been obtained by different fabrication methods. **Figure 1.8** is the summary of ionic conductivity of different solid electrolytes. Sulfide occupies relatively high Li ion conductivity compared to oxide. In addition, amorphous electrolytes show better electrochemical property than crystalline. Here, the following introduction focuses on crystalline electrolytes, amorphous will be introduced in next section with more details.

Sulfide electrolytes present a high ion conductivity at room temperature. Various sulfide electrolytes were synthesized, such as Li_2S-GeS_2, Li_2S-GeS_2-ZnS, and Li_2S-GeS_2-Ga_2S_3 systems [192]. The similarity among those sulfides is the γ-Li_3PO_4-type structure. This structure is characterized by oxides tetrahedrons and LiO_6 octahedrons [193]. There are six candidates for above systems, they are Li_2GeS_3, Li_4GeS_4, Li_2ZnGeS_4, $Li_{4-2x}ZnGeS_4$, Li_5GaS_4, and $Li_{4+x+\delta}(Ge_{1-\delta'-x}Ga_x)S_4$, respectively [194]. Ion conductivity as high as 6.5×10^{-5} S/cm at room temperature was obtained for $Li_{4+x+\delta}(Ge_{1-\delta'-x}Ga_x)S_4$. Meanwhile, the property of ASSB assembled by $Li_{4+x+\delta}(Ge_{1-\delta'-x}Ga_x)S_4$/$LiCoO_2$ was also investigated, the battery was charged/discharged from 0.5 V to 4.2 V at a constant current in 13-64 μA/cm^2 range at room temperature. Lithium silicon sulfides system is

another candidate for crystalline sulfide electrolytes. Compounds belonging to this system also have a γ-Li_3PO_4-type structure. The ion conductivity would be enhanced when Li ion interstitials or Li ion vacancies are created by partial substitution of other cations. The solid solution $Li_{4-x}Si_{1-x}P_xS_4$ (x=0.6) presents an excellent ion conductivity of 6.4×10^{-4} S/cm at room temperature with negligible electronic conductivity [195].

A serious problem that cannot be ignored in sulfide electrolytes is the poor chemical and electrochemical stability. This disadvantage causes the harmful gas H_2S generation during cycling, which further impairs performance of battery. Oxide attracts great attention owing to its good chemical and electrochemical stability. Various oxide solid electrolytes were fabricated. While the low ion conductivity (around $10^{-6} \sim 10^{-8}$ S/cm) at room temperature makes a huge challenge. Aiming to solve this problem different novel structure oxide electrolytes are synthesized.

The first reported oxide about LISICON-type electrolyte is $Li_{12}Zn(GeO_4)_4$ which shows ion conductivity as high as 1.25×10^{-1} S/cm at 573 K. Two factors are proposed in ion conductor, first one is the size of bottlenecks between neighboring Li ion position, the second one is the bonding energy between mobile Li ion and network anion O^{2-} [196]. The network is constructed by $[Li_{11}Zn(GeO_4)_4]^{3-}$ for $Li_{12}Zn(GeO_4)_4$ and other free Li ion can diffuse between interstitial positions. New LISICON-type electrolytes $Li_{10.42}Si_{1.5}P_{1.5}Cl_{0.08}O_{11.92}$ and $Li_{10.42}Ge_{1.5}P_{1.5}Cl_{0.08}O_{11.92}$ which partially doped O^{2-} with Cl^- was synthesized aiming to obtain higher ion conductivity. The above electrolytes show ion conductivity of 1.03×10^{-5} S/cm and 3.7×10^{-5} S/cm at room temperature, respectively [197]. Moreover, $Li_4Al_{1/3}Si_{1/6}Ge_{1/6}P_{1/3}O_4$ is predicted has ion conductivity of 9×10^{-4} S/cm based on MD simulation [198].

Perovskite-type oxide electrolytes are always written as LLTO due to the first reported compound is $Li_{3x}La_{2/3-x}TiO_3$. Lithium and La ions are in the center, titanium ions occupy the corners in perovskite-type electrolytes. The $Li_{3x}La_{2/3-x}TiO_3$ presents a bulk ion conductivity of

1×10^{-3} S/cm and an ion conductivity of over 2×10^{-5} S/cm at room temperature [199]. The modified perovskite-type electrolyte was reported that has higher ion conductivity than the originals. The $Li_{3/8}Sr_{7/16}Ta_{3/4}Zr_{1/4}O_3$(LSTZ) was found that the highest ion conductivity of 2×10^{-4} S/cm and 1.33×10^{-4} S/cm for bulk and grain boundary respectively at room temperature [200].

Another important oxide electrolyte is garnet-type electrolyte which is first reported with the composition of $Li_3Ln_3M_2O_{12}$(M = Te, W; Ln = Y, Pr, Nd, Sm, Eu, Gd, Tb, Dy, Ho, Er, Tm, Yb, Lu). Different elements in electrolyte display various lattice constant. The ion conductivity is affected by the stability of octahedron [201]. The $Li_3Ln_3M_2O_{12}$ has a lower ion conductivity of around 10^{-6} S/cm at room temperature. Doping strategy is introduced in order to enhance ion conductivity. Barium-doped $Li_6BaLa_2Ta_2O_{12}$ shows an ion conductivity of 4.0×10^{-5} S/cm [202]. Gallium-substituted $Li_{6.55}Ga_{0.15}La_3Zr_2O_{12}$ which was prepared in dried O_2 atmosphere shows excellent ion conductivity as high as 1.3×10^{-3} S/cm at 297 K and 2.2×10^{-3} S/cm at 315 K [203].

1.5 Research on Amorphous Electrolyte

Amorphous solids are considered to have optional high ion conductivity based on ion transform mechanism in solid, because they have more structure point defects and minimization of the grain-boundary effect. Moreover, amorphous nanoparticles also present unique advantages in processability, stability, and tunability [204]. Since the larger specific surface area of amorphous nanoparticles benefits reducing interfacial resistance, declining amorphous particle size to nanoscale is considered a research hotspot.

1.5.1 Conventional Amorphous Fabrication Methods

The disorder and chaotic structure of amorphous material lead to its fabrication method being totally different from crystalline. Because the structure of amorphous material is similar to liquid,

how to maintain this structure in solid state becomes important. Lots of attempts are tried in order to achieve these goals, melting quenching is a common method. Sol-gel method and mechanical milling are also developed with the technology process.

I. Sol-gel Method

The first attempt at inorganic ceramic and glass was fabricated by sol-gel method as early as the mid-1800s. Ebelman and Graham observed that SiO_2 glass was obtained by hydrolysis of tetraethyl orthosilicate and $Si(OC_2H_5)_4$ under acidic condition [205]. The lower processing temperature, high homogeneity and purity of target material, and possibility of various forming processing allow sol-gel method to become an ideal method for glass fabrication [206–208]. Binary systems ZrO_2-SiO_2, SiO_2-P_2O_5 glass, complex composition system SiO_2-P_2O_5-CaO-Ag_2O, SiO_2-P_2O_5-CaO-MgO-Na_2O-K_2O glass have already been synthesized successfully by sol-gel method [209–212].

II. Mechanical Milling Method

Mechanical milling is considered a method for stabilizing nonequilibrium phase. Amorphization of solid-state is a common utilization of mechanical milling. The milling process is a defect accumulation process, the increase of energy would cause the loss of stability [213,214]. Meanwhile, the material amorphous systems have different composition ranges for amorphous synthesis, the composition range can be modified by changing milling conditions, such as milling intensity [215,216]. Mechanical milling is widely applied to amorphous fabrication, especially for the system that is difficult to form into glass. Alloy glass is an important region, such as Fe-W, Cr-C, and Ag-Pa [217–219]. High Li content compounds are also difficult to form into

amorphous, glass-ceramic $Li_7P_2S_8I$, amorphous $Li_2Si_2O_5$, and novel $LiTi_2(PO_4)_3$ glass-ceramic nanoparticles are acquired successfully by this method [220–222].

III. Melt Quenching Method

The melt quenching technology is widely used in glass and glass-ceramic production. Compared to sol-gel method melt quenching consumes less time while requiring higher operation temperature. This technique is developed by Duwez and his collaborators in the 1960s, the high cooling rate can reach 10^6 to 10^5 K/s [223]. The high purity raw material (99.9%) is same stoichiometric as target material. The raw material is milled to mix sufficiently before heating. The melt can be quenched in the atmosphere on a cooper plate. The quenched glass flake is annealed at 773 K in order to remove the internal stress [224]. The products synthesized by melt quenching present a plate morphology. Lots of glass with different functions are successfully synthesized. Amorphous sulfide electrolyte Li_2S-P_2S_5 with high ion conductivity, glasses of GeSbSe, SLS-ZnO have already been obtained [225–227]. In addition, melt quenching method is available to bioactivity material SiO_2-BaO-ZnO-B_2O_3-Al_2O_3 glass and SiO_2–B_2O_3–AO–La_2O_3 (A = Sr, Ba) glass [228,229].

1.5.2 Amorphous Lithium Sulfide

Sulfide electrolytes have high ion conductivity even at room temperature as previous mentioned. Amorphous sulfide electrolytes occupy higher ion conductivity in contrast to crystalline. The lithium thiophosphate (LPS) is the most studied sulfide system. The first-time report about high conductivity of LPS is in the late 1970s, the researcher found that doping lithium halides (LiBr, LiI) can rise LPS glass conductivity to a great extent [230]. Increased ion conductivity is found with the P_xS_y unit transiting from di-tetrahedron $P_2S_7^{4-}$ to tetrahedron PS_4^{3-}

with different Li_2S to P_2S_5 molar ratios. Simultaneously, the declined active energy is observed in increased non-bridge sulfur atoms [231]. However, it is not that the higher Li content the better. There is a limitation of Li_2S to P_2S_5 molar ratio. Non-conducting Li_2S crystal would be generated in amorphous material when Li_2S:P_2S_5 ratio increases to 4:1, which results in the barrier for Li diffusion. Various LPS solid electrolytes have already been fabricated. The Li_3PS_4 glass who was prepared by wet-chemical method shows an anomalous high conductivity of around 1.64×10^{-4} S/cm [156]. The $70Li_2S$-$30P_2S_5$ glass was prepared by quenching melts achieving high ion conductivity of 2.1×10^{-3} S/cm, which can replace liquid electrolytes directly [232]. The glass-ceramic of Li_2S-P_2S_5-LiN which is prepared by mechanical milling owns conductivity around 1.4×10^{-3} S/cm [233].

The Li_2S-GeS_2-Ga_2S_3 system glass solid electrolyte was also prepared with limited compositions. The composition ranges of glass formation are <10% or 40%-60% of 1/2 Li_2S with small amounts of Ga_2S_3. The highest ion conductivity was 1.4×10^{-4} S/cm [234]. Unfortunately, the Ge atom would compromise the chemical compatibility of LPS with Li metal [235]. Since silicon is another typical glass former, the Li_2S-SiS_2 system glass electrolyte was also prepared. Over 2×10^{-3} S/cm ion conductivity was achieved in $60Li_2S$-$40SiS_2$ [236].

1.5.3 Amorphous Lithium Phosphate Oxynitride

Serious Li-penetration problem is observed when electrolytes connect with metallic lithium anodes, which further results in interfacial compatibility problems. Lithium phosphate oxynitride (LiPON) was introduced because of its remarkable resistance to Li-penetration owing to the low electronic conductivity [237]. However, its ion conductivity is low around 10^{-6} S/cm at room temperature. In the 1990s, the amorphous LiPON was reported first time [238,239]. The LiPON is considered to consist of randomly oriented, corner-shared $PO_{4-y}N_y$ tetrahedron, the lithium

atoms are distributed randomly within the interstices of network. The most common fabrication method for LiPON is ratio frequency magnetron sputtering.

Lots of research have been developed aiming to enhance ion conductivity at room temperature. These researches indicate that conductivity benefits from former disorder [240]. Substitution of nitrogen, silicon, or boron on oxygen sites can enhance the structure disorder, further enhancing ion conductivity [241,242]. Electronegativity decrease of the system is achieved by anionic substitution, simultaneously, non-bridge specie is also enhanced in material, which reduces the required energy for interstitial Li mobility. Another method to improve conductivity is adding excessive Li, which increases the percentage of available interstitial Li, thereby, obtaining higher conductivity [243].

1.5.4 Amorphous Lithium Oxide

Amorphous sulfide electrolytes not only generate harmful gas H_2S during cycling but also cannot avoid lithium dendrite growth as previous introduction. Above serious problems make that new material development becomes an urgent issue. Lithium oxide electrolytes stand out among all candidates owing to their impressive chemical and electrochemical stability. Amorphous oxide electrolytes become the research focus in the next stage combing the ion transform mechanism in solid with stability issues. Diverse system electrolytes which contain common glass former have already been synthesized by conventional amorphous fabrication methods.

I. Amorphous Lithium Phosphate System

Electrochemical properties of $50Li_2O$-$(50-x)P_2O_5$-xAl_2O_3 amorphous electrolyte were also investigated [244]. A series of glass was prepared by melting quenching method. The ion conductivity shows a non-linear change with Al_2O_3 content increase, the maximum is obtained at

6.25% of Al_2O_3 around 3.4×10^{-7} S/cm at 323 K and 3.9×10^{-4} S/cm at 573 K, respectively. Meanwhile, the experiment also indicates a structure change with different Al_2O_3 content is related to the conductivity change. The molar volume presents a decreased tendency with Al_2O_3 increase from 0 to 6.25%, then increases with Al_2O_3 continuously increase. Conductivity would rise with density increase, with a peak of 6.25% Al_2O_3 in density, while it also descent due to the available interstitial volume [245].

Nanoscale glassy powder Li_2O-Al_2O_3-TiO_2-P_2O_5 (LATP) was synthesized by melting quenching method and mechanical milling [246,247]. The LATP nanoparticles have high conductivity of 10^{-3} S/cm at room temperature. The LATP consists of MO_6 octahedrons and PO_4 tetrahedrons which link with each other by corner-sharing to form a 3D network structure. Lithium ions located in 6-fold O octahedron are responsible for mobile, being located in 10-fold O coordination are favorable for chemical stability of electrolytes besides being mobile. The sample, $Li_{1.4}Al_{0.4}Ti_{1.6}(PO_4)_3$, was synthesized by mechanical milling, displaying the highest conductivity of 1.09×10^{-3} S/cm with activation energy of 0.28 eV at room temperature.

The ion conductivity of amorphous lithium phosphate was also investigated based on thermodynamic modeling of their chemical structure[248]. The calculated results demonstrated that the ion conductivity increase with Li_2O percentage increase due to more non-bridge oxygen bonds formation. These non-bridge oxygen bonds thermally activate hopping between negatively charged positions, further leading to higher ion conductivity [249]. The calculated results have a similar increased tendency with experimental results in ion conductivity, although the value is higher than experiments. This situation can be explained by the arrangement of lithium coordination polyhedrons LiO_n (n=4 or 5) in a sort of percolation channels where the last would be linked through O-Li-O.

II. Amorphous Lithium Silicate System

Amorphous electrolytes of the Li_2O-P_2O_5-SiO_2 system were prepared by sol-gel method. Different molar ratio products show different ion conductivity. The lower conductivity is obtained at 573 K while high value is achieved at 289 K for all products, which mostly owing to protonic conduction at room temperature. Moreover, increasing Li and P content also attributes to Li conductivity. Selected samples, $10Li_2O$-$25P_2O_5$-$65SiO_2$, show conductivity as high as 2×10^{-3} S/cm at room temperature [250].

The complex silicate-based amorphous electrolyte Li_2O-K_2O-Al_2O_3-SiO_2 was also systematically studied [251]. Addition of V_2O_5 to Li_2O-K_2O-Al_2O_3-SiO_2 can increase mechanical properties, chemical resistance and thermal stability [252]. The ion conductivity increases with V_2O_5 content increase although Li_2O content decrease. Simultaneously, the ion conductivity presents a high value at high temperature than low temperature. Topological order of the amorphous silicate-based electrolyte was investigated aiming to understand this phenomenon by MD simulation. The ratio of NBO/BO experiences a rising tendency with V increase. The average jump distance of Li ion is small at low temperature, which results in the less connection of conduction channels. The V plays as the network former at low V content while playing as a channel former at high content. The connection of ion conduction channel can be enhanced by the V-channel, and high Li conduction is achieved.

Molecular dynamic was utilized to simulate the ion pathway in amorphous lithium silicate electrolyte [253]. The increased Li content leads to higher ion conductivity due to the enhanced density and connectivity of pathway for the motion of Li^+ in the amorphous. The high Li content allows the volume fraction of pathway cluster to be increased, meaning the local pathway dimensional becomes higher in Li-rich condition.

III. Amorphous Lithium Borate System

Amorphous lithium borate-based electrolyte attracts lots of interest because boron is a typical network former. The $Li_2O–SeO_2–B_2O_3$ amorphous electrolytes were prepared by melt quenching and characterized by various analysis methods [254]. The maximum conductivity was observed in the 50% Li_2O condition. The typical mixed-former effect was responsible for the increased ion conductivity. The SeO_2 acts as a network former in SeO_2-rich composition and provides another ion pathway, which allows the higher Li ion mobility.

Lithium ion conducting glass of Li_2O-B_2O_3-SiO_2 was prepared by melt quenching, the maximum of conductivity was acquired with $50Li_2O–38B_2O_3–12SiO_2$ glass sample around 2×10^{-6} S/cm [255]. The ion conductivity strongly relies on the Li_2O content. The glass formation region in ternary Li_2O-B_2O_3-SiO_2 system can be extended when the ratio of SiO_2/B_2O_3 decreases to 0.3. The viscosity and crystallization tendency are decreased by addition of B_2O_3.

The local structure of lithium borate glass was also studied by high resolution solid state NMR same as other lithium oxide system glass [256]. The ion conductivity increases with Li ion addition due to the number of ion carrier increasing, simultaneously, the BO_3 unit gradually transforms to BO_4^-. This tendency conforms to Arrhenius behavior characterized by thermally activated transport. However, the generation of NBO with Li continuous addition would impair Li mobility by the interaction and result in declined conductivity.

IV. Amorphous Lithium Titanate System

Perovskite-type $Li_{3x}La_{2/3-x}TiO_3$ (LLTO) evokes lots of interesting ascribing to high ion conductivity, however, crystalline LLTO is not stable when connect to Li metal because Ti^{4+} is reduced to Ti^{3+}, further results in high electronic conductivity [257]. Amorphous LLTO can solve this problem and maintain high conductivity simultaneously. Amorphous LLTO was prepared by

sol-gel method [258]. The conductivity is 4.5×10^{-6} S/cm, 6.9×10^{-6} S/cm, 1.3×10^{-5} S/cm and 3.8×10^{-5} S/cm at 303 K, 323 K, 343 K and 363 K, respectively. This growth tendency indicates amorphous LLTO stability over a wide temperature range. Activation energy over this temperature range is fixed at 0.36 eV.

1.6 Objective and Contents

Amorphous oxide nanoparticles with high Li content are promising candidates for solid electrolytes, researching high-performance and novel lithium oxide nanoparticles contributes to ASSB development and application. The sufficient structure defects of amorphous promise Li ion mobility, which has a positive effect on ion conductivity. Enhanced formability is acquired when the size of amorphous particles decreases to nanoscale. Since the chemical and physical properties of amorphous independent of direction, isotropic ion conductivity can be achieved. In addition, the large specific surface area of amorphous nanoparticles promotes the connection between electrolyte and electrode, further reducing the strong interfacial resistance. However, the limitation of conventional synthesis methods results in a dilemma in solid electrolyte research. Hence, it is urgent and necessary to search for an efficient and advanced synthesis method for amorphous oxide nanoparticles with high Li content.

Induction thermal plasma is considered an excellent method for amorphous nanoparticle synthesis owing to its unique superiorities. The extremely high temperature (up to 10^4 K) allows raw material to decompose and vaporize immediately after injecting into thermal plasma. The rapid quenching rate (10^3-10^6 K/s) can prevent orderly growth, and form into amorphous structure. In addition, counter-flow quenching gas utilization can further increase quenching rate. Electroless discharge of induction thermal plasma avoids the pollution from electrodes, which allows products to achieve high purity. Therefore, the objective of this dissertation is synthesis of

amorphous lithium oxide nanoparticles with different systems and investigation of formation mechanism. Amorphous Li_3BO_3, Li_4GeO_4, and Li_5AlO_4 were selected as target material based on the following reason. Boron, germanium, and aluminum can function as glass former to construct the skeleton of amorphous. High Li content offers more ion carriers to ensure high ion conductivity to satisfy the requirement of electrolytes. The low glass transition temperature allows the amorphous structure to more easily form during the rapid quenching process. The amorphous $LiPO_3$ and Li_4SiO_4 nanoparticles have been synthesized by induction thermal plasma in our laboratory. The amorphous Li_2O-B_2O_3-P_2O_5 and Li_2O-B_2O_3-SiO_2 nanoparticles were also considered as the target material before the experiment. This mixed glass former effect is considered to investigate in the future work.

Figure 1.9 shows the flow diagram of this dissertation, and the contents in each chapter will be presented briefly in this section.

In chapter 2, amorphous Li_3BO_3 nanoparticles were synthesized by induction thermal plasma with different Ar/O_2 molar ratios in sheath gas, different Ar and O_2 quenching gas flow rates. Formation mechanism of lithium borate was investigated after analyzing thermodynamic equilibrium and experiment results. Particle growth process during plasma process was understood to clarify the formation mechanism of amorphous nanoparticles. The effects of O_2 and quenching gas flow rate on the amorphous degree and chemical composition were discussed based on borate unit transformation and temperature distribution.

In chapter 3, amorphous Li_4GeO_4 nanoparticles were synthesized by induction thermal plasma. The experiment was conducted by different Ar/O_2 molar ratios in sheath gas, different Li/Ge molar ratios in raw material, different carrier gas and quenching gas flow rates. Formation mechanism of lithium germanate was studied based on experiment results and thermodynamic analysis. The saturation ratio of different phases was utilized to understand the chemical

composition variation. The Ge content and quenching rate effect were discussed according to the topological order of products.

In chapter 4, amorphous Li_5AlO_4 nanoparticles were synthesized by induction thermal plasma under the experiment conditions of different Li/Al molar ratios in raw material and quenching gas flow rates. Formation mechanism of lithium aluminate was understood by combining the experiment results with thermodynamic analysis. Aluminate polyhedron and Al coordination number were introduced to elucidate amorphous degree tendency. The effects of Li content in raw material and quenching gas flow rate were discussed based on O/Al molar ratios and aluminate polyhedrons transformation.

In chapter 5, the formation ability of amorphous nanoparticles with high Li content was studied based on comparing experiment results of Li-B-O, Li-Ge-O and Li-Al-O systems. The formation ability was discussed from product structure and chemical composition. The formation ability was summarized relying on bond strength, time lag of co-condensation and structure unit transformation.

In chapter 6, the conclusion was summarized and future works were put forward to improve the research.

Reference:

[1] F.F. Chen, Introduction to Plasma Physics and Controlled Fusion, Third, Springer International Publishing, 2016. https://doi.org/10.1007/978-3-319-22309-4_11.

[2] R. Goldston, P. Rutherford, Introduction to Plasma Physics, 1995. https://doi.org/10.1201/9781439822074.

[3] A. Fridman, Plasma Chemistry, 1 st ed., Cambridge University Press, New York, 2008.

[4] P.E. Boulos M I, Fauchains P, Thermal Plasmas：Fundamentals and Applications. Vol. 1, New York: Plenum Press, 1994.

[5] S. Samal, Thermal plasma technology: The prospective future in material processing, J Clean Prod. 142 (2017) 3131–3150. https://doi.org/10.1016/j.jclepro.2016.10.154.

[6] F.L. Tabares, I. Junkar, Cold Plasma Systems and Their Application in Surface Treatments for Medicine, Molecules. 26 (2021). https://doi.org/10.3390/molecules26071903.

[7] H. Conrads, M. Schmidt, Plasma generation and plasma sources, Plasma Sources Sci. Technol. 9 (2000) 441–454.

[8] M.I. Tanaka, Hiroshi, Plasma Processing of Materials and Atomic, Physics. an Introduction, 43 (2000) 1–12.

[9] R. Henne, Thermal plasmas for material processing, Contributions to Plasma Physics. 39 (1999) 385–397. https://doi.org/10.1002/ctpp.2150390503.

[10] M. Ushio, Arc discharge and electrode phenomena, Pure and Applied Chemistry. 60 (1988) 809–814.

[11] L.S. Camacho, Industrial-worthy plasma torches: State-of-the-art, Pure and Applied Chemistry. 60 (1988) 619–632. https://doi.org/doi.org/10.1351/pac198860050619.

[12] G. Ecker, The Vacuum Arc Cathode-A Phenomenon of Many Aspects, IEEE Transactions on Plasma Science. PS-4 (1976). https://doi.org/10.1109/TPS.1976.4316971.

[13] Z. Guo, S. Yin, H. Liao, S. Gu, Three-dimensional simulation of an argon-hydrogen DC non-transferred arc plasma torch, Int J Heat Mass Transf. 80 (2015) 644–652. https://doi.org/10.1016/j.ijheatmasstransfer.2014.09.059.

[14] D.R. Macrae, Plasma-arc Technology for Ferroalloys, Part II, Cape Town. Volume I. Johannesburg. SArMM. I (1992) 21–35.

[15] K.C. Hsu, K. Etemadi, E. Pfender, Study of the free-burning high-intensity argon arc, J Appl Phys. 54 (1983) 1293–1301. https://doi.org/10.1063/1.332195.

[16] J.J. Lowke, Simple theory of free-burning arcs, J Phys D Appl Phys. 12 (1979) 1873–1886. https://doi.org/10.1088/0022-3727/12/11/016.

[17] L. Fulcheri, F. Fabry, S. Takali, V. Rohani, Three-Phase AC Arc Plasma Systems: A Review, Plasma Chemistry and Plasma Processing. 35 (2015) 565–585. https://doi.org/10.1007/s11090-015-9619-8.

[18] A. V. Surov, S.D. Popov, V.E. Popov, D.I. Subbotin, E.O. Serba, V.A. Spodobin, G. V. Nakonechny, A. V. Pavlov, Multi-gas AC plasma torches for gasification of organic substances, Fuel. 203 (2017) 1007–1014. https://doi.org/10.1016/j.fuel.2017.02.104.

[19] Y. Yao, M.M. Hossain, T. Watanabe, T. Matsuura, F. Funabiki, T. Yano, A multi-phase AC arc discharge and its application in in-flight thermal treatment of raw glass powders, Chemical Engineering Journal. 139 (2008) 390–397. https://doi.org/10.1016/j.cej.2007.11.016.

[20] M. Tanaka, Y. Saito, H. Maruyama, T. Watanabe, High-speed visualization of metal oxide precursor in multiphase AC arc during nanoparticle formation, Jpn J Appl Phys. 59 (2020). https://doi.org/10.35848/1347-4065/ab7e15.

[21] Y. Yao, K. Yatsuda, T. Watanabe, T. Matsuura, T. Yano, Characteristics of multi-phase alternating current arc for glass in-flight melting, Plasma Chemistry and Plasma Processing. 29 (2009) 333–346. https://doi.org/10.1007/s11090-009-9182-2.

[22] R.N. Szente, R.J. Munz, M.G. Drouet, Arc velocity and cathode erosion rate in a magnetically driven arc burning in nitrogen, J Phys D Appl Phys. 21 (1988) 909–913. https://doi.org/10.1088/0022-3727/21/6/008.

[23] M. Tanaka, T. Ikeba, Y. Liu, S. Choi, T. Watanabe, Investigation of electrode erosion mechanism of multi-phase AC arc by high-speed video camera, J Phys Conf Ser. 441 (2013). https://doi.org/10.1088/1742-6596/441/1/012015.

[24] M. Tanaka, T. Hashizume, K. Saga, T. Matsuura, T. Watanabe, Diode-rectified multiphase AC arc for the improvement of electrode erosion characteristics, J Phys D Appl Phys. 50 (2017). https://doi.org/10.1088/1361-6463/aa8cac.

[25] X. Xu, Z. Ren, S. Yang, Design and Optimization of a Hybrid Excitation System for Magnetically Driven Rotating DC Arc Plasma Generators, IEEE Access. 9 (2021) 157012–157020. https://doi.org/10.1109/ACCESS.2021.3128583.

[26] M.I. Boulos, The inductively coupled r.f. (radio frequency) plasma, Pure and Applied Chemistry. 57 (1985) 1321–1352. https://doi.org/10.1351/pac198557091321.

[27] T.B. Reed, Induction-Coupled Plasma Torch, Jouranl of Applied Physics. 32 (1961).

[28] M. Schaepkens, N.R. Rueger, J.J. Beulens, X. Li, T.E.F.M. Standaert, P.J. Matsuo, G.S. Oehrlein, Effect of capacitive coupling on inductively coupled fluorocarbon plasma processing, Journal of Vacuum Science & Technology A: Vacuum, Surfaces, and Films. 17 (1999) 3272–3280. https://doi.org/10.1116/1.582054.

[29] M. Watanabe, D.M. Shaw, G.J. Collins, H. Sugai, Radio-frequency plasma potential variations originating from capacitive coupling from the coil antenna in inductively coupled plasmas, J Appl Phys. 85 (1999) 3428–3434. https://doi.org/10.1063/1.369700.

[30] N.M. Reed, R.O. Cairns, R.C. Hutton, Y. Takaku, Characterization of polyatomic ion interferences in inductively coupled plasma mass spectrometry using a high resolution mass spectrometer, J Anal At Spectrom. 9 (1994) 881–896. https://doi.org/10.1039/ja9940900881.

[31] M.I. Boulos, RF induction plasma spraying: State-of-the-art review, Journal of Thermal Spray Technology. 1 (1992) 33–40. https://doi.org/10.1007/BF02657015.

[32] K. Major, J. Veilleux, G. Brisard, Lithium Iron Phosphate Powders and Coatings Obtained by Means of Inductively Coupled Thermal Plasma, Journal of Thermal Spray Technology. 25 (2016) 357–364. https://doi.org/10.1007/s11666-015-0289-0.

[33] X. Zhang, R. Hayashida, M. Tanaka, T. Watanabe, Synthesis of carbon-coated silicon nanoparticles by induction thermal plasma for lithium ion battery, Powder Technol. 371

(2020) 26–36. https://doi.org/10.1016/j.powtec.2020.05.084.

[34] A.S. Westover, A.K. Kercher, M. Kornbluth, M. Naguib, M.J. Palmer, D.A. Cullen, N.J. Dudney, Plasma Synthesis of Spherical Crystalline and Amorphous Electrolyte Nanopowders for Solid-State Batteries, ACS Appl Mater Interfaces. (2020). https://doi.org/10.1021/acsami.9b20812.

[35] K.K. Falkner, D.M. Christie, Inductively Coupled plasma-Optical Emission Spectroscopy, Earth. 46 (1995).

[36] E.R.G. Eckert, E. Pfender, Advances in Plasma Heat Transfer, Adv Heat Transf. 4 (1967) 229–316. https://doi.org/10.1016/S0065-2717(08)70275-2.

[37] E. Mensing, L.R. Boedeker, Theoretical Investigation of R-F Induction Heated Plasma, NASA CR-1312, 1969.

[38] M. Moisan, Z. Zakrzewski, Plasma sources based on the propagation of electromagnetic surface waves, J Phys D Appl Phys. 24 (1991) 1025–1048. https://doi.org/10.1088/0022-3727/24/7/001.

[39] K. V. Khodataev, Microwave discharges and possible applications in aerospace technologies, J Propuls Power. 24 (2008) 962–972. https://doi.org/10.2514/1.24409.

[40] Y. Kabouzi, D.B. Graves, E. Castaños-Martínez, M. Moisan, Modeling of atmospheric-pressure plasma columns sustained by surface waves, Phys Rev E. 75 (2007) 1–14. https://doi.org/10.1103/PhysRevE.75.016402.

[41] Z. Zakrzewski, Conditions of existence and axial structure of long microwave discharges sustained by travelling waves, J Phys D Appl Phys. 16 (1983) 171–180. https://doi.org/10.1088/0022-3727/16/2/014.

[42] M.I. Boulos, New frontiers in thermal plasma processing, Pure and Applied Chemistry. 68 (1996) 1007–1010. https://doi.org/10.1351/pac199668051007.

[43] R. Knight, R.W. Smith, D. Apelian, Application of plasma arc melting technology to processing of reactive metals, International Materials Reviews. 36 (1991) 221–252. https://doi.org/10.1179/imr.1991.36.1.221.

[44] J.M. Oh, K.M. Roh, J.W. Lim, Brief review of removal effect of hydrogen-plasma arc melting on refining of pure titanium and titanium alloys, Int J Hydrogen Energy. 41 (2016) 23033–23041. https://doi.org/10.1016/j.ijhydene.2016.09.082.

[45] S. Samal, K.K. Rao, P.S. Mukherjee, T.K. Mukherjee, Statistical modelling studies on leachability of titania-rich slag obtained from plasma melt separation of metallized ilmenite, Chemical Engineering Research and Design. 86 (2008) 187–191. https://doi.org/10.1016/j.cherd.2007.10.018.

[46] C. Alemany, C. Trassy, B. Pateyron, K.-I. Li, Y. Delannoy, Refining of metallurgical-grade silicon by inductive plasma, Solar Energy Materials & Solar Cells. 72 (2002) 41–48.

[47] I.N. Kravchenko, S. v. Kartsev, V. Kolomeichenko, Y. Kuznetsov, S.N. Perevislov, Markov, Metallurgical Features of Plasma Surfacing with Powder Hard Alloy with Addition of Aluminum Powder, Metallurgist. 64 (2021) 1077–1085. https://doi.org/10.1007/s11015-021-01089-x.

[48] J.F. Lancaster, The Physic of Welding, Phys. Technol. 15 (1984).

[49] S. Ramakrishnan, M. Gershenzon, F. Polivka, T.N. Kearney, M.W. Rogozinski, Plasma generation for the plasma cutting process, IEEE Transactions on Plasma Science. 25 (1997) 937–946. https://doi.org/10.1109/27.649600.

[50] V.A. Nemchinsky, W.S. Severance, What we know and what we do not know about plasma arc cutting, J Phys D Appl Phys. 39 (2006). https://doi.org/10.1088/0022-3727/39/22/R01.

[51] D.J. Thomas, Optimising plasma cut-Edge properties for improving the durability of bridge structures, International Journal of Steel Structures. 11 (2011) 481–493. https://doi.org/10.1007/s13296-011-4007-6.

[52] A.P. Hoult, I.R. Pashby, K. Chan, Fine plasma cutting of advanced aerospace materials, J Mater Process Technol. 48 (1995) 825–831.

[53] A. Rzeźnikiewicz, Cost comparison between oxyfuel and plasma cutting low alloy steel, 63 (2014) 81–85.

[54] C.S. Wu, L. Wang, W.J. Ren, X.Y. Zhang, Plasma arc welding: Process, sensing, control and modeling, J Manuf Process. 16 (2014) 74–85. https://doi.org/10.1016/j.jmapro.2013.06.004.

[55] P. Fauchais, M. Vardelle, Plasma spraying: present and future, Pure & Appl. Chem. 66 (1994) 1247–1258.

[56] R. Fernández-Pacheco, M. Arruebo, C. Marquina, R. Ibarra, J. Arbiol, J. Santamaría, Highly magnetic silica-coated iron nanoparticles prepared by the arc-discharge method, Nanotechnology. 17 (2006) 1188–1192. https://doi.org/10.1088/0957-4484/17/5/004.

[57] R. Hui, Z. Wang, O. Kesler, L. Rose, J. Jankovic, S. Yick, R. Maric, D. Ghosh, Thermal plasma spraying for SOFCs: Applications, potential advantages, and challenges, J Power Sources. 170 (2007) 308–323. https://doi.org/10.1016/j.jpowsour.2007.03.075.

[58] L. Pawlowski, P. Fauchais, Thermally Sprayed Coatings for Electrical and Electronic Applications, Materials Science Forum. 140–142 (1993) 497–520. https://doi.org/10.4028/www.scientific.net/msf.140-142.497.

[59] P. Fauchais, Understanding plasma spraying, J Phys D Appl Phys. 37 (2004). https://doi.org/10.1088/0022-3727/37/9/R02.

[60] M. Boulos, Plasma power can make better powders, Metal Powder Report. 59 (2004) 16–21. https://doi.org/10.1016/S0026-0657(04)00153-5.

[61] J.H. Seo, D.U. Kim, J.S. Nam, S.H. Hong, S.B. Sohn, S.M. Song, Radio frequency thermal

plasma treatment for size reduction and spheroidization of glass powders used in ceramic electronic devices, Journal of the American Ceramic Society. 90 (2007) 1717–1722. https://doi.org/10.1111/j.1551-2916.2007.01645.x.

[62] S. Samal, Synthesis of TiO2 Nanoparticles from Ilmenite Through the Mechanism of Vapor-Phase Reaction Process by Thermal Plasma Technology, J Mater Eng Perform. 27 (2018) 2622–2628. https://doi.org/10.1007/s11665-017-3060-5.

[63] J. Heberlein, A.B. Murphy, Thermal plasma waste treatment, J Phys D Appl Phys. 41 (2008). https://doi.org/10.1088/0022-3727/41/5/053001.

[64] B. Assamoi, Y. Lawryshyn, The environmental comparison of landfilling vs. incineration of MSW accounting for waste diversion, (2011). https://doi.org/10.1016/j.wasman.2011.10.023.

[65] M. Tendler, P. Rutberg, G. van Oost, Plasma based waste treatment and energy production, Plasma Phys Control Fusion. 47 (2005). https://doi.org/10.1088/0741-3335/47/5A/016.

[66] A. Bosmans, I. Vanderreydt, D. Geysen, L. Helsen, The crucial role of Waste-to-Energy technologies in enhanced landfill mining: a technology review, J Clean Prod. 55 (2013) 10–23. https://doi.org/10.1016/J.JCLEPRO.2012.05.032.

[67] B. Ruj, S. Ghosh, Technological aspects for thermal plasma treatment of municipal solid waste—A review, Fuel Processing Technology. 126 (2014) 298–308. https://doi.org/10.1016/J.FUPROC.2014.05.011.

[68] M. Hlina, M. Hrabovsky, T. Kavka, M. Konrad, Production of high quality syngas from argon/water plasma gasification of biomass and waste, Waste Management. 34 (2014) 63–66. https://doi.org/10.1016/J.WASMAN.2013.09.018.

[69] D. Panepinto, G. Genon, Solid Waste and Biomass Gasification: Fundamental Processes and Numerical Simulation, Chem Eng Trans. 24 (2011) 25–30.

[70] C.-Y.W. Pratim Biswas, Nanoparticles and the environment, J Air Waste Manage Assoc. 55 (2005) 708–746. https://doi.org/10.1080/10473289.2005.10464656.

[71] R.H. Kodama, Magnetic nanoparticles, J Magn Magn Mater. 200 (1999) 359–372. https://doi.org/10.1016/S0304-8853(99)00347-9.

[72] C.M. Welch, R.G. Compton, The use of nanoparticles in electroanalysis: A review, Anal Bioanal Chem. 384 (2006) 601–619. https://doi.org/10.1007/s00216-005-0230-3.

[73] X. Huang, M.A. El-Sayed, Gold nanoparticles: Optical properties and implementations in cancer diagnosis and photothermal therapy, J Adv Res. 1 (2010) 13–28. https://doi.org/10.1016/J.JARE.2010.02.002.

[74] T. Ishida, T. Murayama, A. Taketoshi, M. Haruta, Importance of Size and Contact Structure of Gold Nanoparticles for the Genesis of Unique Catalytic Processes, Chem Rev. 120 (2020) 464–525. https://doi.org/10.1021/acs.chemrev.9b00551.

[75] O. v Salata, Applications of nanoparticles in biology and medicine, Journal of Nanobiotechnolog. 2 (2004) 1–6. http://www.jnanobiotechnology.com/content/2/1/3.

[76] S. Panigrahi, S. Kundu, K. Ghosh, S. Nath, T. Pal, General method of synthesis for metal nanoparticles, Journal of Nanoparticle Research. 6 (2004) 411–414.

[77] A.H. Lu, E.L. Salabas, F. Schüth, Magnetic nanoparticles: Synthesis, protection, functionalization, and application, Angewandte Chemie - International Edition. 46 (2007) 1222–1244. https://doi.org/10.1002/anie.200602866.

[78] K.N. Thakkar, S.S. Mhatre, R.Y. Parikh, Biological synthesis of metallic nanoparticles, Nanomedicine. 6 (2010) 257–262. https://doi.org/10.1016/J.NANO.2009.07.002.

[79] M. Shigeta, T. Watanabe, Two-dimensional analysis of nanoparticle formation in induction thermal plasmas with counterflow cooling, Thin Solid Films. 516 (2008) 4415–4422. https://doi.org/10.1016/j.tsf.2007.10.022.

[80] J.H. Seo, B.G. Hong, Thermal plasma synthesis of nano-sized powders, Nuclear Engineering and Technology. 44 (2012) 9–20. https://doi.org/10.5516/NET.77.2012.002.

[81] A.M. FUDOLIG Hiroshi NOGAM, J. Yag, M. Manila Philippines, Prediction of Generation Rates In “Reactive Arc Plasma” Ultrafine Powder Production Process, ISIJ International. 37 (1997) 641–646.

[82] Y.I.Y.E.S.H. and M.K. T. Araya, Arc apparatus for producing ultrafine particles, 4,732,369, 1988.

[83] M. Shigeta, A.B. Murphy, Thermal plasmas for nanofabrication, J Phys D Appl Phys. 44 (2011). https://doi.org/10.1088/0022-3727/44/17/174025.

[84] D.W. Kim, T.H. Kim, S. Choi, K.S. Kim, D.W. Park, Preparation of silica coated iron oxide nanoparticles using non-transferred arc plasma, Advanced Powder Technology. 23 (2012) 701–707. https://doi.org/10.1016/J.APT.2011.09.001.

[85] H.P. Li, E. Pfender, Three dimensional modeling of the plasma spray process, Journal of Thermal Spray Technology. 16 (2007) 245–260. https://doi.org/10.1007/s11666-007-9023-x.

[86] M. Tanaka, T. Watanabe, Mechanism of enhanced vaporization from molten metal surface by argon-hydrogen Arc plasma, Jpn J Appl Phys. 52 (2013). https://doi.org/10.7567/JJAP.52.076201.

[87] T. Watanabe, K. Yatsuda, Y. Yao, T. Yano, T. Matuura, Innovative in-flight glass-melting technology using thermal plasmas, in: Pure and Applied Chemistry, 2010: pp. 1337–1351. https://doi.org/10.1351/PAC-CON-09-09-19.

[88] S.L. Girshick, C.P. Chiu, R. Muno, C.Y. Wu, L. Yang, S.K. Singh, P.H. McMurry, Thermal plasma synthesis of ultrafine iron particles, J Aerosol Sci. 24 (1993) 367–382. https://doi.org/10.1016/0021-8502(93)90009-X.

[89] M. Shigeta, T. Watanabe, H. Nishiyama, Numerical investigation for nano-particle synthesis in an RF inductively coupled plasma, Thin Solid Films. 457 (2004) 192–200. https://doi.org/10.1016/J.TSF.2003.12.020.

[90] M.A. El-Sayed, Some interesting properties of metals confined in time and nanometer space of different shapes, Acc Chem Res. 34 (2001) 257–264. https://doi.org/10.1021/ar960016n.

[91] D.L. Huber, Synthesis, properties, and applications of iron nanoparticles, Small. 1 (2005) 482–501. https://doi.org/10.1002/smll.200500006.

[92] T. Yoshida, K. Akashi, Preparation of Ultrafine Iron Particles using an RF Plasma, 1981.

[93] T. Yoshida, K. Akashi, Particle heating in a radio-frequency plasma torch, J Appl Phys. 48 (1977) 2252–2260. https://doi.org/10.1063/1.324036.

[94] M. Shinde, A. Pawar, S. Karmakar, T. Seth, V. Raut, S. Rane, S. Bhoraskar, D. Amalnerkar, Uncapped silver nanoparticles synthesized by DC arc thermal plasma technique for conductor paste formulation, Journal of Nanoparticle Research. 11 (2009) 2043–2047. https://doi.org/10.1007/s11051-008-9569-7.

[95] S.M. Wentworth, S. Member, B.L. Dillaman, S. Member, J.R. Chadwick, C.D. Ellis, R. Wayne Johnson, Attenuation in Silver-Filled Conductive Epoxy Interconnects, 1997.

[96] Y. Li, P. Leung, L. Yao, Q.W. Song, E. Newton, Antimicrobial effect of surgical masks coated with nanoparticles, Journal of Hospital Infection. 62 (2006) 58–63. https://doi.org/10.1016/J.JHIN.2005.04.015.

[97] M.M. Mench, K.K. Kuo, C.L. Yeh, Y.C. Lu, Comparison of Thermal Behavior of Regular and Ultra-fine Aluminum Powders Alex Made from Plasma Explosion Process, Combustion Science and Technology. 135 (1998) 269–292. https://doi.org/10.1080/00102209808924161.

[98] Y.S. Kwon, A.A. Gromov, J.I. Strokova, Passivation of the surface of aluminum nanopowders by protective coatings of the different chemical origin, Appl Surf Sci. 253 (2007) 5558–5564. https://doi.org/10.1016/J.APSUSC.2006.12.124.

[99] V.L. Mathe, V. Varma, S. Raut, A.K. Nandi, A. Pant, H. Prasanth, R.K. Pandey, S. v. Bhoraskar, A.K. Das, Enhanced active aluminum content and thermal behaviour of nano-aluminum particles passivated during synthesis using thermal plasma route, Appl Surf Sci. 368 (2016) 16–26. https://doi.org/10.1016/J.APSUSC.2016.01.246.

[100] K.-I. Sugimura, K. Hirao, Effect of a BaTiO3 nanoparticle additive on the quality of thin-film Ni electrodes in MLCC, Journal of the Ceramic Society of Japan. 117 (2009) 1039–1043.

[101] Y.M. Kim, K.H. Kim, B. Kim, H. Choi, Size and morphology manipulation of nickel nanoparticle in inductively coupled thermal plasma synthesis, J Alloys Compd. 658 (2016)

824–831. https://doi.org/10.1016/J.JALLCOM.2015.10.136.

[102] M. Shigeta, T. Watanabe, Numerical investigation of cooling effect on platinum nanoparticle formation in inductively coupled thermal plasmas, J Appl Phys. 103 (2008). https://doi.org/10.1063/1.2903918.

[103] P. Raveendran, J. Fu, S.L. Wallen, A simple and "green" method for the synthesis of Au, Ag, and Au–Ag alloy nanoparticles, Green Chemistry. 8 (2006) 34–38. https://doi.org/10.1039/b512540e.

[104] S. Rohart, C. Raufast, L. Favre, E. Bernstein, E. Bonet, V. Dupuis, Magnetic anisotropy of Cox Pt1-x clusters embedded in a matrix: Influences of the cluster chemical composition and the matrix nature, Phys Rev B Condens Matter Mater Phys. 74 (2006). https://doi.org/10.1103/PhysRevB.74.104408.

[105] C. Antoniak, J. Lindner, M. Spasova, D. Sudfeld, M. Acet, M. Farle, K. Fauth, U. Wiedwald, H.G. Boyen, P. Ziemann, F. Wilhelm, A. Rogalev, S. Sun, Enhanced orbital magnetism in Fe50Pt50 nanoparticles, Phys Rev Lett. 97 (2006). https://doi.org/10.1103/PhysRevLett.97.117201.

[106] N.S. Kanhe, A. Kumar, S.M. Yusuf, A.B. Nawale, S.S. Gaikwad, S.A. Raut, S. v. Bhoraskar, S.Y. Wu, A.K. Das, V.L. Mathe, Investigation of structural and magnetic properties of thermal plasma-synthesized Fe1−xNix alloy nanoparticles, J Alloys Compd. 663 (2016) 30–40. https://doi.org/10.1016/J.JALLCOM.2015.11.190.

[107] T. Hasegawa, S. Kanatani, M. Kazaana, K. Takahashi, K. Kumagai, M. Hirao, S. Ishio, Conversion of FeCo from soft to hard magnetic material by lattice engineering and nanopatterning, Sci Rep. 7 (2017). https://doi.org/10.1038/s41598-017-13602-x.

[108] G.S. Chaubey, C. Barcena, N. Poudyal, C. Rong, J. Gao, S. Sun, J.P. Liu, Synthesis and stabilization of FeCo nanoparticles, J Am Chem Soc. 129 (2007) 7214–7215. https://doi.org/10.1021/ja0708969.

[109] Y. Hirayama, K. Takagi, Evaluation of compositional homogeneity of Fe-Co alloy nanoparticles prepared by thermal plasma synthesis, J Alloys Compd. 792 (2019) 594–598. https://doi.org/10.1016/J.JALLCOM.2019.04.083.

[110] Y. Hirayama, K. Suzuki, W. Yamaguchi, K. Takagi, Cold welding behavior of fine bare aluminum powders prepared by new low oxygen induction thermal plasma system, J Alloys Compd. 768 (2018) 608–612. https://doi.org/10.1016/J.JALLCOM.2018.07.275.

[111] K. Park, Y. Hirayama, M. Shigeta, Z. Liu, M. Kobashi, K. Takagi, Anisotropic Sm-Co nanopowder prepared by induction thermal plasma, J Alloys Compd. 882 (2021) 160633. https://doi.org/10.1016/J.JALLCOM.2021.160633.

[112] J.H. Lee, Y.C. Shin, S.M. Lee, O.S. Jin, S.H. Kang, S.W. Hong, C.M. Jeong, J.B. Huh, D.W. Han, Enhanced Osteogenesis by Reduced Graphene Oxide/Hydroxyapatite

Nanocomposites, Sci Rep. 5 (2015). https://doi.org/10.1038/srep18833.

[113] A. Kazimirov, D.H. Bilderback, R. Huang, A. Sirenko, A. Ougazzaden, Microbeam high-resolution diffraction and x-ray standing wave methods applied to semiconductor structures, J Phys D Appl Phys. 37 (2004). https://doi.org/10.1088/0022-3727/37/4/L01.

[114] M. Shigeta, T. Watanabe, Effect of saturation pressure difference on metal-silicide nanopowder formation in thermal plasma fabrication, Nanomaterials. 6 (2016). https://doi.org/10.3390/nano6030043.

[115] G. Oskam, Metal oxide nanoparticles: Synthesis, characterization and application, in: J Solgel Sci Technol, 2006: pp. 161–164. https://doi.org/10.1007/s10971-005-6621-2.

[116] P.K. Stoimenov, R.L. Klinger, G.L. Marchin, K.J. Klabunde, Metal oxide nanoparticles as bactericidal agents, Langmuir. 18 (2002) 6679–6686. https://doi.org/10.1021/la0202374.

[117] M.R. Hoffmann, S.T. Martin, W. Choi, D.W. Bahnemann1', W.M. Keck, Environmental Applications of Semiconductor Photocatalysis, 1995. https://pubs.acs.org/sharingguidelines.

[118] G. Ren, D. Hu, E.W.C. Cheng, M.A. Vargas-Reus, P. Reip, R.P. Allaker, Characterisation of copper oxide nanoparticles for antimicrobial applications, Int J Antimicrob Agents. 33 (2009) 587–590. https://doi.org/10.1016/J.IJANTIMICAG.2008.12.004.

[119] R. Ye, J.G. Li, T. Ishigaki, Controlled synthesis of alumina nanoparticles using inductively coupled thermal plasma with enhanced quenching, Thin Solid Films. 515 (2007) 4251–4257. https://doi.org/10.1016/J.TSF.2006.02.050.

[120] G.D. Dhamale, V.L. Mathe, S. v. Bhoraskar, S.N. Sahasrabudhe, S. Ghorui, Synthesis and characterization of Nd_2O_3 nanoparticles in a radiofrequency thermal plasma reactor, Nanotechnology. 27 (2016). https://doi.org/10.1088/0957-4484/27/8/085603.

[121] R.A. Karaballi, Y.E. Monfared, M. Dasog, Overview of Synthetic Methods to Prepare Plasmonic Transition-Metal Nitride Nanoparticles, Chemistry - A European Journal. 26 (2020) 8499–8505. https://doi.org/10.1002/chem.201905217.

[122] A. v. Samokhin, V.A. Sinaiskii, N. v. Alekseev, E. v. Troitskaya, Y. v. Tsvetkov, Production of titanium nitride nanopowder from titanium hydride based on synthesis in thermal plasma, Inorganic Materials: Applied Research. 5 (2014) 224–229. https://doi.org/10.1134/S2075113314030149.

[123] Y. Koltypin, X. Cao, R. Prozorov, J. Balogh, D. Kaptasc, A. Gedanken, Sonochemical synthesis of iron nitride nanoparticles, n.d.

[124] T.K. Kim, M. Takahashi, New magnetic material having ultrahigh magnetic moment, Appl Phys Lett. 20 (1972) 492–494. https://doi.org/10.1063/1.1654030.

[125] Z. Turgut, D.E. Ferguson, M.Q. Huang, W.E. Wallace, M.E. Mchenry, Thermal Plasma Synthesis of γ-FeNx, Nanoparticles as Precursors for the Fe16N2 Synthesis by Annealing,

(1999).

[126] Q. Zhang, L. Gao, Synthesis of nanocrystalline aluminum nitride by nitridation of δ-Al2O3 nanoparticles in flowing ammonia, Journal of the American Ceramic Society. 89 (2006) 415–421. https://doi.org/10.1111/j.1551-2916.2005.00715.x.

[127] Y. Cheng, M. Shigeta, S. Choi, T. Watanabe, Formation mechanism of titanium boride nanoparticles by RF induction thermal plasma, Chemical Engineering Journal. 183 (2012) 483–491. https://doi.org/10.1016/j.cej.2011.12.040.

[128] R.G. Munro, Material Properties of Titanium Diboride, n.d. http://www.nist.gov/jres.

[129] S. Li, X. Yang, H. Zhu, Y. Chen, Y. Liu, Investigation of amorphous CoB alloy as the anode catalyst for a direct borohydride fuel cell, J Power Sources. 196 (2011) 5858–5862. https://doi.org/10.1016/J.JPOWSOUR.2011.02.016.

[130] S. Choi, L.D.S. Lapitan, Y. Cheng, T. Watanabe, Synthesis of cobalt boride nanoparticles using RF thermal plasma, Advanced Powder Technology. 25 (2014) 365–371. https://doi.org/10.1016/J.APT.2013.06.002.

[131] M. Kim, J.-H. Oh, T.-H. Kim, Y.H. Lee, S.-H. Hong, S. Choi, Synthesis of Metal Boride Nanoparticles Using Triple Thermal Plasma Jet System, J Nanosci Nanotechnol. 19 (2019) 6264–6270. https://doi.org/10.1166/jnn.2019.17026.

[132] B.A. Herbert Beall, W.N. Lipscomb, C.O. Wilson, J.F. Ditter, W.J. Lehman, The nature of the nickel boride formed by the action of sodium borohydride on nickel salts, American Chemical Society, 1964. https://pubs.acs.org/sharingguidelines.

[133] N.G. Szwacki, The structure and hardness of the highest boride of tungsten, a borophene-based compound, Sci Rep. 7 (2017). https://doi.org/10.1038/s41598-017-04394-1.

[134] C. Nachiappan, L. Rangaraj, C. Divakar, V. Jayaram, Synthesis and densification of monolithic zirconium carbide by reactive hot pressing, Journal of the American Ceramic Society. 93 (2010) 1341–1346. https://doi.org/10.1111/j.1551-2916.2010.03608.x.

[135] L. Bai, H. Zhang, H. Jin, F. Yuan, S. Huang, J. Li, Radio-frequency atmospheric-pressure plasma synthesis of ultrafine ZrC powders, Int J Appl Ceram Technol. 10 (2013) E274–E281. https://doi.org/10.1111/j.1744-7402.2012.02816.x.

[136] L. Tong, R.G. Reddy, Synthesis of titanium carbide nano-powders by thermal plasma, Scr Mater. 52 (2005) 1253–1258. https://doi.org/10.1016/J.SCRIPTAMAT.2005.02.033.

[137] P. Huber, D. Manova, S. Mändl, B. Rauschenbach, Formation of TiN, TiC and TiCN by metal plasma immersion ion implantation and deposition, Surf Coat Technol. 174–175 (2003) 1243–1247. https://doi.org/10.1016/S0257-8972(03)00458-4.

[138] Y. Gotoh, K. Fujimura, M. Koike, Y. Ohkoshi, M. Nagura, K. Akamatsu, S. Deki, Synthesis of titanium carbide from a composite of TiO_2 nanoparticles/methyl cellulose by carbothermal reduction, Mater Res Bull. 36 (2001) 2263–2275.

https://doi.org/10.1016/S0025-5408(01)00713-9.

[139] G.H. Lee, S. Kang, Sintering of nano-sized WC–Co powders produced by a gas reduction–carburization process, J Alloys Compd. 419 (2006) 281–289. https://doi.org/10.1016/J.JALLCOM.2005.09.060.

[140] M. Wu, X. Lin, A. Hagfeldt, T. Ma, Low-Cost Molybdenum Carbide and Tungsten Carbide Counter Electrodes for Dye-Sensitized Solar Cells, Angewandte Chemie. 123 (2011) 3582–3586. https://doi.org/10.1002/ange.201006635.

[141] J.-H. Oh, M. Kim, Y.H. Lee, S.H. Hong, T.-H. Kim, S. Choi, Synthesis of Tungsten Carbide Nanomaterials in Triple DC Thermal Plasma Jet System, J Nanosci Nanotechnol. 19 (2019) 6277–6284. https://doi.org/10.1166/jnn.2019.17029.

[142] J.M. Mcenaney, R.E. Schaak, Solution synthesis of metal silicide nanoparticles, Inorg Chem. 54 (2015) 707–709. https://doi.org/10.1021/ic502394u.

[143] Y.-U. Kwon, M.A. Rzeznik, A. Guloy, J.D. Corbett, Impurity Stabilization of Phases with the Mn_5Si_3-Type Structure. Questions Regarding La_5Sn_3 and Zr_5Si_3, 1990. https://pubs.acs.org/sharingguidelines.

[144] M. Shigeta, T. Watanabe, Numerical analysis for co-condensation processes in silicide nanoparticle synthesis using induction thermal plasmas at atmospheric pressure conditions, J Mater Res. 20 (2005) 2801–2811. https://doi.org/10.1557/JMR.2005.0351.

[145] M. Shigeta, T. Watanabe, Two-directional nodal model for co-condensation growth of multicomponent nanoparticles in thermal plasma processing, Journal of Thermal Spray Technology. 18 (2009) 1022–1037. https://doi.org/10.1007/s11666-009-9316-3.

[146] M. Shigeta, T. Watanabe, Effect of precursor fraction on silicide nanopowder growth under thermal plasma conditions: A computational study, Powder Technol. 288 (2016) 191–201. https://doi.org/10.1016/j.powtec.2015.11.005.

[147] S.E. Rodil, A.C. Ferrari, J. Robertson, W.I. Milne, Raman and infrared modes of hydrogenated amorphous carbon nitride, J Appl Phys. 89 (2001) 5425–5430. https://doi.org/10.1063/1.1365076.

[148] K.J. Clay, S.P. Speakman, G.A.J. Amaratunga, S.R.P. Silva, Characterization of a-C:H:N deposition from CH_4/N_2 rf plasmas using optical emission spectroscopy, J Appl Phys. 79 (1996) 7227–7233. https://doi.org/10.1063/1.361439.

[149] Y. Mao, T.J. Park, S.S. Wong, Synthesis of classes of ternary metal oxide nanostructures, Chemical Communications. (2005) 5721–5735. https://doi.org/10.1039/b509960a.

[150] A. Jankeviciute, Z. Károly, N. v. Tarakina, J. Szépvölgyi, A. Kareiva, Synthesis and characterization of spherical amorphous alumo-silicate nanoparticles using RF thermal plasma method, J Non Cryst Solids. 359 (2013) 9–14. https://doi.org/10.1016/J.JNONCRYSOL.2012.09.025.

[151] X. Zhang, Z. Liu, M. Tanaka, T. Watanabe, Formation mechanism of amorphous silicon nanoparticles with additional counter-flow quenching gas by induction thermal plasma, Chem Eng Sci. 230 (2021) 116217. https://doi.org/10.1016/j.ces.2020.116217.

[152] H.L. Tuller, D.P. Button, D.R. Uhlmann, Fast ion transport in oxide glasses, J Non Cryst Solids. 40 (1980) 93–118. https://doi.org/10.1016/0022-3093(80)90096-4.

[153] J. L. Souquet, Ionic transport in amorphous solid electrolytes, Annu Rev Mater Res. 11 (1981) 211–231. https://doi.org/10.1080/00150199408244731.

[154] M.S. Whittingham, Mechanism of fast ion transport in solids, Electrochim Acta. 20 (1975) 575–583. https://doi.org/10.1016/0013-4686(75)80008-9.

[155] B. Zhang, R. Tan, L. Yang, J. Zheng, K. Zhang, S. Mo, Z. Lin, F. Pan, Mechanisms and properties of ion-transport in inorganic solid electrolytes, Energy Storage Mater. 10 (2018) 139–159. https://doi.org/10.1016/j.ensm.2017.08.015.

[156] Z. Liu, W. Fu, E.A. Payzant, X. Yu, Z. Wu, N.J. Dudney, J. Kiggans, K. Hong, A.J. Rondinone, C. Liang, Anomalous high ionic conductivity of nanoporous β-Li3PS4, J Am Chem Soc. 135 (2013) 975–978. https://doi.org/10.1021/ja3110895.

[157] K. Homma, M. Yonemura, T. Kobayashi, M. Nagao, M. Hirayama, R. Kanno, Crystal structure and phase transitions of the lithium ionic conductor Li3PS4, Solid State Ion. 182 (2011) 53–58. https://doi.org/10.1016/J.SSI.2010.10.001.

[158] P. Maldonado-Manso, E.R. Losilla, M. Martínez-Lara, M.A.G. Aranda, S. Bruque, F.E. Mouahid, M. Zahir, High lithium ionic conductivity in the $Li_{1+x}Al_xGe_yTi_{2-x-y}(PO_4)_3$ NASICON series, Chemistry of Materials. 15 (2003) 1879–1885. https://doi.org/10.1021/cm021717j.

[159] G.Y. Adachi, N. Imanaka, S. Tamura, Ionic conducting lanthanide oxides, Chem Rev. 102 (2002) 2405–2429. https://doi.org/10.1021/cr0103064.

[160] S. Stramare, V. Thangadurai, W. Weppner, Lithium Lanthanum Titanates: A Review, Chemistry of Materials. 15 (2003) 3974–3990. https://doi.org/10.1021/cm0300516.

[161] R.J. Charles, Polarization and diffusion in a silicate glass, J Appl Phys. 32 (1961) 1115–1126. https://doi.org/10.1063/1.1736169.

[162] R. Terai, R. Hayami, Ionic diffusion in glasses, J Non Cryst Solids. 18 (1975) 217–264. https://doi.org/10.1016/0022-3093(75)90022-8.

[163] M. Eom, S. Son, C. Park, S. Noh, W.T. Nichols, D. Shin, High performance all-solid-state lithium-sulfur battery using a Li2S-VGCF nanocomposite, Electrochim Acta. 230 (2017) 279–284. https://doi.org/10.1016/J.ELECTACTA.2017.01.155.

[164] J. Janek, W.G. Zeier, A solid future for battery development, Nat Energy. 1 (2016). https://doi.org/10.1038/nenergy.2016.141.

[165] C. Yang, K. Fu, Y. Zhang, E. Hitz, L. Hu, Protected Lithium-Metal Anodes in Batteries:

From Liquid to Solid, Advanced Materials. 29 (2017). https://doi.org/10.1002/adma.201701169.

[166] M. Nagao, A. Hayashi, M. Tatsumisago, T. Kanetsuku, T. Tsuda, S. Kuwabata, In situ SEM study of a lithium deposition and dissolution mechanism in a bulk-type solid-state cell with a Li_2S-P_2S_5 solid electrolyte, Physical Chemistry Chemical Physics. 15 (2013) 18600–18606. https://doi.org/10.1039/c3cp51059j.

[167] R. Garcia-Mendez, F. Mizuno, R. Zhang, T.S. Arthur, J. Sakamoto, Effect of Processing Conditions of $75Li_2S$-$25P_2S_5$ Solid Electrolyte on its DC Electrochemical Behavior, Electrochim Acta. 237 (2017) 144–151. https://doi.org/10.1016/J.ELECTACTA.2017.03.200.

[168] F. Han, J. Yue, X. Zhu, C. Wang, Suppressing Li Dendrite Formation in Li_2S-P_2S_5 Solid Electrolyte by LiI Incorporation, Adv Energy Mater. 8 (2018). https://doi.org/10.1002/aenm.201703644.

[169] Z. Wang, Y. Fu, Z. Zhang, S. Yuan, K. Amine, V. Battaglia, G. Liu, Application of Stabilized Lithium Metal Powder (SLMP®) in graphite anode – A high efficient prelithiation method for lithium-ion batteries, J Power Sources. 260 (2014) 57–61. https://doi.org/10.1016/J.JPOWSOUR.2014.02.112.

[170] A.C. Kozen, C.F. Lin, A.J. Pearse, M.A. Schroeder, X. Han, L. Hu, S.B. Lee, G.W. Rubloff, M. Noked, Next-Generation Lithium Metal Anode Engineering via Atomic Layer Deposition, ACS Nano. 9 (2015) 5884–5892. https://doi.org/10.1021/acsnano.5b02166.

[171] J. Zhao, Z. Lu, N. Liu, H.W. Lee, M.T. McDowell, Y. Cui, Dry-air-stable lithium silicide-lithium oxide core-shell nanoparticles as high-capacity prelithiation reagents, Nat Commun. 5 (2014). https://doi.org/10.1038/ncomms6088.

[172] J. Liang, X. Li, Y. Zhao, L. v. Goncharova, W. Li, K.R. Adair, M.N. Banis, Y. Hu, T.K. Sham, H. Huang, L. Zhang, S. Zhao, S. Lu, R. Li, X. Sun, An Air-Stable and Dendrite-Free Li Anode for Highly Stable All-Solid-State Sulfide-Based Li Batteries, Adv Energy Mater. 9 (2019). https://doi.org/10.1002/aenm.201902125.

[173] C.K. Chan, H. Peng, G. Liu, K. McIlwrath, X.F. Zhang, R.A. Huggins, Y. Cui, High-performance lithium battery anodes using silicon nanowires, Nat Nanotechnol. 3 (2008) 31–35. https://doi.org/10.1038/nnano.2007.411.

[174] W.J. Zhang, Lithium insertion/extraction mechanism in alloy anodes for lithium-ion batteries, J Power Sources. 196 (2011) 877–885. https://doi.org/10.1016/j.jpowsour.2010.08.114.

[175] A. Anani, R.A. Huggins, Multinary alloy electrodes for solid state batteries I. A phase diagram approach for the selection and storage properties determination of candidate electrode materials, 1992.

[176] S. Jin, Y. Ye, Y. Niu, Y. Xu, H. Jin, J. Wang, Z. Sun, A. Cao, X. Wu, Y. Luo, H. Ji, L.-J. Wan, Solid−Solution-Based Metal Alloy Phase for Highly Reversible Lithium Metal Anode, J. Am. Chem. Soc. 142 (2020) 53. https://doi.org/10.1021/jacs.0c01811.

[177] T. Krauskopf, B. Mogwitz, C. Rosenbach, W.G. Zeier, J. Janek, Diffusion Limitation of Lithium Metal and Li–Mg Alloy Anodes on LLZO Type Solid Electrolytes as a Function of Temperature and Pressure, Adv Energy Mater. 9 (2019). https://doi.org/10.1002/aenm.201902568.

[178] D. Billaud, F.X. Henry, P. Willmann, Electrochemical Synthesis of Binary Graphite-Lithium Intercalation Compounds, Res. Bull. 28 (1993) 477–483.

[179] K. Takada, T. Inada, A. Kajiyama, H. Sasaki, S. Kondo, M. Watanabe, M. Murayama, R. Kanno, Solid-state lithium battery with graphite anode, Solid State Ion. 158 (2003) 269–274. www.elsevier.com/locate/ssi.

[180] Y. Jin Shan, Y. Inaguma, M. Itoh, The effect of electrostatic potentials on lithium insertion for perovskite oxides, Solid State Ion. 79 (1995) 245–251.

[181] Y. He, L. Jiang, T. Chen, Y. Xu, H. Jia, R. Yi, D. Xue, M. Song, A. Genc, C. Bouchet-Marquis, L. Pullan, T. Tessner, J. Yoo, X. Li, J.G. Zhang, S. Zhang, C. Wang, Progressive growth of the solid–electrolyte interphase towards the Si anode interior causes capacity fading, Nat Nanotechnol. 16 (2021) 1113–1120. https://doi.org/10.1038/s41565-021-00947-8.

[182] H. Wu, G. Chan, J.W. Choi, I. Ryu, Y. Yao, M.T. Mcdowell, S.W. Lee, A. Jackson, Y. Yang, L. Hu, Y. Cui, Stable cycling of double-walled silicon nanotube battery anodes through solid-electrolyte interphase control, Nat Nanotechnol. 7 (2012) 310–315. https://doi.org/10.1038/nnano.2012.35.

[183] Q. Ai, D. Li, J. Guo, G. Hou, Q. Sun, Q. Sun, X. Xu, W. Zhai, L. Zhang, J. Feng, P. Si, J. Lou, L. Ci, Artificial Solid Electrolyte Interphase Coating to Reduce Lithium Trapping in Silicon Anode for High Performance Lithium-Ion Batteries, Adv Mater Interfaces. 6 (2019). https://doi.org/10.1002/admi.201901187.

[184] P.G. Bruce, Solid-state chemistry of lithium power source, Chemical Communications. (1997) 1817–1824.

[185] H.S. Kim, B.W. Cho, W. il Cho, Cycling performance of $LiFePO_4$ cathode material for lithium secondary batteries, J Power Sources. 132 (2004) 235–239. https://doi.org/10.1016/j.jpowsour.2003.12.058.

[186] N. Ohta, K. Takada, L. Zhang, R. Ma, M. Osada, T. Sasaki, Enhancement of the high-rate capability of solid-state lithium batteries by nanoscale interfacial modification, Advanced Materials. 18 (2006) 2226–2229. https://doi.org/10.1002/adma.200502604.

[187] S.H. Jung, K. Oh, Y.J. Nam, D.Y. Oh, P. Brüner, K. Kang, Y.S. Jung, Li_3BO_3-Li_2CO_3:

Rationally Designed Buffering Phase for Sulfide All-Solid-State Li-Ion Batteries, Chemistry of Materials. 30 (2018) 8190–8200. https://doi.org/10.1021/acs.chemmater.8b03321.

[188] N. Ohta, K. Takada, I. Sakaguchi, L. Zhang, R. Ma, K. Fukuda, M. Osada, T. Sasaki, $LiNbO_3$-coated $LiCoO_2$ as cathode material for all solid-state lithium secondary batteries, Electrochem Commun. 9 (2007) 1486–1490. https://doi.org/10.1016/j.elecom.2007.02.008.

[189] S.M. Bak, E. Hu, Y. Zhou, X. Yu, S.D. Senanayake, S.J. Cho, K.B. Kim, K.Y. Chung, X.Q. Yang, K.W. Nam, Structural changes and thermal stability of charged $LiNi_xMn_yCo_zO_2$ cathode materials studied by combined in situ time-resolved XRD and mass spectroscopy, ACS Appl Mater Interfaces. 6 (2014) 22594–22601. https://doi.org/10.1021/am506712c.

[190] P. He, H. Yu, D. Li, H. Zhou, Layered lithium transition metal oxide cathodes towards high energy lithium-ion batteries, J Mater Chem. 22 (2012) 3680–3695. https://doi.org/10.1039/c2jm14305d.

[191] C. Liang, F. Kong, R.C. Longo, K.C. Santosh, J.S. Kim, S.H. Jeon, S.A. Choi, K. Cho, Unraveling the Origin of Instability in Ni-Rich $LiNi_{1-2x}Co_xMn_xO_2$ (NCM) Cathode Materials, Journal of Physical Chemistry C. 120 (2016) 6383–6393. https://doi.org/10.1021/acs.jpcc.6b00369.

[192] A. Sakuda, A. Hayashi, M. Tatsumisago, Sulfide solid electrolyte with favorable mechanical property for all-solid-state lithium battery, Sci Rep. 3 (2013) 2–6. https://doi.org/10.1038/srep02261.

[193] Y.-P. Hong, Crystal Structure and Ionic Conductivity of $Li_{14}Zn(GeO_4)_4$ and Other New Li^+ Superionic Conductors, Mat. Res. Bul. 13 (1978) 117–124.

[194] R. Kanno, T. Hata, Y. Kawamoto, M. Irie, Synthesis of a new lithium ionic conductor, thio-LISICON-lithium germanium sulfide system, Solid State Ion. 130 (2000) 97–104. www.elsevier.com/locate/ssi.

[195] M. Murayama, R. Kanno, M. Irie, S. Ito, T. Hata, N. Sonoyama, Y. Kawamoto, Synthesis of new lithium ionic conductor thio-LISICON - Lithium silicon sulfides system, J Solid State Chem. 168 (2002) 140–148. https://doi.org/10.1006/jssc.2002.9701.

[196] F. Zheng, M. Kotobuki, S. Song, M.O. Lai, L. Lu, Review on solid electrolytes for all-solid-state lithium-ion batteries, J Power Sources. 389 (2018) 198–213. https://doi.org/10.1016/j.jpowsour.2018.04.022.

[197] S. Song, J. Lu, F. Zheng, H.M. Duong, L. Lu, A facile strategy to achieve high conduction and excellent chemical stability of lithium solid electrolytes, RSC Adv. 5 (2015) 6588–6594. https://doi.org/10.1039/c4ra11287c.

[198] Y. Deng, C. Eames, B. Fleutot, R. David, J.N. Chotard, E. Suard, C. Masquelier, M.S.

Islam, Enhancing the Lithium Ion Conductivity in Lithium Superionic Conductor (LISICON) Solid Electrolytes through a Mixed Polyanion Effect, ACS Appl Mater Interfaces. 9 (2017) 7050–7058. https://doi.org/10.1021/acsami.6b14402.

[199] C.L.M.I. and T.N. Yoshiyuki Inaguma, High Ionic Conductivity in Lithium Lanthanum Titanate, Solid State Communication. 86 (1993) 689–693.

[200] C.H. Chen, S. Xie, E. Sperling, A.S. Yang, G. Henriksen, K. Amine, Stable lithium-ion conducting perovskite lithium-strontium-tantalum- zirconium-oxide system, Solid State Ion. 167 (2004) 263–272. https://doi.org/10.1016/j.ssi.2004.01.008.

[201] HM Kasper, Series of rare earth garnets $Ln^{3+}{}_3M_2Li^{+}{}_3O_{12}$ (M= Te, W), Inorg Chem. 8 (1969) 1000–1002.

[202] V. Thangadurai, W. Weppner, $Li_6ALa_2Ta_2O_{12}$ (A=Sr, Ba): Novel garnet-like oxides for fast lithium ion conduction, Adv Funct Mater. 15 (2005) 107–112. https://doi.org/10.1002/adfm.200400044.

[203] C. Bernuy-Lopez, W. Manalastas, J.M. Lopez Del Amo, A. Aguadero, F. Aguesse, J.A. Kilner, Atmosphere controlled processing of Ga-substituted garnets for high li-ion conductivity ceramics, Chemistry of Materials. 26 (2014) 3610–3617. https://doi.org/10.1021/cm5008069.

[204] Z.A. Grady, C.J. Wilkinson, C.A. Randall, J.C. Mauro, Emerging Role of Non-crystalline Electrolytes in Solid-State Battery Research, Front Energy Res. 8 (2020). https://doi.org/10.3389/fenrg.2020.00218.

[205] L.L. Hench, J.K. West, The Sol-Gel Process, Chem. Rev. 90 (1990) 33–72. https://pubs.acs.org/sharingguidelines.

[206] K. Kajihara, Recent advances in sol–gel synthesis of monolithic silica and silica-based glasses, Journal of Asian Ceramic Societies. 1 (2013) 121–133. https://doi.org/10.1016/J.JASCER.2013.04.002.

[207] J. Zarzycki, Past and Present of Sol-Gel Science and Technology, J Solgel Sci Technol. 11 (1996) 17–22.

[208] S.P. Mukherjee, Sol-gel processes in glass science and technology, J Non Cryst Solids. 42 (1980) 477–488. https://doi.org/10.1016/0022-3093(80)90046-0.

[209] S.W. Lee, R.A.C. Sr, The infrared and Raman spectra of ZrO_2-SiO_2 glasses prepared by a sol-gel process, J Mater Sci. 23 (1988) 2951–2959.

[210] C. Fernfindez-Lorenzo, L. Esquivias, F. Taulelle, Sol-gel synthesis of SiO_2-P_2O_5 glasses, J Non Cryst Solids. 176 (1994) 189–199.

[211] F. Sharifianjazi, N. Parvin, M. Tahriri, Synthesis and characteristics of sol-gel bioactive SiO_2-P_2O_5-CaO-Ag_2O glasses, J Non Cryst Solids. 476 (2017) 108–113. https://doi.org/10.1016/J.JNONCRYSOL.2017.09.035.

[212] E. Fiume, C. Migneco, E. Verné, F. Baino, Comparison between bioactive sol-gel and melt-derived glasses/glass-ceramics based on the multicomponent SiO_2-P_2O_5-CaO-MgO-Na_2O-K_2O System, Materials. 13 (2020). https://doi.org/10.3390/ma13030540.

[213] Y. Chen, M. Bibole, R. le Hazif, C. Martin, Ball-milling-induced amorphization in Ni_xZr_y compounds: A parametric study, Phys Rev B. 48 (1993).

[214] G. Gorrasi, A. Sorrentino, Mechanical milling as a technology to produce structural and functional bio-nanocomposites, Green Chemistry. 17 (2015) 2610–2625. https://doi.org/10.1039/c5gc00029g.

[215] J. Eckert, L. Schultz, K. Urban, Formation of quasicrystalline and amorphous phases in mechanically alloyed Al-based and Ti-Ni-based alloys, Acta Metallurgica et Materialia. 39 (1991) 1497–1506. https://doi.org/10.1016/0956-7151(91)90235-S.

[216] C. Suryanarayana, Mechanical alloying and milling, Prog Mater Sci. 46 (2001) 1–184. https://doi.org/10.1016/S0079-6425(99)00010-9.

[217] M. Sherif El-Eskandarany, K. Sumiyama, K. Suzuki, Crystalline-to-amorphous phase transformation in mechanically alloyed Fe50W50 powders, Acta Mater. 45 (1997) 1175–1187. https://doi.org/10.1016/S1359-6454(96)00205-4.

[218] H. Huang, P.G. McCormick, Effect of milling conditions on the synthesis of chromium carbides by mechanical alloying, J Alloys Compd. 256 (1997) 258–262. https://doi.org/10.1016/S0925-8388(96)03010-1.

[219] L. Aymard, A. Delahaye-Vidal, F. Portemer, F. Disma, Study of the formation reactions of silver-palladium alloys by grinding and post-milling isothermal annealing, J Alloys Compd. 238 (1996) 116–127. https://doi.org/10.1016/0925-8388(95)02174-4.

[220] S.-J. Choi, S.-H. Lee, Y.-C. Ha, J.-H. Yu, C.-H. Doh, Y. Lee, J.-W. Park, S.-M. Lee, H.-C. Shin, Synthesis and Electrochemical Characterization of a Glass-Ceramic Li7P2S8I Solid Electrolyte for All-Solid-State Li-Ion Batteries, J Electrochem Soc. 165 (2018) A957–A962. https://doi.org/10.1149/2.0981805jes.

[221] L. Hallmann, P. Ulmer, M. Kern, Effect of microstructure on the mechanical properties of lithium disilicate glass-ceramics, J Mech Behav Biomed Mater. 82 (2018) 355–370. https://doi.org/10.1016/J.JMBBM.2018.02.032.

[222] N. Sharma, A. Dalvi, Mechanical milling assisted synthesis of novel $LiTi_2(PO_4)_3$-glass-ceramic nanocomposites, J Non Cryst Solids. 483 (2018) 126–133. https://doi.org/10.1016/J.JNONCRYSOL.2018.01.016.

[223] T.R. Anantharaman, C. Suryanarayana, Review: A Decade of Quenching from the Melt, J Mater Sci. 6 (1971) 1111–1135.

[224] G. Kaur, O.P. Pandey, K. Singh, D. Homa, B. Scott, G. Pickrell, A review of bioactive glasses: Their structure, properties, fabrication and apatite formation, J Biomed Mater Res

A. 102 (2014) 254–274. https://doi.org/10.1002/jbm.a.34690.

[225] A. Hayashi, K. Minami, F. Mizuno, M. Tatsumisago, Formation of Li^+ superionic crystals from the Li_2S-P_2S_5 melt-quenched glasses, J Mater Sci. 43 (2008) 1885–1889. https://doi.org/10.1007/s10853-007-2421-0.

[226] N. Nedelcu, V. Chiroiu, C. Rugină, L. Munteanu, R. Ioan, I. Girip, C. Dragne, Dielectric properties of GeSbSe glasses prepared by the conventional melt-quenching method, Results Phys. 16 (2020) 102856. https://doi.org/10.1016/J.RINP.2019.102856.

[227] M.H.M. Zaid, K.A. Matori, H.J. Quah, W.F. Lim, H.A.A. Sidek, M.K. Halimah, W.M.M. Yunus, Z.A. Wahab, Investigation on structural and optical properties of SLS–ZnO glasses prepared using a conventional melt quenching technique, Journal of Materials Science: Materials in Electronics. 26 (2015) 3722–3729. https://doi.org/10.1007/s10854-015-2891-9.

[228] G. Kaur, P. Sharma, V. Kumar, K. Singh, Assessment of in vitro bioactivity of SiO_2-BaO-ZnO-B_2O_3-Al_2O_3 glasses: An optico-analytical approach, Materials Science and Engineering: C. 32 (2012) 1941–1947. https://doi.org/10.1016/J.MSEC.2012.05.034.

[229] G. Kaur, O.P. Pandey, K. Singh, Interfacial study between high temperature SiO_2–B_2O_3–AO–La_2O_3 (A = Sr, Ba) glass seals and Crofer 22APU for solid oxide fuel cell applications, Int J Hydrogen Energy. 37 (2012) 6862–6874. https://doi.org/10.1016/J.IJHYDENE.2012.01.118.

[230] J.P. Malugani, G. Robert, Conductivite ionique dans les verres $LiPO_3LiX$ (X = I, Br, Cl), Mater Res Bull. 14 (1979) 1075–1081. https://doi.org/10.1016/0025-5408(79)90075-8.

[231] T. Hakari, M. Deguchi, K. Mitsuhara, T. Ohta, K. Saito, Y. Orikasa, Y. Uchimoto, Y. Kowada, A. Hayashi, M. Tatsumisago, Structural and Electronic-State Changes of a Sulfide Solid Electrolyte during the Li Deinsertion-Insertion Processes, Chemistry of Materials. 29 (2017) 4768–4774. https://doi.org/10.1021/acs.chemmater.7b00551.

[232] K. Minami, F. Mizuno, A. Hayashi, M. Tatsumisago, Lithium ion conductivity of the Li_2S-P_2S_5 glass-based electrolytes prepared by the melt quenching method, Solid State Ion. 178 (2007) 837–841. https://doi.org/10.1016/j.ssi.2007.03.001.

[233] A. Fukushima, A. Hayashi, H. Yamamura, M. Tatsumisago, Mechanochemical synthesis of high lithium ion conducting solid electrolytes in a Li_2S-P_2S_5-Li_3N system, Solid State Ion. 304 (2017) 85–89. https://doi.org/10.1016/J.SSI.2017.03.010.

[234] M. Yamashita, H. Yamanaka, Formation and ionic conductivity of Li_2S-GeS_2-Ga_2S_3 glasses and thin films, Solid State Ion. 158 (2003) 151–156. https://doi.org/10.1016/S0167-2738(02)00756-7.

[235] Y. Mo, S.P. Ong, G. Ceder, First principles study of the $Li_{10}GeP_2S_{12}$ lithium super ionic conductor material, in: Chemistry of Materials, 2012: pp. 15–17.

https://doi.org/10.1021/cm203303y.

[236] R.F. Bartholomew, D.M. Young, A.J.G. Ellison, Electrical properties of new glasses based on the Li_2S-SiS_2 system, J Non Cryst Solids. 256 (1999) 242–247. https://doi.org/10.1016/S0022-3093(99)00486-X.

[237] F. Han, A.S. Westover, J. Yue, X. Fan, F. Wang, M. Chi, D.N. Leonard, N.J. Dudney, H. Wang, C. Wang, High electronic conductivity as the origin of lithium dendrite formation within solid electrolytes, Nat Energy. 4 (2019) 187–196. https://doi.org/10.1038/s41560-018-0312-z.

[238] J.B. Bates, N.J. Dudney, G.R. Gruzalski, R.A. Zuhr, A. Choudhury, C.F. Luck, J.D. Robertson, Electrical properties of amorphous lithium electrolyte thin films, Solid State Ion. 53–56 (1992) 647–654. https://doi.org/10.1016/0167-2738(92)90442-R.

[239] J.B. Bates, N.J. Dudney, G.R. Gruzalski, R.A. Zuhr, A. Choudhury, C.F. Luck, J.D. Robertson, Fabrication and characterization of amorphous lithium electrolyte thin films and rechargeable thin-film batteries, 1993.

[240] V. Lacivita, N. Artrith, G. Ceder, Structural and Compositional Factors That Control the Li-Ion Conductivity in LiPON Electrolytes, Chemistry of Materials. 30 (2018) 7077–7090. https://doi.org/10.1021/acs.chemmater.8b02812.

[241] Y. Yoon, C. Park, J. Kim, D. Shin, Characterization of lithium borophosphate glass thin film electrolytes deposited by RF-magnetron sputtering for micro-batteries, Solid State Ion. 225 (2012) 636–640. https://doi.org/10.1016/J.SSI.2012.05.008.

[242] T. Famprikis, J. Galipaud, O. Clemens, B. Pecquenard, F. le Cras, Composition Dependence of Ionic Conductivity in LiSiPO(N) Thin-Film Electrolytes for Solid-State Batteries, ACS Appl Energy Mater. 2 (2019) 4782–4791. https://doi.org/10.1021/acsaem.9b00415.

[243] D.L. Xiao, J. Tong, Y. Feng, G.H. Zhong, W.J. Li, C.L. Yang, Improved performance of all-solid-state lithium batteries using LiPON electrolyte prepared with Li-rich sputtering target, Solid State Ion. 324 (2018) 202–206. https://doi.org/10.1016/J.SSI.2018.07.011.

[244] S. v. Pershina, A.A. Raskovalov, B.D. Antonov, T. v. Yaroslavtseva, O.G. Reznitskikh, Y. v. Baklanova, E.D. Pletneva, Extreme behavior of Li-ion conductivity in the Li_2O-Al_2O3-P_2O_5 glass system, J Non Cryst Solids. 430 (2015) 64–72. https://doi.org/10.1016/j.jnoncrysol.2015.10.003.

[245] F. Moreau, A. Durán, F. Muñoz, Structure and properties of high Li_2O-containing aluminophosphate glasses, J Eur Ceram Soc. 29 (2009) 1895–1902. https://doi.org/10.1016/J.JEURCERAMSOC.2008.12.016.

[246] J. Fu, Superionic conductivity of glass-ceramics in the system Li_2O- Al_2O_3-TiO_2-P_2O_5, Solid State Ion. 96 (1997) 195–200. https://doi.org/10.1016/S0167-2738(97)00018-0.

[247] X. Xu, Z. Wen, X. Yang, J. Zhang, Z. Gu, High lithium ion conductivity glass-ceramics in Li_2O-Al_2O_3-TiO_2-P_2O_5 from nanoscaled glassy powders by mechanical milling, Solid State Ion. 177 (2006) 2611–2615. https://doi.org/10.1016/j.ssi.2006.04.010.

[248] A. López-Grande, R. Dagupati, P. Galán del Sastre, F. Muñoz, Ionic conductivity of Li_2O–P_2O_5 glasses from thermodynamic modeling of their chemical structure, Journal of the American Ceramic Society. 104 (2021) 5625–5635. https://doi.org/10.1111/jace.17962.

[249] K. Takada, Progress in solid electrolytes toward realizing solid-state lithium batteries, J Power Sources. 394 (2018) 74–85. https://doi.org/10.1016/J.JPOWSOUR.2018.05.003.

[250] E.A. Hayri, M. Greenblatt, The preparation and ionic conductivity of sol-gels in the Li_2O-P_2O_5-SiO_2 system, J Non Cryst Solids. 94 (1987) 387–401. https://doi.org/10.1016/S0022-3093(87)80073-X.

[251] A. Gaddam, A.R. Allu, S. Ganisetti, H.R. Fernandes, G.E. Stan, C.C. Negrila, A.P. Jamale, F. Mear, L. Montagne, J.M.F. Ferreira, Effect of Vanadium Oxide on the Structure and Li-Ion Conductivity of Lithium Silicate Glasses, Journal of Physical Chemistry C. 125 (2021) 16843–16857. https://doi.org/10.1021/acs.jpcc.1c05059.

[252] H.R. Fernandes, D.U. Tulyaganov, A. Goel, J.M.F. Ferreira, Structural characterisation and thermo-physical properties of glasses in the Li_2O-SiO_2-Al_2O_3-K_2O system, J Therm Anal Calorim. 103 (2011) 827–834. https://doi.org/10.1007/s10973-010-1049-5.

[253] R. Prasada Rao, T.D. Tho, S. Adams, Ion transport pathways in molecular dynamics simulated lithium silicate glasses, Solid State Ion. 181 (2010) 1–6. https://doi.org/10.1016/J.SSI.2009.12.003.

[254] C.H. Lee, K.H. Joo, J.H. Kim, S.G. Woo, H.J. Sohn, T. Kang, Y. Park, J.Y. Oh, Characterizations of a new lithium ion conducting Li_2O–SeO_2–B_2O_3 glass electrolyte, Solid State Ion. 149 (2002) 59–65. https://doi.org/10.1016/S0167-2738(02)00137-6.

[255] C.E. Kim, H.C. Hwang, M.Y. Yoon, B.H. Choi, H.J. Hwang, Fabrication of a high lithium ion conducting lithium borosilicate glass, J Non Cryst Solids. 357 (2011) 2863–2867. https://doi.org/10.1016/J.JNONCRYSOL.2011.03.022.

[256] V. Montouillout, H. Fan, L. del Campo, S. Ory, A. Rakhmatullin, F. Fayon, M. Malki, Ionic conductivity of lithium borate glasses and local structure probed by high resolution solid-sate NMR, J Non Cryst Solids. 484 (2018) 57–64. https://doi.org/10.1016/J.JNONCRYSOL.2018.01.020.

[257] C.H. Chen, K. Amine, Ionic conductivity, lithium insertion and extraction of lanthanum lithium titanate, Solid State Ion. 144 (2001) 51–57. https://doi.org/10.1016/S0167-2738(01)00884-0.

[258] Z. Zheng, H. Fang, F. Yang, Z.-K. Liu, Y. Wang, Amorphous $LiLaTiO_3$ as Solid Electrolyte Material, J Electrochem Soc. 161 (2014) A473–A479. https://doi.org/10.1149/2.006404jes.

[259] M.I. Boulos, P.L. Fauchais, E. Pfender, The Plasma State, in: Handbook of Thermal Plasmas, Springer International Publishing, 2016: pp. 1–53. https://doi.org/10.1007/978-3-319-12183-3_1-2.

[260] S. Samal, Thermal plasma technology: The prospective future in material processing, J Clean Prod. 142 (2017) 3131–3150. https://doi.org/10.1016/j.jclepro.2016.10.154.

[261] C. De, E. Langlois Bertrand, C. de Izarra, E. Langlois-Bertrand, Interaction between a CO2 laser beam and an atmospheric pressure argon plasma jet, (2009). https://www.researchgate.net/publication/267859157.

[262] K.S. Kim, T.H. Kim, Nanofabrication by thermal plasma jets: From nanoparticles to low-dimensional nanomaterials, J Appl Phys. 125 (2019). https://doi.org/10.1063/1.5060977.

[263] M. Shigeta, A.B. Murphy, Thermal plasmas for nanofabrication, J Phys D Appl Phys. 44 (2011). https://doi.org/10.1088/0022-3727/44/17/174025.

[264] M. Shoji, E.J. Cheng, T. Kimura, K. Kanamura, Recent progress for all solid state battery using sulfide and oxide solid electrolytes, J Phys D Appl Phys. 52 (2019). https://doi.org/10.1088/1361-6463/aaf7e2.

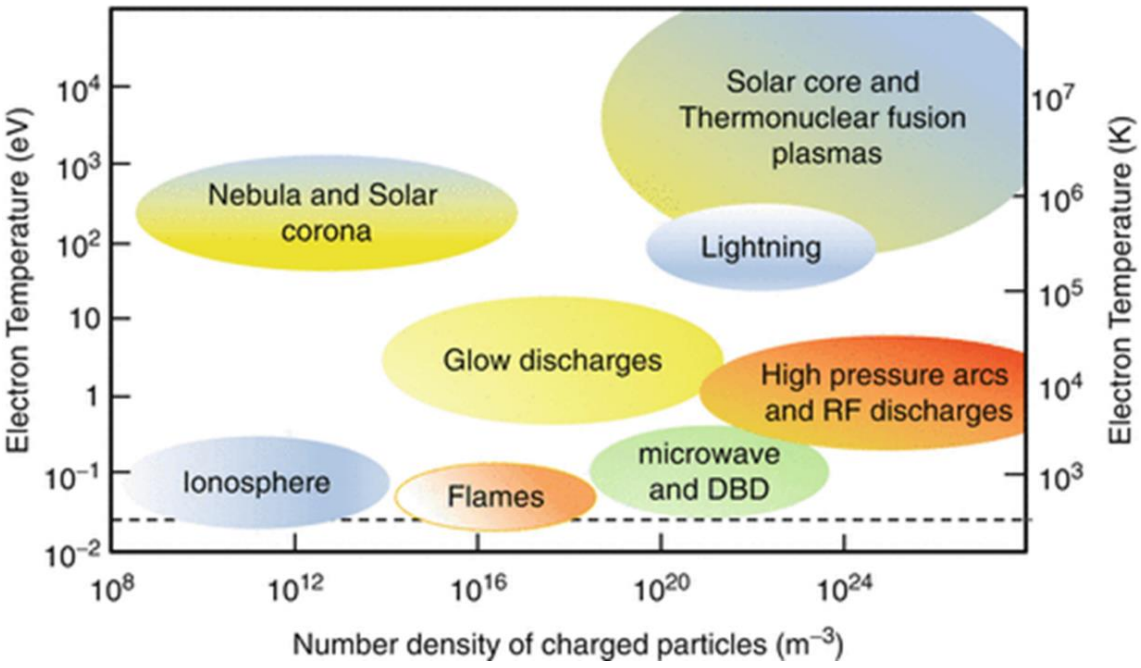

Fig. 1.1. The domains of plasma as the function of temperature and electron density [259].

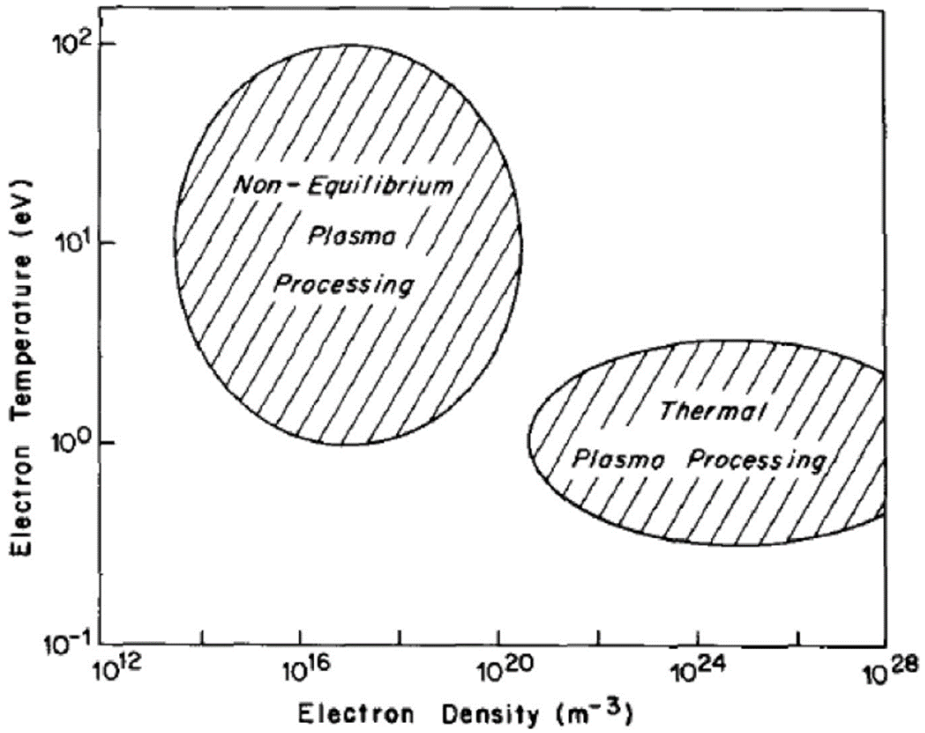

Fig. 1.2. The typical ranges of electron temperature rang with electron density for non-equilibrium and equilibrium plasma [260].

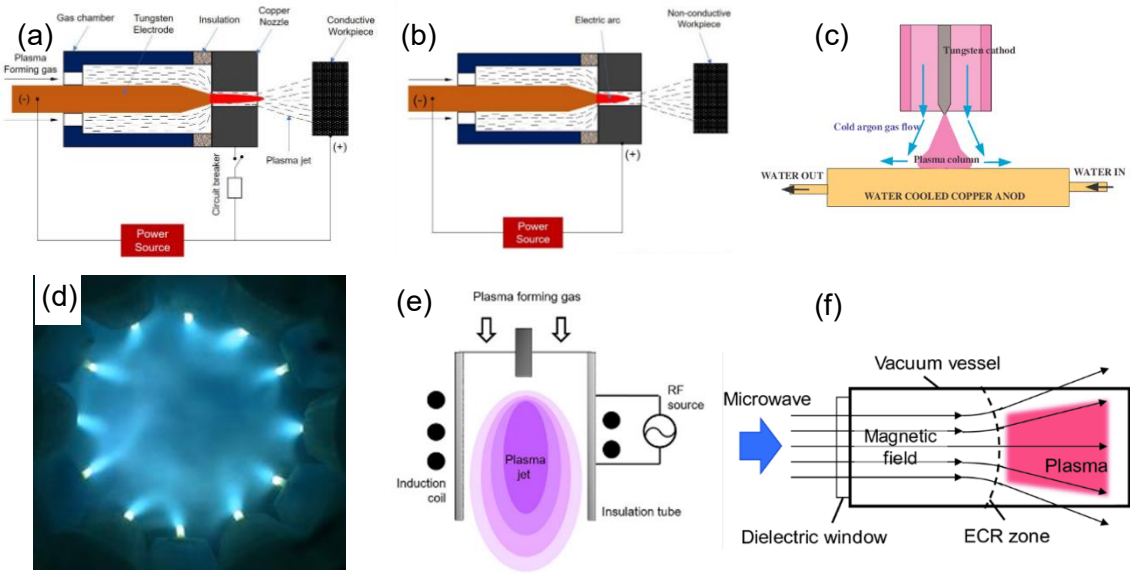

Fig. 1.3. Schematic diagrams for different generators of thermal plasma. (a) transfer DC arc, (b) non-transfer DC arc, (c) free-burning arc, (d) multiphase AC arc, (e) induction thermal plasma, (f) microwave thermal plasma [261,262].

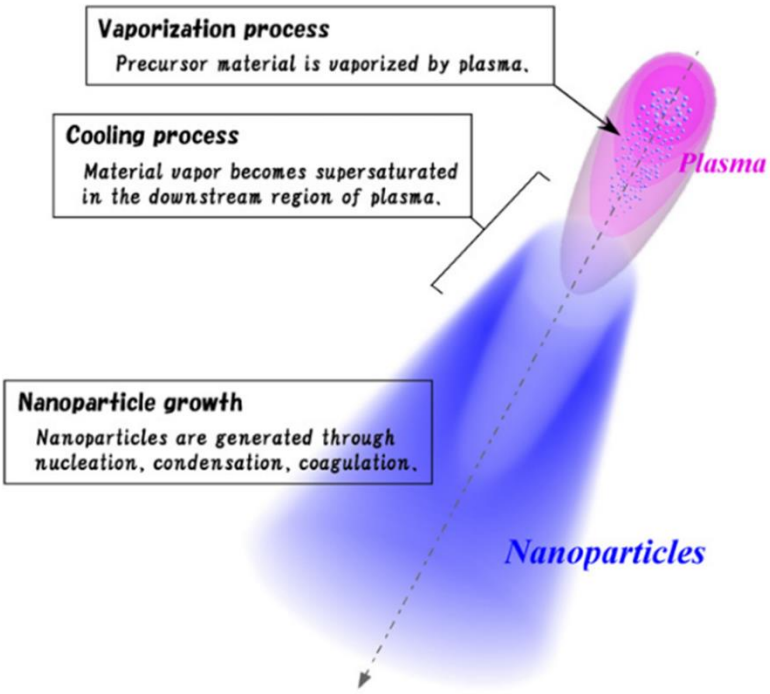

Fig. 1.4. Process of nanoparticles synthesized by thermal plasma [263].

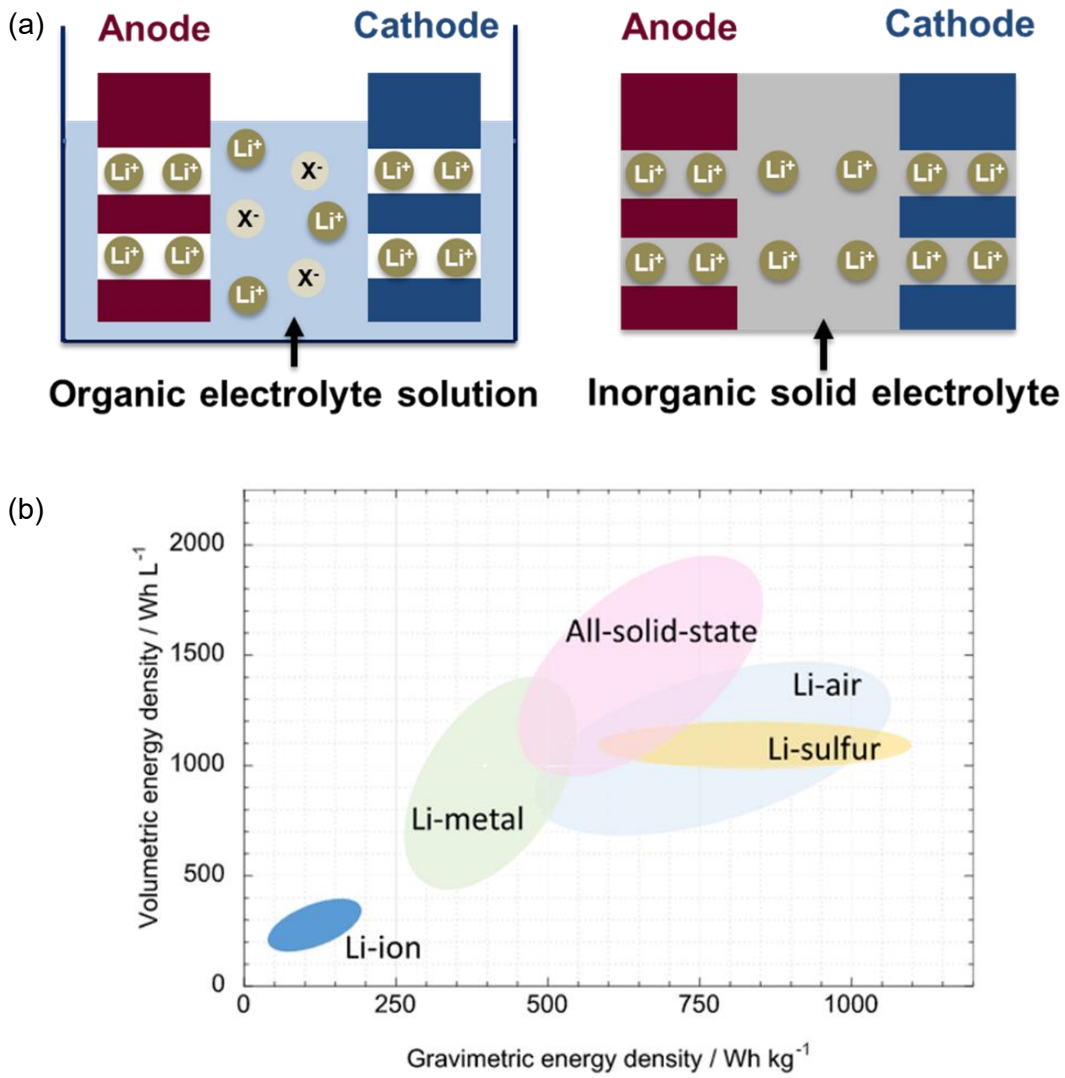

Fig. 1.5. The discrepancy between Li ion battery and all-solid-state battery. (a) schematic diagram of structure for two types of batteries, (b) volumetric and gravimetric energy density for different batteries [264].

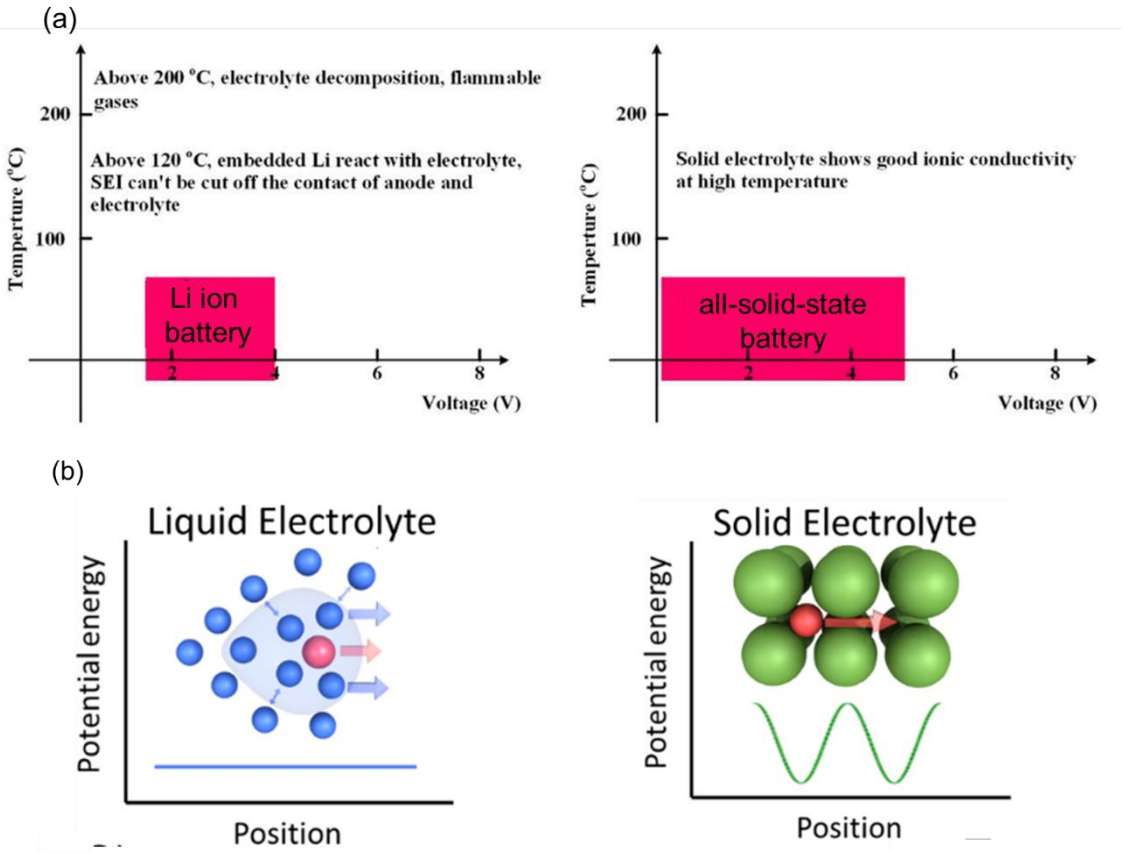

Fig. 1.6 The discrepancy for Li ion and all-solid-state battery (a) the range of safety window, (b) the potential energy.

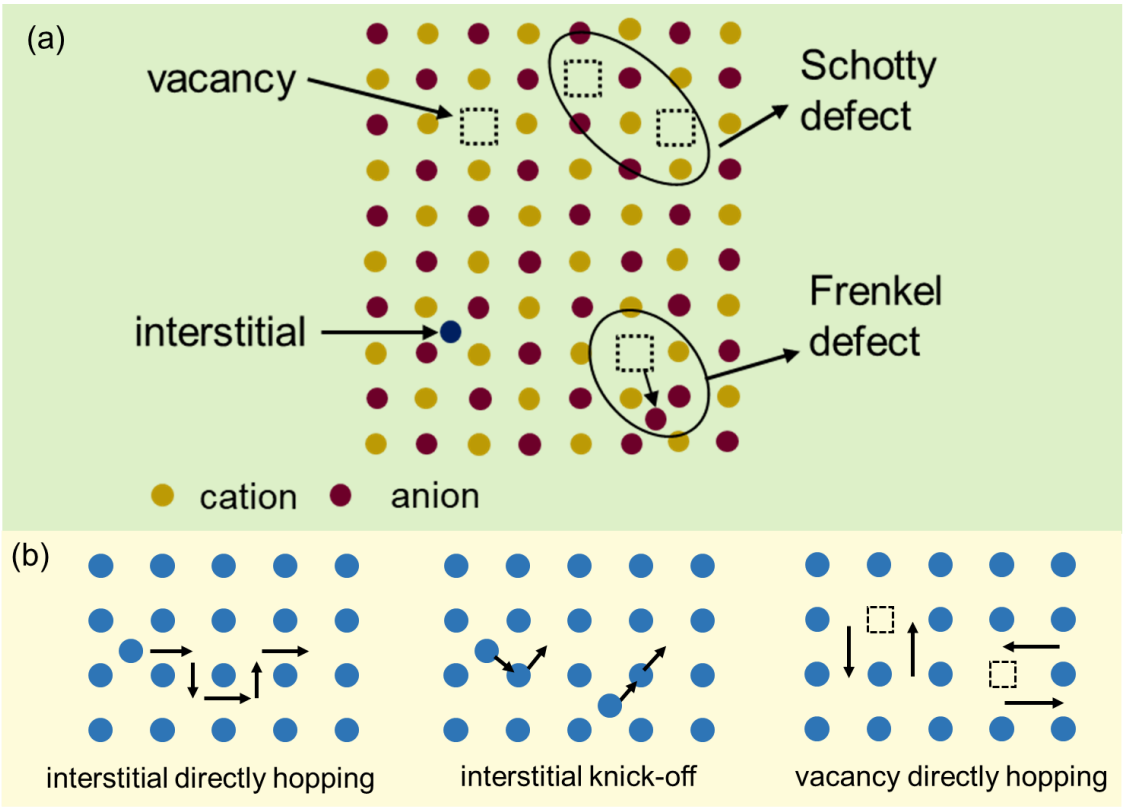

Fig. 1.7. Schematic diagram of (a) structure defects and (b) ion migration mechanism.

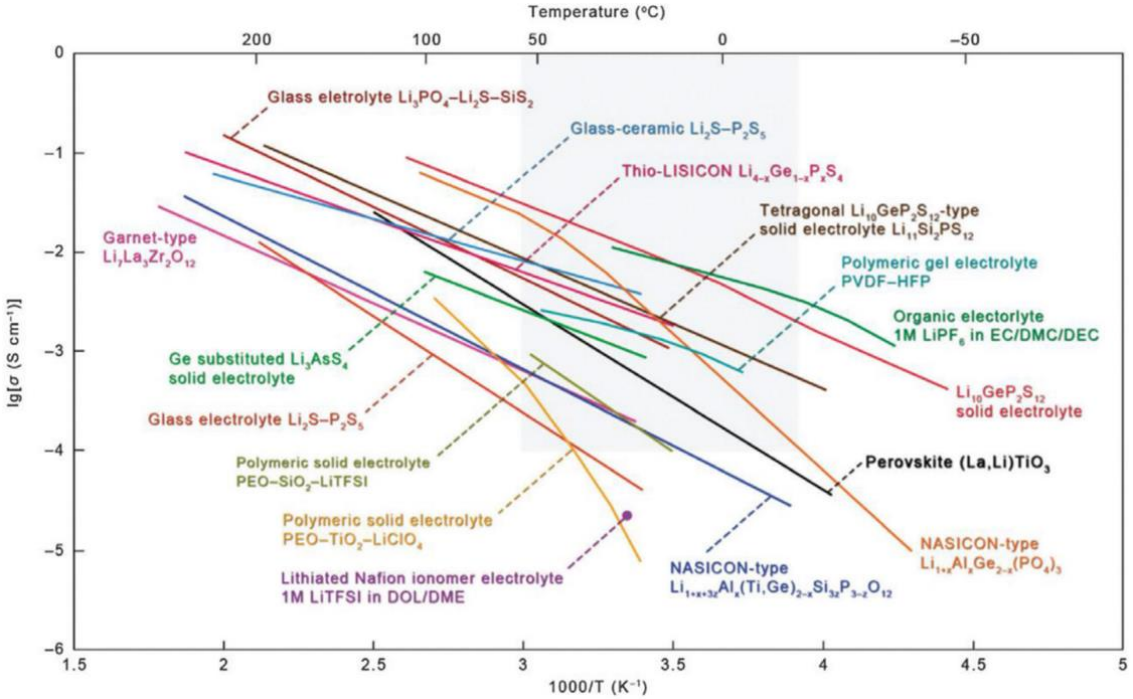

Fig. 1.8. Lithium ionic conductivity for different solid electrolyte materials [264].

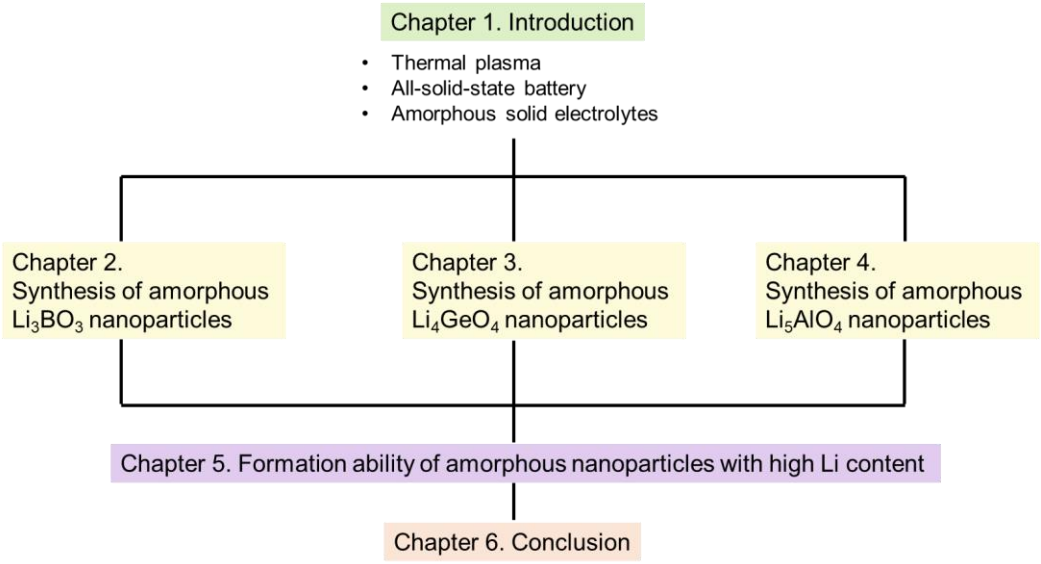

Fig. 1.9. Flow diagram of this dissertation.

2. Synthesis of Amorphous Li_3BO_3 Nanoparticles

The ASSBs attract academic attention gradually and strongly with rapid development of electric vehicles and portable devices. The unique advantages of ASSBs, such as large energy density, no leakage and non-flammable, allow them to become a promising choice for second-generation batteries [1]. The solid-state battery materials of ASSBs promise a higher lithium transport number and wider electrochemical window, however, also result in lower lithium ion conductivity and stronger interfacial resistance between electrolyte and electrode, contrasted to conventional lithium ion batteries [2]. The investigation of solid electrolyte materials has been a hot issue in order to address the above problems.

Amorphous Li_3BO_3 nanoparticles are considered a promising candidate for solid electrolytes ascribing to their outstanding advantages. The chemical and electrochemical stability of oxide avoids electrolyte decomposition and harmful gas generation during cycling. Amorphous structure increases the formability, simultaneously, the sufficient defects of amorphous benefit Li ion mobility. The interface area between electrode and electrolyte can be enhanced by the nanosized particles, which decrease the interfacial resistance. The high Li content in Li_3BO_3 promises the high ion conductivity, as well as, the good glass former boron allows easy formation of amorphous nanoparticles.

The conventional synthesis methods of amorphous nanoparticles, such as mechanical milling and sol-gel method, are time-consuming and operation-complex. Advanced and efficient synthesis methods should be developed as soon as possible. Induction thermal plasma is considered an ideal method to generate nanoparticles with high purity due to its distinctive advantages, such as extremely high temperature up to 10^4 K, rapid quenching rate (10^3-10^6 K/s) and controllable atmosphere (oxide, reduction, or inert). Besides, the electrodeless discharge,

large plasma volume, and low gas velocity also ensure its superiority in nanoparticle synthesis [3,4]. Especially the rapid quenching rate is suitable for amorphous structure nanoparticle formation. Moreover, the nanoparticles can be synthesized in a very short time.

Therefore, this chapter focuses on synthesizing amorphous Li_3BO_3 nanoparticles by induction thermal plasma with different experiment conditions. The effect of O_2 flow rate, additional quenching gas and formation mechanism were investigated based on experiment results and thermodynamic analysis.

2.1 Experimental

2.1.1 Experimental Configuration and Procedure

Figure 2.1 shows a schematic illustration of experimental device for amorphous Li_3BO_3 nanoparticles synthesis. The setup mainly consists of power supply, powder feeder, plasma touch, reaction chamber, quench tube, and prepared particles collection filter. The thermal plasma was generated with 4 MHz applied electromagnetic field, and the input power fixed at 20 kW. Sheath gas was set at 60 L/min with different Ar (purity > 99.99%, Fukuoka Oxygen Cooperation) and O_2 (purity > 99.5%, Fukuoka Oxygen Cooperation) ratios. Argon was selected as quenching gas and was injected into chamber by quench tube which was placed 15 cm below touch. Oxygen offers oxidizing atmosphere for Li oxidation during plasma process. The injection of counter quenching gas offers rapid quenching rate. Other experiment conditions are listed in **Table 2.1**.

Crystal α-Li_3BO_3 was selected as raw material (diameter 10-30 μm purity 99.9%, Toyoshima manufacturing.) was injected into reaction chamber through Ar at 600 mg/min. The raw material would be evaporated immediately in high temperature region after injecting into plasma, then the particles would nucleate in relative lower temperature region under supersaturated state. The product nanoparticle would be collected from the wall of chamber and filter after co-condensation,

coagulation. Oxygen was injected into chamber gradually after plasma process in order to ensure all lithium exists as compounds to prevent simple substance Li existence.

2.1.2 Analysis Method

The phase and crystal structure identification of prepared particles were achieved by X-ray diffraction (XRD, Rigaku Multifle), operating with a Cu Kα source (λ = 0.1541 nm). The continue scan was conducted in a 2θ range of 10°-90° at a scan speed of 1°/min. The borate structure and their relative amounts were understood by a microscopic laser Raman spectrometer (Raman, LabRAM ARAMIS). The wavelength of laser source in this research was 532 nm. The morphology of prepared particles was characterized through transmission electron microscopy (TEM, JEOL JEM-2100HCKM). The surface component of product was determined by X-ray photoelectron spectroscopy (XPS, Shimadzu KRATOS AXIS ULTRA) to check by product.

2.2. Experiment Results

2.2.1 Effect of Oxygen Flow Rate

The morphology of products synthesized by different O_2 flow rates was understood through TEM. The TEM photographs with electron diffraction are shown in **Fig. 2.2 (a)-(d)**. The TEM was operated at an acceleration voltage of 200 kV. A 16 mega pixel CMOS camera is used to capture digital TEM photographs. The diameter of the area of the electron diffraction is 200 nm. The spherical particles are only observed in O_2 1L/min condition, the agglomerates are observed in other conditions. The spherical particles would be produced at high temperature because of coalescence. The loose agglomerates with quite open structure would be formed at lower temperature. Those partially sintered particles form into non-spherical state at intermediate condition [5]. Induction thermal plasma is characterized rapid quenching rate. Generation of the

lithium borate would be started in relative lower temperature region around 1700 K. Coalescence of lithium borate particles is negligibly slow, the agglomerates would form in this research. **Figure 2.2 (e)-(f)** is the enlarged TEM photograph of nanoparticles synthesized 2.5 L/min and 5 L/min O_2. The photographs indicate that the diameter of nanoparticles is around 30-50 nm indexed by red circle. Some particles indexed by orange circle have a diameter below 10 nm.

Figure 2.3 (a) shows the XRD spectra for products synthesized by different O_2 flow rates. Peaks of major product belong to high temperature phase Li_3BO_3 (β-Li_3BO_3) in all cases [6,7], the peaks of Li_2CO_3 are also detected as the by-products. The β-Li_3BO_3 is not stable at room temperature, and it would transit to thermodynamically stable phase (α-Li_3BO_3) around 977 K [8]. This structure could be remained owing to the rapid quenching rate in thermal plasma. The intensity of β-Li_3BO_3 peaks becomes weak with O_2 flow rate increase.

The estimated amorphous degree of product with different O_2 flow rates is shown in **Fig. 2.4**. The amorphous degree was estimated by *JADE* 6.5 (Material Data, USA) based on XRD spectra using the following equations:

$$W_{Amorphous} = 1 - DOC \tag{2.1}$$

$$DOC = \frac{I_c}{I_t} \tag{2.2}$$

where DOC represents degree of crystalline, I_c and I_t are crystalline integral intensity and total integral intensity, respectively. There is an obvious growth in amorphous degree with O_2 flow rate increase from 1 L/min to 2.5 L/min to 5 L/min, the corresponding estimated amorphous degree are 54%, 59%, and 70%. Increased amorphous degree is caused by the different composition and structure of different products. The reason for difference among products in composition and structure would be discussed in next section.

The Raman analysis was conducted to understand amorphous part composition. **Figure 2.5 (a)** is the Raman spectra for products synthesized by different O_2 flow rates. The wavelength of laser

was fixed at 532 nm. Gray dots line is the experimental spectrum, the blue line is the cumulative fitting. The characteristic peaks are fitted by Gaussian function and four typical peaks are identified. The peaks located around 760-785 cm^{-1}, 850-830 cm^{-1}, and 950-930 cm^{-1} are indexed to borate units [9]. These three regions are indexed to diborate ($B_4O_9^{6-}$) in red dotted line, pryoborate ($B_2O_5^{4-}$) in orange and orthoborate (BO_3^{3-}) in purple, respectively. The peak around 1100 cm^{-1} is classified as CO_3^{2-} in green [10]. Besides target material Li_3BO_3 other lithium borates $Li_6B_4O_9$ and $Li_4B_2O_5$ were also synthesized during the plasma process according to Raman spectra. The $Li_4B_2O_5$ is not stable at room temperature, and it decomposes into $Li_6B_4O_9$ and Li_3BO_3 below 923 K [11]. The $Li_4B_2O_5$ could be remained ascribing to the rapid quenching rate.

The relative molar amount of each structure group was estimated in order to obtain the relative amount of target material. The relative amount of a particular structure group can be estimated assuming that the total number of Raman scattering events gives rise to the area under the peak [12]. In addition, the integral intensity of each Raman peaks is related to the molar amount of the corresponding borate structure unit. The relative molar percentage of each unit could be accessed based on above assumption [13]. **Figure 2.6** displays the evolution of the relative amount of each borate group and CO_3^{2-} in product synthesized by different O_2 flow rates. The percentage of BO_3^{3-} is dominant compared to other units in product. There is a downward trend in BO_3^{3-} percentage with O_2 flow rate increase, while the other structure group in product show an opposite trend. The $B_4O_9^{6-}$ and $B_2O_5^{4-}$ are more easily form into amorphous structure contrasted to BO_3^{3-} at same quenching rate owing to bridging oxygens (BOs) existence. Therefore, the higher amorphous degree was achieved with the O_2 flow rate increase due to more $Li_6B_4O_9$ and $Li_4B_2O_5$ generated.

Figure 2.4 shows the estimated result for amorphous Li_3BO_3 degree with different O_2 flow rates. This result was obtained based on following considerations. The Raman spectra indicate the products consisted of $Li_6B_4O_9$, $Li_4B_2O_5$, Li_3BO_3, and Li_2CO_3. Only Li_2CO_3 and β-Li_3BO_3 peaks

were detected by XRD, which means the amorphous part in product consisted of $Li_6B_4O_9$, $Li_4B_2O_5$ and part of Li_3BO_3. The relative amount of amorphous Li_3BO_3 could be estimated by subtracting the relative amount of $Li_6B_4O_9$ and $Li_4B_2O_5$ from all amorphous part. **Figure 2.4** demonstrates the percentage of amorphous structure Li_3BO_3 increases with O_2 flow rate increase. Around 33% of amorphous Li_3BO_3 was obtained in 1 L/min case. The amorphous Li_3BO_3 degree increases to 37% and 41% in 2.5 L/min and 5 L/min cases, respectively.

The by-product Li_2CO_3 was detected in final product, although no carbon source was input during plasma process. The generation of Li_2CO_3 is considered after the plasma process, that is, those unreacted Li_2O attach H_2O and CO_2 in atmosphere to form Li_2CO_3. The surface composition of product was identified by XPS in order to verify this hypothesis. **Figure 2.7 (a)-(b)** show the XPS spectra for B (1s) and C (1s) with different O_2 flow rates. The peak near 188 eV and 191 eV are assigned to carbide and B-O bond, respectively [14]. Peaks position of carbide is located near 282 eV and 284 eV as for carbon (1s) [15]. The other two peaks near 286 eV and 289 eV are classified as C-O, the two peaks identify the existence of CO_3^{2-} [15]. There is a great difference in penetration depth for Raman and XPS analysis methods [16]. The XPS can measure the kinetic energy and quantity of escape electrons from 1 nm to 10nm below the surface of the material, while the penetration depth of Raman is around 1000 nm under the analysis condition used in this research [17]. Thus, XPS and Raman focus on the surface region and whole particles, respectively.

Figure 2.8 is the estimated result for relative molar amounts of C in products based on Raman and XPS with different O_2 flow rates. The figure demonstrates that the relative molar amount of C on surface is much higher than whole particles. This huge gap reveals that the carbon in products concentrates on the surface. Surface of the product has the possibility to contact the atmosphere, further reacting with H_2O and CO_2 to form Li_2CO_3. Hence, the aforementioned hypothesis is verified, the CO_2 is the carbon source of Li_2CO_3 synthesis. The existence of Li_2CO_3 also indicates

that Li_2O is synthesized and that not all Li_2O take part in the reaction during the plasma process.

The above experiment results indicate that O_2 has a positive effect on amorphous Li_3BO_3 fabrication. Meanwhile, the O_2 injection results in more by-product generation. The by-product Li_2CO_3 concentrates on the surface of the produce. The reason would be discussed in the next section.

2.2.2 Effect of Argon Quenching Gas

There is no significant difference among products synthesized by different quenching gas flow rates in morphology. No spherical particles were observed and the products present agglomerate state. Because the quenching rate is enhanced by quenching gas. There is no sufficient energy to support the boundary of those small particles to eliminate to form a new spherical particle in low temperature region.

The major product in crystal part is also β-Li_3BO_3 in different quenching gas flow rates, the Li_2CO_3 was detected as by-product. The XRD spectra are presented in **Fig. 2.3 (b)**. The estimated amorphous degree of products is shown in **Fig. 2.9**. The result reveals that the amorphous degree increases obviously after quenching gas utilization, arriving at around 71% in 40 L/min quenching gas condition. This phenomenon is related to nanoparticle growth and the chemical composition of the product. Details would be discussed in the next section.

The products synthesized by different quenching gas flow rates also consisted of Li_3BO_3, $Li_4B_2O_5$, $Li_6B_4O_9$, and Li_2CO_3 based on Raman analysis. The Raman spectra are presented in **Fig. 2.5 (b)**. The quantified result of Raman spectra is shown in **Fig. 2.10**. There is a similar tendency in quenching gas condition with O_2 condition. The percentage of BO_3^{3-} shows a declining trend, while other borate groups and CO_3^{2-} present a rising trend with quenching gas flow rates increase. Enhanced amorphous degree of product was obtained due to more $Li_6B_4O_9$ and $Li_4B_2O_5$

generation. The amorphous Li_3BO_3 degree result is presented in **Fig. 2.9**. The result demonstrates more amorphous Li_3BO_3 was fabricated after quenching gas utilization, occupying around 42% of the final product in 40 L/min condition.

The by-product Li_2CO_3 formation mechanism has already been discussed in the previous part. The XPS results for quenching gas condition show Li_2CO_3 also concentrate on the surface of products. The Li_2CO_3 was synthesized by unreacted Li_2O with H_2O and CO_2 in atmosphere.

The above results indicate that Ar counter quenching gas influences Li_3BO_3 generation negatively. Synthesis of amorphous Li_3BO_3 is promoted by quenching gas. The reason would be discussed in the next section.

2.2.3 Effect of Oxygen Quenching Gas

Diatomic gas O_2 was selected as another quenching gas in order to investigate the effect of different types of quenching gas. **Figure 2.3 (c)** displays the XRD spectra of products synthesized by different O_2 quenching gas flow rates. A declined tendency of crystal peak intensity was observed with O_2 quenching gas flow rate increasing. Another by-product $LiOH \cdot H_2O$ was detected in 20 L/min case. There is no hydrogen source injection during the plasma process, simultaneously, not all Li_2O take part in reactions. These $LiOH \cdot H_2O$ are considered to be synthesized by unreacted Li_2O with H_2O in the atmosphere. Estimated amorphous degree of products reaches around 72% with 40 L/min O_2 flow rates, shown in **Fig. 2.11**.

The products synthesized by different O_2 quenching gas flow rates are also consisted of Li_3BO_3, $Li_4B_2O_5$, $Li_6B_4O_9$, and Li_2CO_3 based on Raman analysis, the Raman spectra are shown in **Fig. 2.5 (c)**. The quantified results of Raman spectra are shown in **Fig. 2.12**, this result demonstrates composition variety tendency of products synthesized by different O_2 quenching gas flow rates is similar to Ar quenching gas. The percentage of BO_3^{3-} decrease from 53% to 43% with O_2

increasing to 40 L/min. Amorphous Li_3BO_3 degree is presented in **Fig. 2.11**, showing around 43% amorphous Li_3BO_3 nanoparticles are obtained with 40 L/min O_2 quenching gas injection.

The above results indicate that quenching gas type cannot affect the synthesized compounds and amorphous degree in Li-B-O system. Because the temperature of injected O_2 is similar to injected Ar, both of them are close to room temperature. The thermal conductivity of Ar and O_2 at room temperature is similar, which leads to no obvious discrepancy in the temperature distribution. Thus, there are no comparable experiment results in different types of quenching gas cases.

2.3. Discussion

2.3.1 Formation Mechanism of Lithium Borate Nanoparticles

There is a huge difference between induction thermal plasma and other conventional methods in amorphous nanoparticle fabrication regarding the formation mechanism. The lithium borate nanoparticles formation mechanism was investigated. This investigation attributes to understanding the effect of O_2 and quenching gas on product in composition and structure theoretically. The formation mechanism of nanoparticles in induction thermal plasma has already been investigated systematically [18–20]. The raw materials evaporate totally in high temperature region after injecting into plasma immediately, then particles nucleate in super saturated state in lower temperature downstream region, finally particles generation after condensation [20]. The reactions are ended by the solidification of each species in Li-B-O system. Particles grow continually through coagulation once occur in vapor phase. Therefore, the nucleation phase should identify first in the Li-B-O system. Because the solid interface is absent during the nucleation for thermal plasma synthesis. Homogeneous nucleation rate J is estimated based on non-dimensional surface tension in this paper and expressed as [21]:

$$J = \frac{\beta_{ij} n_s^2 S}{12} \sqrt{\frac{\Theta}{2\pi}} \exp\left[\Theta - \frac{4\Theta^3}{27(\ln S)^2}\right] \tag{2.3}$$

where S is saturation ratio, n_s is equilibrium saturation monomer concentration at temperature T. The saturation ratio is given by the following equation:

$$S = \frac{P}{P_S} \tag{2.4}$$

where P and P_s represents partial pressure of vapor and saturation pressure, respectively. The non-dimensional surface tension Θ is given by:

$$\Theta = \frac{\sigma s_1}{kT} \tag{2.5}$$

where δ is the surface tension, s_1 is the monomer surface area, k means Boltzmann constant. β_{ij} is the collision frequency function between monomers and expressed as:

$$\beta_{ij} = \left(\frac{3v_1}{4\pi}\right)^{1/6} \sqrt{\frac{6kT}{\rho_P}\left(\frac{1}{i} + \frac{1}{j}\right)} \times \left(i^{1/3} + j^{1/3}\right)^2 \tag{2.6}$$

here, ρ_p means particles mass density and v_1 means monomer volume, i and j are equal to 1 because of the monomer collision mode of this method.

The particle formation could be experimental observation conveniently when the nucleate rate is over 1 cm^{-3} s^{-1} [43]. The value of the corresponding saturation ratio is defined as the critical saturation ratio at nucleation temperature. The parameters of nucleation rate are the functions of temperature according to the above equations. Thereby, nucleation temperature is considered as the temperature at which the nucleation rate achieves 1 cm^{-3} s^{-1}. The nucleation temperature for B and Li estimated based on **Eqs. (2.3)-(2.6)** are 2998 K and 1056 K with 600 mg/min feeding rate, respectively. Melting points of oxides are regarded as nucleation temperature due to the two temperatures being always close and lacking physical properties. The relationship between nucleation temperature and melting point is presented in **Fig. 2.13**. **Figure 2.13** indicates that

boron has the highest nucleation temperature and should nucleate first in this system. The melting point and boiling point in **Fig. 2.13** are obtained from Lang's Handbook of Chemistry [22].

The homogenous nucleation is also dependent on saturation ratio strongly beside the nucleation temperature. The vapor phase reactions among substances before nucleation would influence their vapor pressure to a great extent. Since thermal plasma is considered as thermodynamic equilibrium, the vapor phase reactions are chemical equilibrium. Thermal equilibrium composition in Li-B-O system is developed using thermodynamic calculation software *FactSage* 7.2 (Centre for Research in Computational Thermochemistry, Canada; GTT-Technology, Germany) with following conditions. The feeding rate of crystalline Li_3BO_3 is 600 mg/min, O_2 flow rate is 2.5 L/min. Since the nuclei cannot stably exist in high temperature region, the nucleation and condensation phase are solidified below 1000 K. The thermodynamic equilibrium composition is estimated with a temperature range of 1000-5000 K. The estimated result is shown in **Fig. 2.14**. The result reveals that O, Li, and BO vapor are dominant over 3000 K. The amount of B vapor is much lower around its nucleation temperature, which means insufficient B vapor pressure cannot lead to super saturation state. Thus, boron cannot nucleate first in Li-B-O system. The amount of O, Li and BO vapor lose their advantage gradually with temperature declining. Vapor of Li_2O and Li_2O_2 begin to rise, vapor of $LiBO_2$ becomes the stable phase in this system. The main reactions during this process are presented following:

$$B(g) + O(g) \rightarrow BO(g)$$

$$Li(g) + O(g) \rightarrow LiO(g)$$

$$BO(g) + LiO(g) \rightarrow LiBO_2(g)$$

$$LiO(g) + Li(g) \rightarrow Li_2O(g)$$

Figure 2.13 indicates that Li_2O would nucleate around 1711 K following B. The vapor pressure of Li_2O vapor is sufficient according to thermodynamic analysis. Hence, Li_2O would nucleate

first in Li-B-O system. The Li_2O and $LiBO_2$ are the co-condensation phase.

The formation mechanism is put forward according to thermodynamic consideration. **Figure 2.15** presents the amorphous Li-B-O nanoparticles generation process. Crystalline Li_3BO_3 decomposes and evaporates into Li, B, and O vapor after injecting into thermal plasma in high temperature region. The vapor-phase reactions start among various substances to generate Li_2O vapor and $LiBO_2$ vapor. More and more Li_2O molecules are generated continuously to produce embryos. Simultaneously, the saturation vapor pressure decreases rapidly due to temperature decline. Homogeneous nucleation of Li_2O would start under super saturation state when temperature declines to 1711 K. Vapor of $LiBO_2$ and Li_2O heterogeneous co-condense on the Li_2O nucleus to form Li-B-O system particles subsequently. The driving force for heterogeneous condensation is saturation ratio *S*. Vapor of Li_2O achieves the supersaturated state earlier than vapor of $LiBO_2$, the Li_2O condensation would be dominant in initial stage [23]. The Li-rich nanoparticles of Li_3BO_3 are formed mainly at the early stage of particle growth. Another condensation phase $LiBO_2$ achieves super saturation state with temperature decrease. Vapor of Li_2O is consumed simultaneously. The B-rich particles of $Li_6B_4O_9$ and $Li_4B_2O_5$ would be formed in following stage.

There is an intense relationship between the structure of borate group and Li^+ content. **Figure 2.16** illustrates the process for borate group transformation with Li^+ increase. The borate structure transforms from six-member with one BO_4 tetrahedron (BO^{2-}) to diborate ($B_4O_9^{6-}$) to pyroborate ($B_2O_5^{4-}$) to orthoborate (BO_3^{3-}) in order with Li^+ content increase [13]. The structure of BO_2^- starts to change when $LiBO_2$ and Li_2O vapor condense on Li_2O nuclei during the heterogeneous co-condensation process. The bridge oxygens (BOs) bonds start to break because the stronger electropositive of Li contrasted to B. The non-bridge oxygens (NBOs) start to generate. Vapor of Li_2O more rapidly condenses on the nucleus than $LiBO_2$ vapor at the early stage, the Li_3BO_3 is

synthesized by complete borate transition. This transition is impaired in the following stage because less Li_2O vapor takes part in the transition process. Hence, Li_3BO_3 was mainly synthesized at early stage due to the complete borate group transition. The $Li_6B_4O_9$ and $Li_4B_2O_5$ were mainly synthesized at following stage due to uncomplete transition caused by low Li_2O partial pressure.

The borate transition terminates by species solidification in the Li-B-O system. Every species of the Li-B-O system solidifies below 1000 K based on **Fig. 2.14** and phase diagram [11]. These synthesized particles grow continuously by coagulation in lower temperature region to form loose agglomerates. The temperature during coagulation process is not enough to provide sufficient energy to activate the surface of synthesized particles. Spherical particles cannot be formed by incomplete coalescence [24].

Borate transition is related to temperature distribution intensively because the process would be ended by solidification of species. Since diatomic O_2 releases heat through decomposition and ionization, while monoatomic gas Ar release heat only through ionization. The thermal conductivity of the Ar and O_2 mixture would be increased by adding diatomic gas O_2 into sheath gas. Therefore, addition of O_2 not only leads to improving heat transfer from plasma to particles but also shrinks the plasma flow [25,26]. Enhanced quenching rate in reactor chamber would achieve by the shrunken plasma flow. Since the counter-flow quenching gas suppresses high temperature region, the more rapid quenching rate is also achieved. The quenching rate would increase from 3.2×10^4 K/s without quenching gas to 1.3×10^5 K/s and 4.0×10^5 K/s after 20 L/min and 40 L/min quenching gas injection, respectively [27]. Hence, addition of O_2 into sheath gas and counter-flow quenching gas utilization could achieve steeper temperature gradient. The steeper temperature gradient accelerates temperature decrease and shortens co-condensation time. Solidification of species in the Li-B-O system is also promoted, the borate structure

transformation also would be impeded. More $B_4O_9^{6-}$ remained in final product due to no sufficient transformation time. In addition, the more rapid quenching rate prevents $B_2O_5^{4-}$ decomposes into $B_4O_9^{6-}$ and BO_3^{3-}. This situation also reduces Li_3BO_3 amount. Therefore, less Li_3BO_3 was obtained in higher O_2 and quenching gas conditions. Increase of unreacted Li_2O leads to more Li_2CO_3 generation after plasma process.

2.3.2 Formation Mechanism of Amorphous Li_3BO_3

Nanoparticles synthesis by induction thermal plasma is an extremely fast and complex heat/mass transfer process. The whole process, containing phase conversion, interaction among thermofluid field, induced electromagnetic field, particles concentration field with numerous variables as well as chemical reactions, lasts only a few tens of milliseconds [28,29]. Therefore, nanoparticle formation and crystallization are considered to occur simultaneously during the process.

Figures 2.4 and **2.9** demonstrate the percentage of amorphous structure Li_3BO_3 increases with O_2 and Ar quenching gas flow rate increase. There is a significant influence of nanoparticle growth on temperature distribution. Because the critical indices during this process, such as morphology and structure of product, are influenced by temperature. Saturation ratio, *S*, is the driving force for nucleation based on **Eq. (2.3)**, the higher-level saturation ratio would lead to faster nucleation., Nucleation rate would be enhanced when *P* is fixed while P_s becomes lower. P_s is a function of temperature and the value would be lower when temperature decrease. The number of nuclei is increased at the more rapid quenching rate. Because the total amount of Li_2O vapor is constant, the vapor consumption of each nucleus would reduce with increased number of nuclei. This situation allows smaller particles to generate. The particle order growth time is also reduced owing to steeper temperature gradient. Moreover, particle growth is also impaired by the lower kinetic

energy. The lower temperature results in the lower kinetic energy of particles, which would further impair co-condensation and coagulation. Those small particles cannot achieve long-range order structure, and the product keeps the more chaotic state. Therefore, increased amount of amorphous Li_3BO_3 particles were obtained with steeper temperature gradient.

2.4. Conclusion

Amorphous Li_3BO_3 as solid electrolyte was synthesized successfully by induction thermal plasma with different O_2 flow rates and counter Ar quenching gas injection. The formation mechanism was investigated based on nucleation temperature and thermodynamic analysis. Enhanced quenching rate could reduce co-condensation duration time, further influence borate group transition negatively, and finally Li_3BO_3 percentage is decreased. More $Li_6B_4O_9$ and $Li_4B_2O_5$ are generated as amorphous structure, which enhances products amorphous degree. The enhanced quenching rate allows smaller size nuclei generation and prevents particles grow orderly. This phenomenon leads to more amorphous Li_3BO_3 production. In addition, the insufficient temperature caused by rapid quenching rate results in the product with agglomerated state.

Reference:

[1] K. Takada, Progress and prospective of solid-state lithium batteries, Acta Mater. 61 (2013) 759–770. https://doi.org/10.1016/j.actamat.2012.10.034.

[2] M. Tatsumisago, R. Takano, K. Tadanaga, A. Hayashi, Preparation of Li_3BO_3-Li_2SO_4 glass-ceramic electrolytes for all-oxide lithium batteries, J Power Sources. 270 (2014) 603–607. https://doi.org/10.1016/j.jpowsour.2014.07.061.

[3] M. Tanaka, T. Kageyama, H. Sone, S. Yoshida, D. Okamoto, T. Watanabe, Synthesis of Lithium Metal Oxide Nanoparticles by Induction Thermal Plasmas, Nanomaterials. 6 (2016) 60. https://doi.org/10.3390/nano6040060.

[4] K. Major, J. Veilleux, G. Brisard, Lithium Iron Phosphate Powders and Coatings Obtained by Means of Inductively Coupled Thermal Plasma, Journal of Thermal Spray Technology. 25 (2016) 357–364. https://doi.org/10.1007/s11666-015-0289-0.

[5] S. Samal, Synthesis of TiO_2 Nanoparticles from Ilmenite Through the Mechanism of Vapor-Phase Reaction Process by Thermal Plasma Technology, J Mater Eng Perform. 27 (2018) 2622–2628. https://doi.org/10.1007/s11665-017-3060-5.

[6] H.W. Hans-Albert Lehmann, Zur Chemie und Konstitution borsaurer Salze. V. Zur Isomorphie zwischen Carbonaten und Boraten., Journal of Inorganic and General Chemistry. 304 (1960) 121–125.

[7] M. He, H. Okudera, J. Fleig, A. Simon, X.L. Chen, J. Maier, The Al^{3+} stabilized phase $Li_{3-3x}Al_xBO_3$, J Solid State Chem. 178 (2005) 680–687. https://doi.org/10.1016/j.jssc.2004.12.017.

[8] Y.P.X. L. Wu, X.L. Chen, Q.Y. Tu, M. He, Y. Zhang, Phase Relations in the System Li_2O–CaO–B_2O_3, Journal of the Alloys and Compounds. 385 (2003) 23–28. https://doi.org/10.1111/j.1151-2916.1969.tb09198.x.

[9] W.L. Konijnendijk, J.M. Stevels, The structure of borate glasses studied by Raman scattering, J Non-Cryst Solids. 18 (1975) 307–331. https://doi.org/10.1016/0022-3093(75)90137-4.

[10] D.E. Irish, Raman and Infrared Spectral Studies of Anhydrous Li_2CO_3 and Na_2CO_3, Advances in Infrared and Raman Spectroscopy. 4788 (1976).

[11] B.S.R. Sastry, F.A. Hummel, Studies in Lithium Oxide Systems: V, Li_2O B_2O_3–B_2O_3, Journal of the American Ceramic Society. 41 (1958) 216–218. https://doi.org/10.1111/j.1151-2916.1958.tb13496.x.

[12] P. Unifantowicz, S. Vaucher, M. Lewandowska, K.J. Kurzydłowski, Structural changes of silicon upon high-energy milling investigated by Raman spectroscopy, Journal of Physics Condensed Matter. 20 (2008). https://doi.org/10.1088/0953-8984/20/02/025205.

[13] M. Tatsumisago, M. Takahashi, T. Minami, M. Tanaka, N. Umesaki, N. Iwamoto, Structural Investigation of Rapidly Quenched Li_2O-B_2O_3 Glasses by Raman Spectroscopy, Yogyo Kyokai Shi/Journal of the Ceramic Society of Japan. 94 (1986) 464–469. https://doi.org/10.2109/jcersj1950.94.1089_464.

[14] T.S. Kim, J.H. Yeo, K.B. Nam, M.J. Kim, J.B. Yoo, Boron carbide coating to improve the chemical stability of nm-thick graphite films, Thin Solid Films. 704 (2020) 138002. https://doi.org/10.1016/j.tsf.2020.138002.

[15] X. Chen, X. Wang, D. Fang, A review on C1s XPS-spectra for some kinds of carbon materials, Fullerenes Nanotubes and Carbon Nanostructures. 0 (2020) 1–11. https://doi.org/10.1080/1536383X.2020.1794851.

[16] E. Buixaderas, E. Maria Anghel, S. Petrescu, P. Osiceanu, Structural investigation in the TiB_2–($Na_2O{\cdot}B_2O_3{\cdot}Al_2O_3$) system, J Solid State Chem. 183 (2010) 2227–2235. https://doi.org/10.1016/J.JSSC.2010.07.023.

[17] N. Ollier, B. Boizot, B. Reynard, D. Ghaleb, G. Petite, Analysis of molecular oxygen formation in irradiated glasses: a Raman depth profile study, Journal of Nuclear Materials. 340 (2005) 209–213. https://doi.org/10.1016/J.JNUCMAT.2004.11.011.

[18] M. Shigeta, T. Watanabe, Growth model of binary alloy nanopowders for thermal plasma synthesis, J Appl Phys. 108 (2010). https://doi.org/10.1063/1.3464228.

[19] K.S. Kim, A. Moradian, J. Mostaghimi, Y. Alinejad, A. Shahverdi, B. Simard, G. Soucy, Synthesis of single-walled carbon nanotubes by induction thermal plasma, Nano Res. 2 (2009) 800–817. https://doi.org/10.1007/s12274-009-9085-9.

[20] M. Shigeta, T. Watanabe, Two-dimensional analysis of nanoparticle formation in induction thermal plasmas with counterflow cooling, Thin Solid Films. 516 (2008) 4415–4422. https://doi.org/10.1016/j.tsf.2007.10.022.

[21] S.L. Girshick, C.P. Chiu, Kinetic nucleation theory: A new expression for the rate of homogeneous nucleation from an ideal supersaturated vapor, J Chem Phys. 93 (1990) 1273–1277. https://doi.org/10.1063/1.459191.

[22] James G. Speight, Lang's Handbook of Chemistry, Seventeenth, 2017.

[23] M. Shigeta, T. Watanabe, Effect of saturation pressure difference on metal-silicide nanopowder formation in thermal plasma fabrication, Nanomaterials. 6 (2016). https://doi.org/10.3390/nano6030043.

[24] M.T. Swihart, Vapor-phase synthesis of nanoparticles, Curr Opin Colloid Interface Sci. 8 (2003) 127–133. https://doi.org/10.1016/S1359-0294(03)00007-4.

[25] Y.L. Li, T. Ishigaki, Controlled one-step synthesis of nanocrystalline anatase and rutile TiO_2 powders by in-flight thermal plasma oxidation, Journal of Physical Chemistry B. 108 (2004) 15536–15542. https://doi.org/10.1021/jp040316j.

[26] N. Atsuchi, M. Shigeta, T. Watanabe, Modeling of non-equilibrium argon-oxygen induction plasmas under atmospheric pressure, Int J Heat Mass Transf. 49 (2006) 1073–1082. https://doi.org/10.1016/j.ijheatmasstransfer.2005.07.052.

[27] X. Zhang, Z. Liu, M. Tanaka, T. Watanabe, Formation mechanism of amorphous silicon nanoparticles with additional counter-flow quenching gas by induction thermal plasma, Chem Eng Sci. 230 (2021) 116217. https://doi.org/10.1016/j.ces.2020.116217.

[28] M. Shigeta, T. Watanabe, Numerical investigation of cooling effect on platinum nanoparticle formation in inductively coupled thermal plasmas, J Appl Phys. 103 (2008). https://doi.org/10.1063/1.2903918.

[29] M. Shigeta, T. Watanabe, Effect of saturation pressure difference on metal-silicide nanopowder formation in thermal plasma fabrication, Nanomaterials. 6 (2016). https://doi.org/10.3390/nano6030043.

Table 2.1. Experimental conditions for induction thermal plasma system.

Parameter	Condition
Input power [kW]	20
Pressure [kPa]	101.3
Frequency [MHz]	4
Sheath gas rate [L/min]	60 (Ar+O_2)
Inner gas rate [L/min]	5 (Ar)
Carrier gas rate [L/min]	3 (Ar)
Quenching gas rate [L/min]	0, 20, 40 (Ar) 0, 20, 40 (O_2)
Feed rate [mg/min]	600
Ar/O_2 molar ratio [-]	59:1,57.5:2.5, 55:5

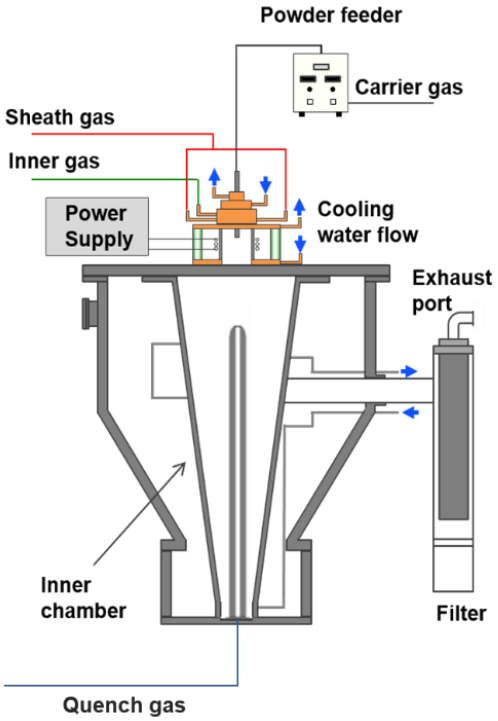

Fig. 2.1. Schematic diagram of amorphous Li_3BO_3 synthesized by induction thermal plasma.

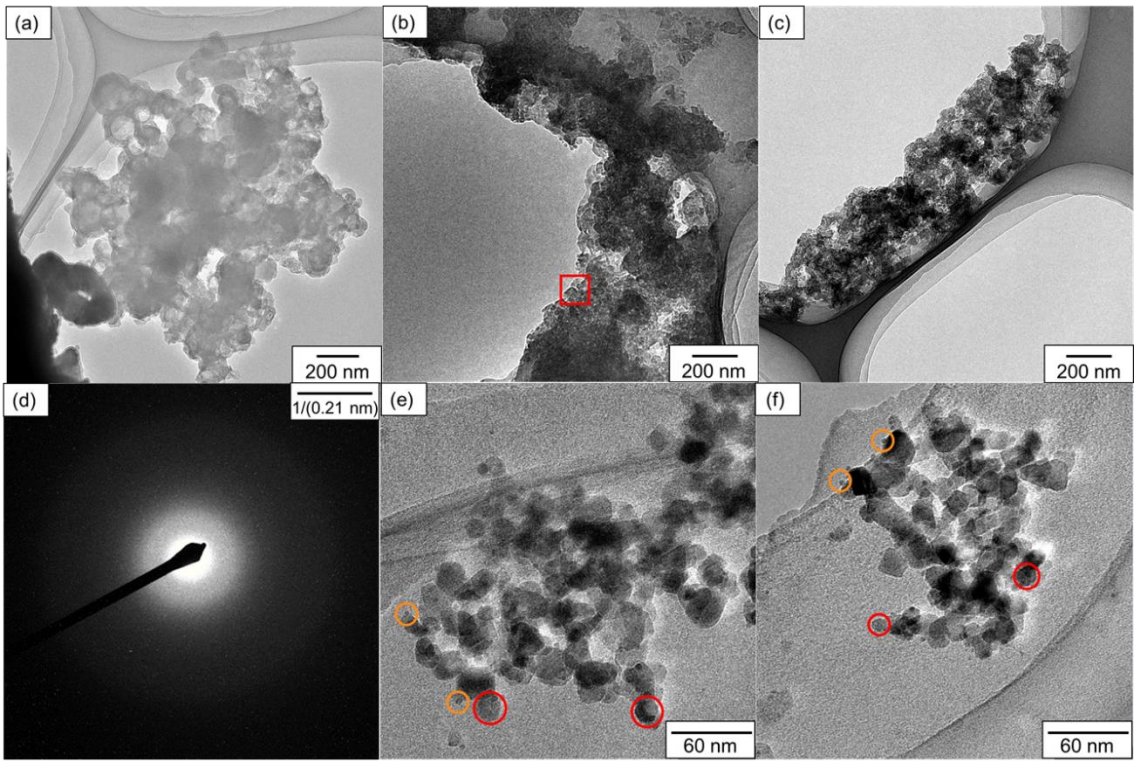

Fig. 2.2. TEM photographs of products synthesized by (a) 1 L/min O_2, (b) 2.5 L/min O_2, (c) 5 L/min O_2. The red square is the focus of the electron beam on product. The corresponding diffraction pattern is shown in (d). The enlarged TEM photograph of nanoparticles synthesized (e) 2.5 L/min and (f) 5 L/min O_2.

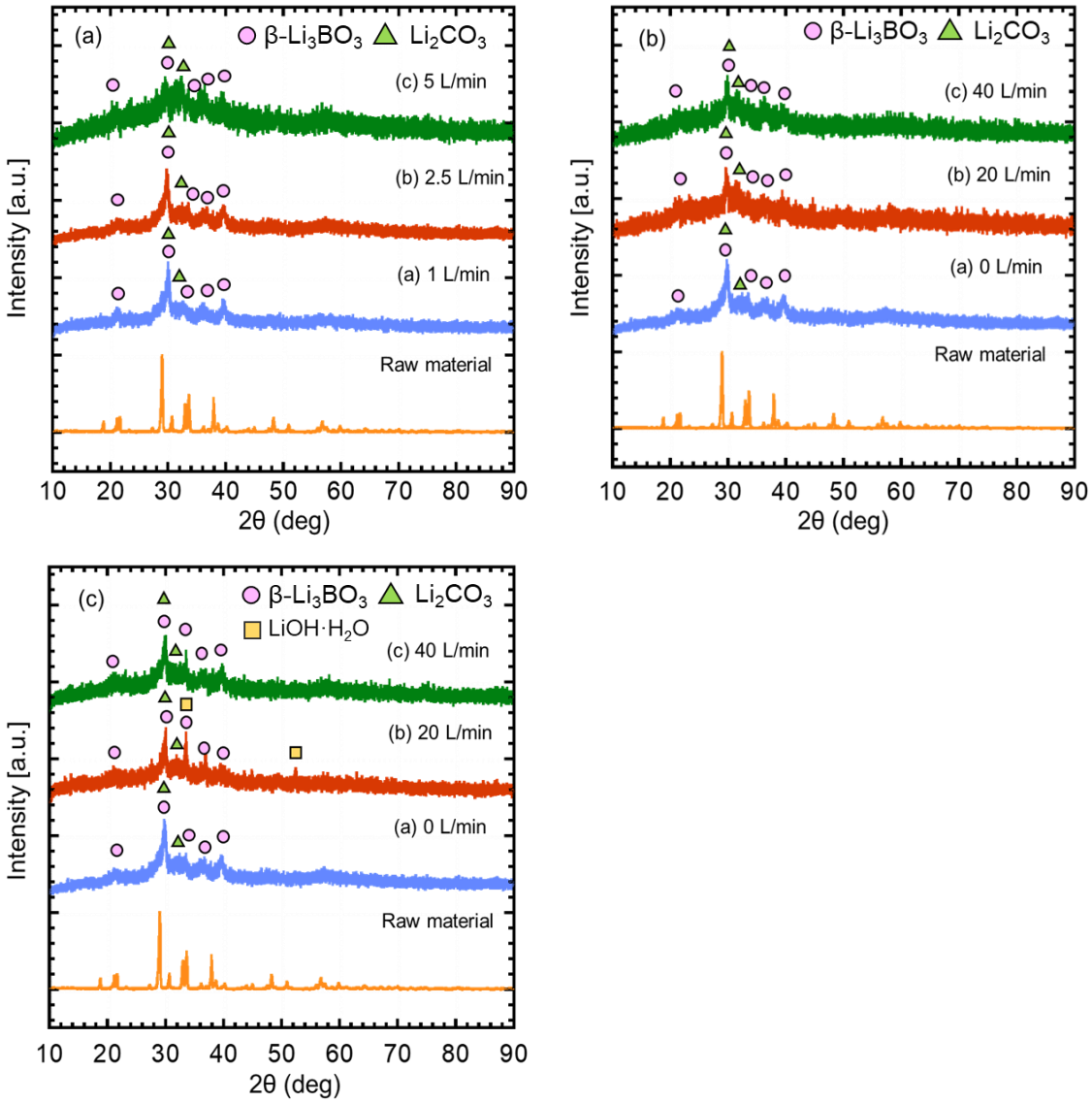

Fig. 2.3. XRD spectra of products synthesized by different (a) O_2 flow rates, (b) Ar quenching gas flow rates and (c) O_2 quenching gas flow rates. Circle, triangle and square represent β-Li_3BO_3, Li_2CO_3 and $LiOH·H_2O$, respectively.

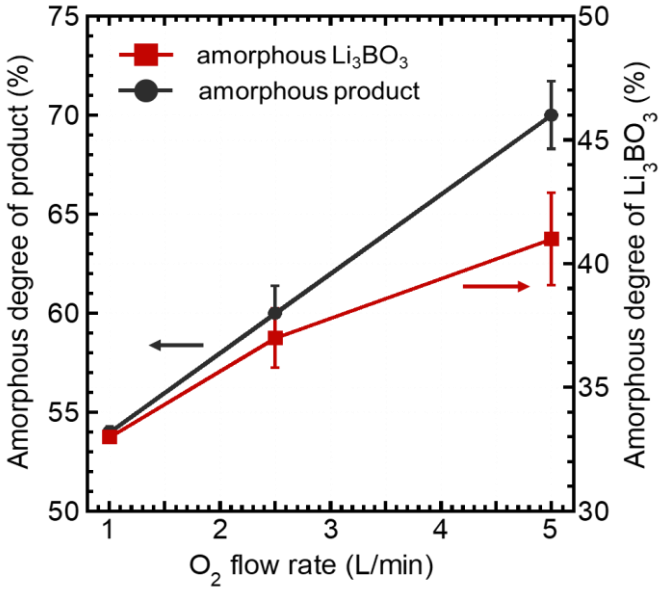

Fig. 2.4. Estimated amorphous degree of products and Li_3BO_3 synthesized by different O_2 flow rates. The error bars represent the standard errors of the corresponding average.

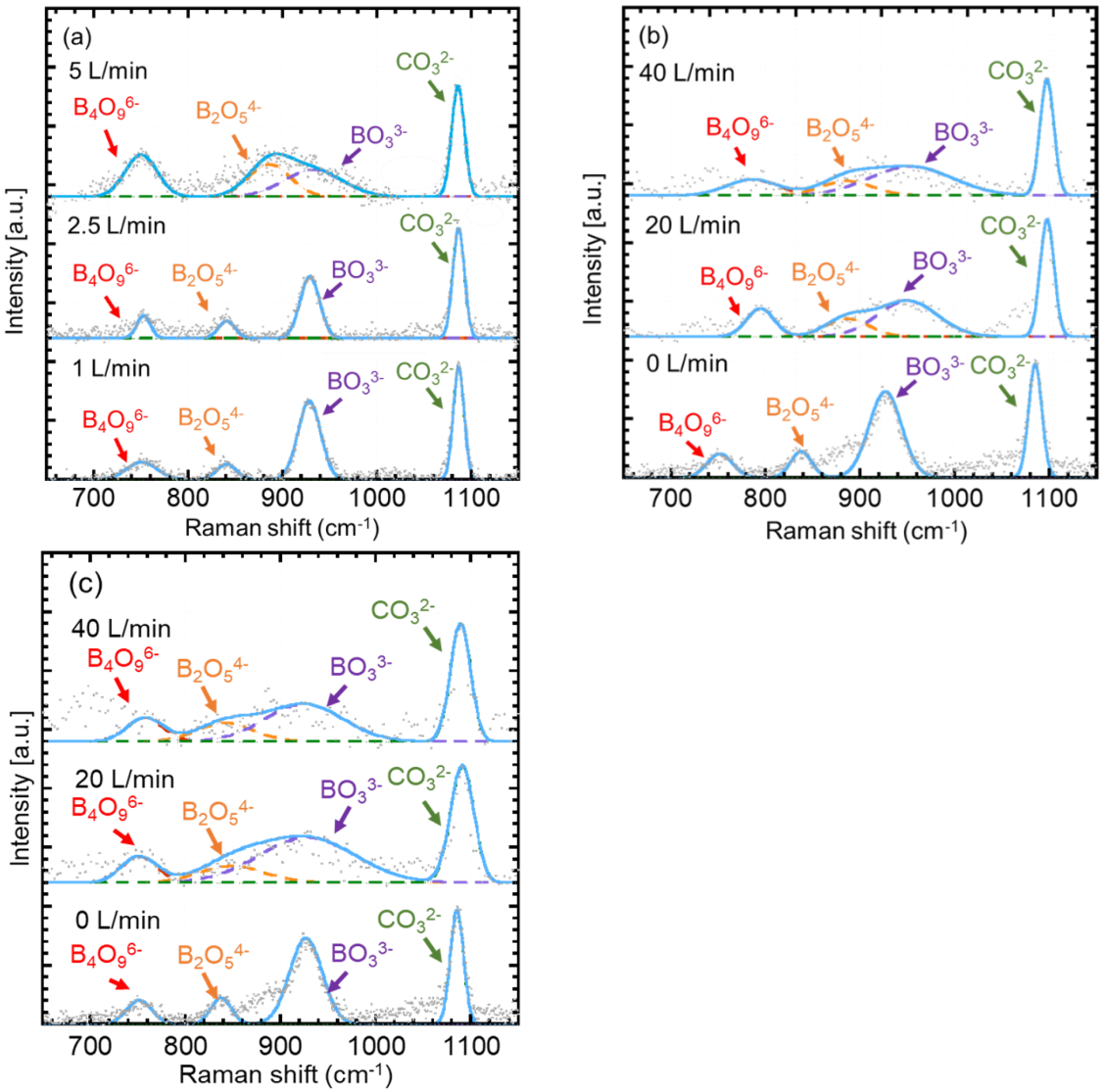

Fig. 2.5. Raman spectra of products synthesized by different (a) O_2 flow rates, (b) Ar quenching gas flow rates and (c) O_2 quenching gas flow rates. Gray dots line is the experimental results, the blue line is the cumulative fitting.

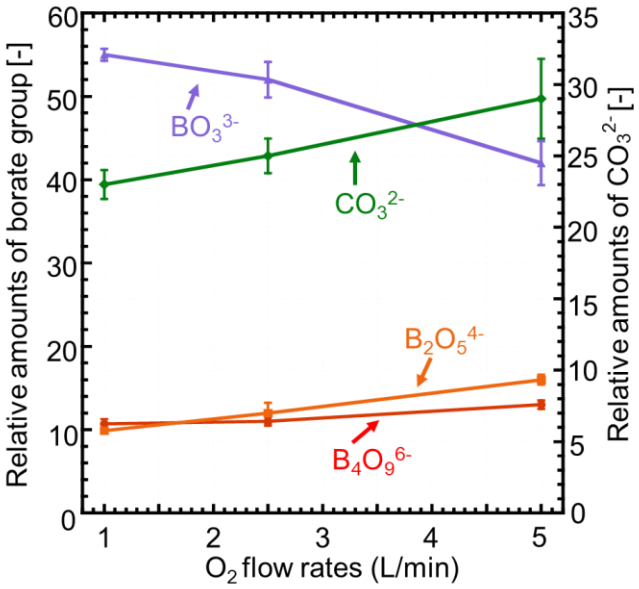

Fig. 2.6. The relative amounts of different groups in products synthesized by different O_2 flow rates. The error bars represent the standard errors of the corresponding average.

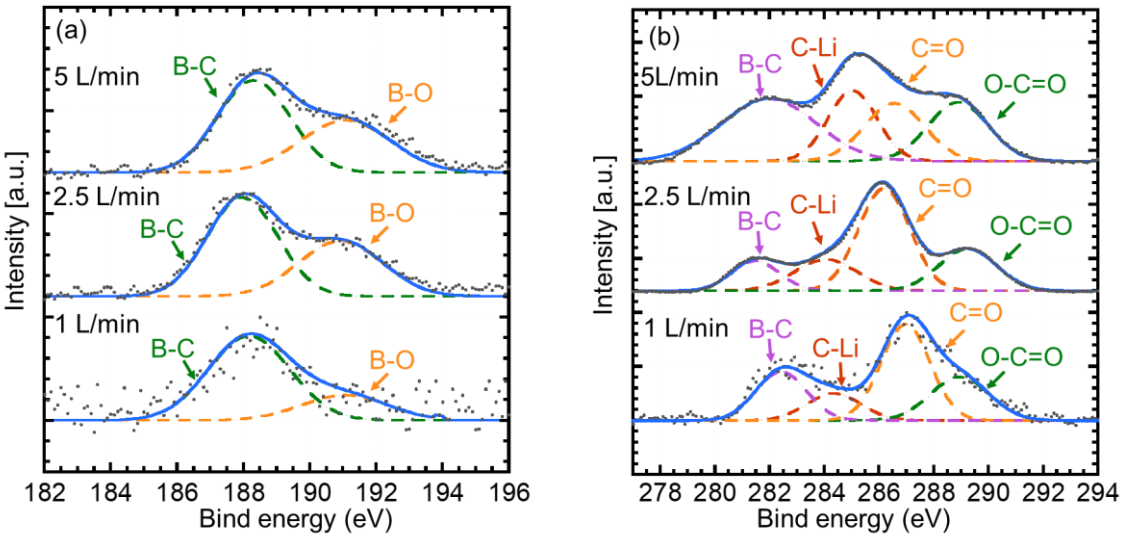

Fig. 2.7. XPS spectra of the products synthesized by different O_2 flow rates. (a) boron (1s) and (b) carbon (1s).

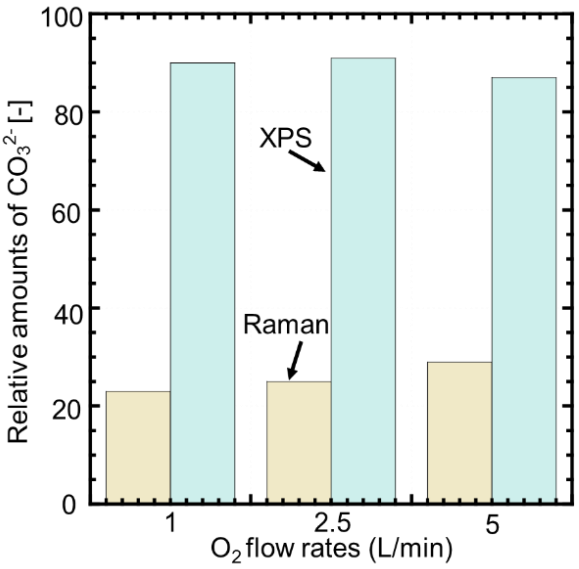

Fig. 2.8. Relative amounts of C in products estimated based on Raman and XPS with different O_2 flow rates.

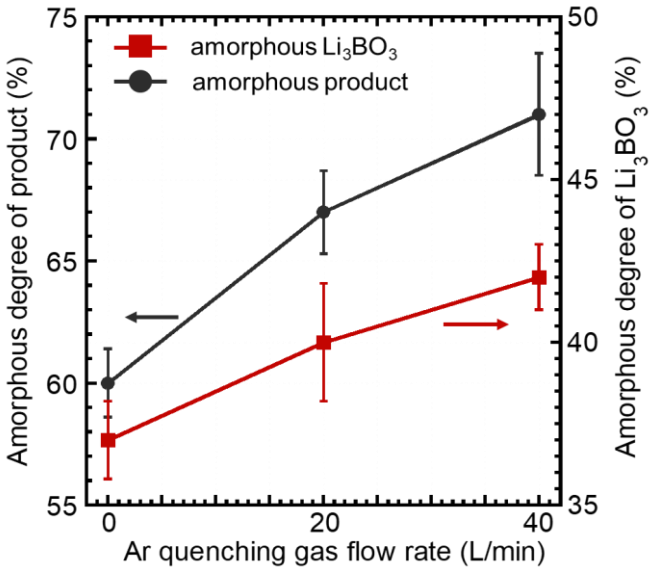

Fig. 2.9. Estimated amorphous degree of products and Li_3BO_3 synthesized by different Ar quenching gas flow rates. The error bars represent the standard errors of the corresponding average.

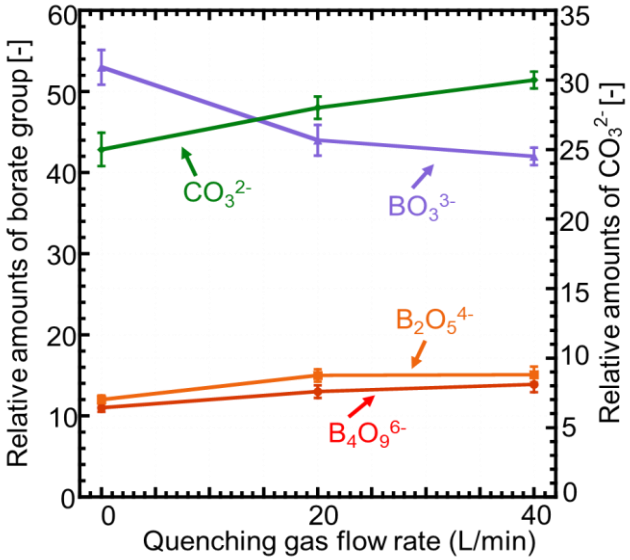

Fig. 2.10. The relative amounts of different groups in products synthesized by different Ar quenching gas flow rates. The error bars represent the standard errors of the corresponding average.

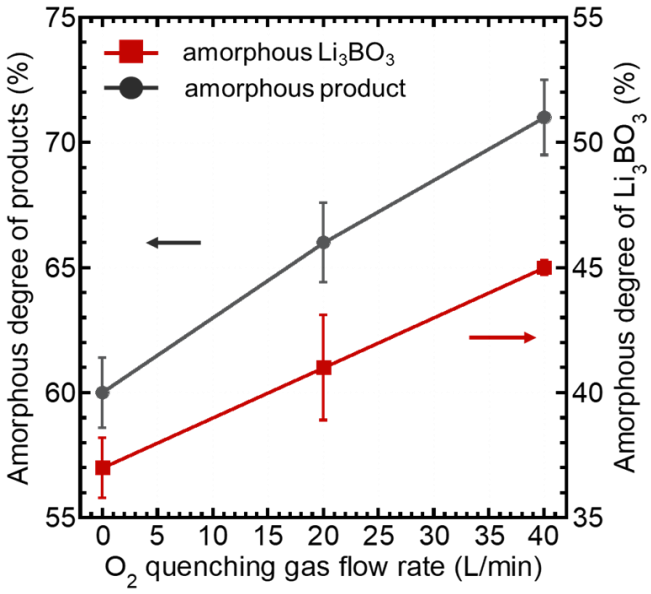

Fig. 2.11. Estimated amorphous degree of products and Li_3BO_3 synthesized by different O_2 quenching gas flow rates. The error bars represent the standard errors of the corresponding average.

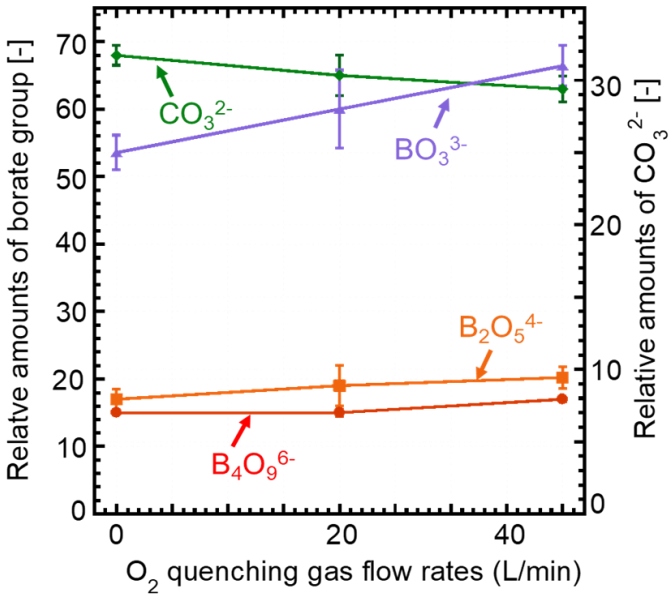

Fig. 2.12. The relative amounts of different groups in products synthesized by different O_2 quenching gas flow rates. The error bars represent the standard errors of the corresponding average.

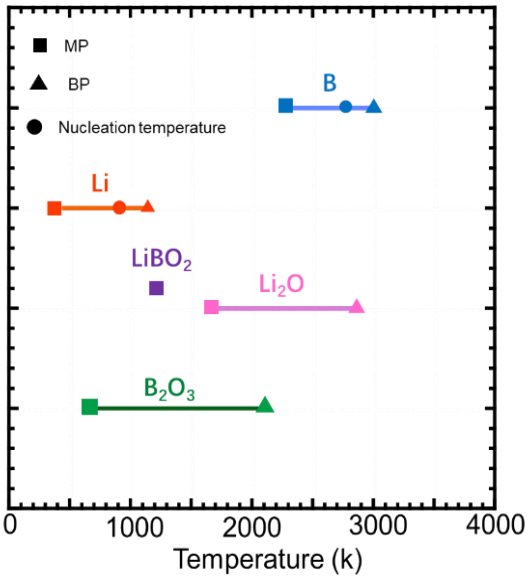

Fig. 2.13. The melting, boiling, and nucleation temperature relationship for B, Li and oxides.

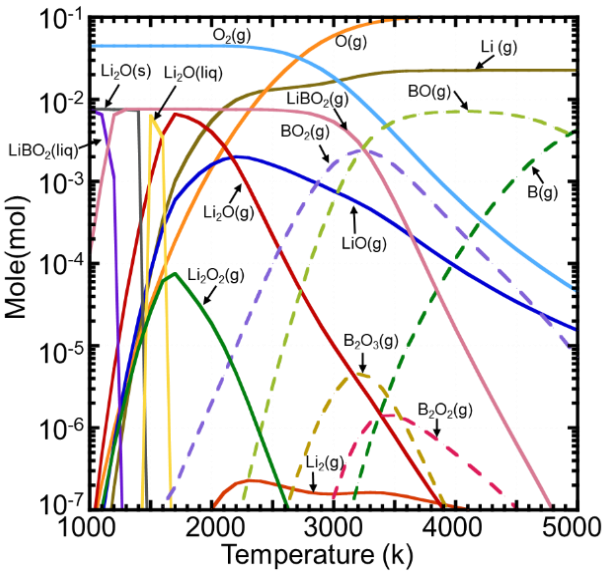

Fig. 2.14. Thermal equilibrium of the Li-B-O system: Li: B: O_2 = 3:1.5:115.

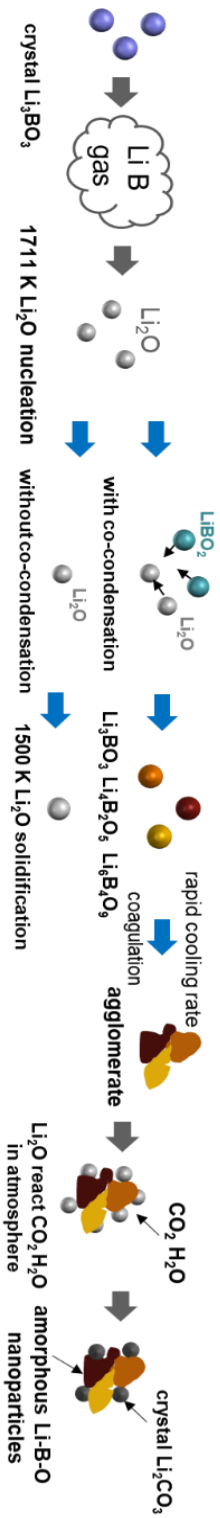

Fig. 2.15. Formation mechanism of Li-B-O powder by induction thermal plasma.

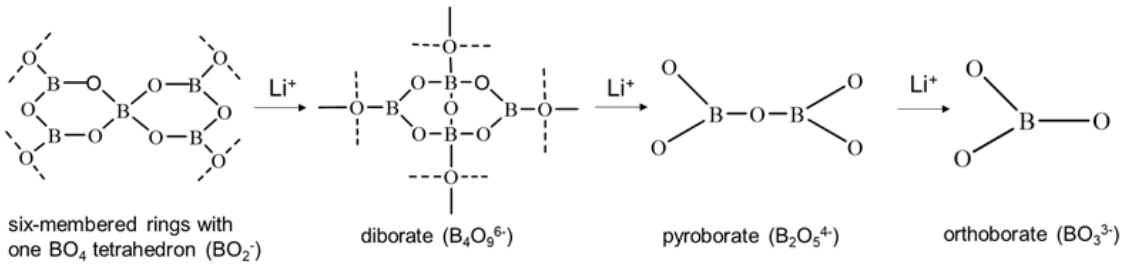

Fig. 2.16. Borate structure transformation process with Li^+ percentage increase.

3. Synthesis of Amorphous Li_4GeO_4 Nanoparticles

Solid electrolytes act as the Li ion transition bridge between anode and cathode, playing a critical role in cycling performance, operation temperature region, and life span of ASSBs [1]. Three main requirements were put forward for solid electrolytes: i) a high degree of disorder to allow ion mobile; ii) a high concentration of weakly bonded Li ion; iii) a suitable structure that allows macroscopic motion of Li ion with low activation energy [2]. Amorphous solid electrolytes known for the total disorder structure were introduced to satisfy the above requirements. Moreover, the isotropic Li ion conductivity in amorphous electrolytes is also beneficial to the application due to the minimization of the grain-boundary effect [3]. Low electronic conductivity is another significant requirement for solid electrolytes. The decreased overlap of electronic states of neighboring ions can be achieved by the disorder amorphous structure, further leading to reduced electron mobility and enhanced ionic transference number [4]. Overall, amorphous structure is a promising factor for solid electrolytes.

The amorphous Li_4GeO_4 was selected as the target material according to the following reasons. Germanium is a good glass former ascribing to the covalent bonds to promise amorphous structure generation. Meanwhile, the high Li content of Li_4GeO_4 ensures high Li ionic conductivity.

This chapter focuses on synthesizing amorphous Li_4GeO_4 nanoparticles by induction thermal plasma with different Li/Ge molar ratios, O_2 flow rates, and carrier gas and quenching gas flow rates. The effect of Ge percentage, O_2 flow rate, quenching rate, and formation mechanism were investigated based on experiment results and thermodynamic analysis.

3.1. Experimental

3.1.1 Experimental Configuration and Procedure

The experiment device consists of power supply, powder feeder, plasma touch, reaction chamber, quench tube, and collection filter, the schematic diagram is presented in **Fig. 3.1**. The experiments were operated under atmosphere pressure. The frequency of applied electromagnetic field was 4 MHz and the input power was fixed at 20 kW. The sheath gas consisted of Ar (purity > 99.9%, Fukuoka Oxygen) and O_2 (purity > 99.5%, Fukuoka Oxygen) with various molar ratios. Total flow rate was adjusted at 60 L/min. The quench tube was located 15 cm below the torch. Argon was selected as quenching gas injected into the reaction chamber by the quench tube with different flow rates. Oxygen was injected into chamber with 3 L/min after plasma process and lasted two minutes to ensure all lithium exist as compounds in products.

Raw material is the mixture of Li_2CO_3 (purity 99%, Honjo Chemical Corporation) and GeO_2 (purity 99.99%, Kojundo Chemical Laboratory) with different Li/Ge molar ratios. The raw material was injected into plasma torch at 300 mg/min. The Li/Ge and Ar/O_2 molar ratio were fixed at 4:1 and 57.5:2.5 in the experiments of carrier gas and quenching rate effect. There was no quenching gas injection in the experiment of Ge and Li content effect, the Ar/O_2 molar ratio was 57.5:2.5. The experiment conditions were summarized in **Table 3.1**.

3.1.2 Analysis Method

The phase identification of synthesized nanoparticles was conducted through X-ray diffraction (XRD, Rigaku Multiflex), operating with a Cu Kα source (λ = 0.1541 nm). The scan mode was set at a speed of 1°/min in the region 10°-90°. The structure of the amorphous part was understood through Raman spectrometer (Raman, LabRAM ARAMIS). The wavelength of laser source in this research was 532 nm. The morphology of products was characterized through transmission electron microscopy (TEM, JEOL JEM-2100HCKM) with an accelerating voltage of 200 kV. Two software, *JADE* 6.5 (Material Data, USA) and *FactSage* 7.2 (Centre for Research in

Computational Thermochemistry, Canada; GTT-Technology, Germany), were used to investigate the amorphous degree and thermodynamic composition during plasma process.

3.2 Experiment results

3.2.1 Effect of Germanium content in Raw Material

The morphology of nanoparticles synthesized by different Ge contents was understood through TEM. The TEM images with electron diffraction are shown in **Fig. 3.2 (a)-(d)**. The focus of electron beam in products is depicted as the red square. The halo in electron diffraction image represents amorphous structure and the unregular diffraction spots indicate low crystallinity. These images indicate the products exist as agglomerated states insides of isolated spherical particles. The diameter of nanoparticles is around 40-50 nm indexed by orange circle.

Temperature influences the morphology of the products during the particle growth process [5]. Particle coalescence is more rapid than coagulation at high temperature. This phenomenon allows spherical particle formation. Coagulation becomes obvious gradually compared to coalescence with temperature decrease. This is because there is no sufficient energy to achieve particle boundary elimination. Agglomerates are formed at low temperature due to coagulation being dominant [6]. The temperature of particle growth in Li-Ge-O system is lower than 1700 K. The reaction temperature region was estimated by thermodynamic equilibrium and the result is shown in section 3.3.1. Thereby, agglomerates instead of spherical particles are formed in Li-Ge-O system.

Figure 3.3 is the XRD spectra for products synthesized by different Ge contents. The low temperature phase Li_4GeO_4 (α-Li_4GeO_4) and high temperature phase Li_4GeO_4 (γ-Li_4GeO_4) are the main products in the crystal part. Peaks belonging to Li_2GeO_3 are also detected as the by-product. There is a phase transition from γ-Li_4GeO_4 to α-Li_4GeO_4 around 1006 K [7]. The rapid quenching

rate of induction thermal plasma prevents the phase transition, allowing the γ-Li_4GeO_4 to remain in products. Peak intensity of γ-Li_4GeO_4 becomes stronger with Ge molar content increase. This tendency results from the enlarged O-Ge-O angle distribution in high Ge cases and will be discussed in the section 3.3.2.

The estimated amorphous Li_4GeO_4 degree for different Li/Ge molar ratios is shown in **Fig. 3.4**. This result is estimated by *JADE* 6.5 according to XRD spectra using **Eqs. (2.1) - (2.2)**. Classification of crystalline and broad amorphous peaks is important based on **Eq. (2.1)**. There are no obvious and sharp peaks in XRD spectrum for amorphous compounds, instead, the broad amorphous peak emerges. Different compounds own different 2θ for their amorphous peaks [8]. Amorphous peaks for amorphous Li_4GeO_4 and Li_2GeO_3 are located around 22 and 30 degree, respectively [9,10]. The amorphous Li_4GeO_4 degree is obtained by only estimating the amorphous peak at 22 degree. The estimated amorphous degree rises from 23% to 39% with the molar ratio of Li/Ge rising from 4:1 to 4:1.5. This increase demonstrates Ge promotes amorphous Li_4GeO_4 generation.

Tetrahedron [GeO_4] is the fundamental structure unit for lithium germanate glass, the schematic diagram is shown in **Fig. 3.5 (a)**. The network of amorphous lithium germanate is built by [GeO_4], lithium ions locate in the hole of the network. The strong Ge-O bond is beneficial to resist the destruction of network caused by the Li_2O addition. The topological disorder structure is preserved by the rapid quenching rate, further achieving the amorphous structure in lithium germanate. The Q^n species distribution reflects structure of lithium germanate glass [11,12]. The *n* represents the bridge oxygen (BOs) number connected with tetrahedron [GeO_4]. The schematic diagram of Q^n is presented in **Fig. 3.5 (b)**. Raman spectrum analysis was conducted to investigate Q^n distribution for products.

The Raman spectra are presented in **Fig. 3.6 (a)-(c)**. The gray dots line and blue line represent

the experimental spectrum and cumulative fitting, respectively. The characteristic peaks are fitted by Gaussian function. There are five typical peaks are identified, indicating products consist of five germanate units. Peaks are marked as orange dots line located around 500-600 cm^{-1} and 730-760 cm^{-1} are belonged to GeO_4^{4-} with bending and stretching vibration, respectively [13]. Peak around 800-810 cm^{-1} is indexed to isolated GeO_3^{2-} in purple dots line [14]. The Q^2, tetrahedral [GeO_4] with 2 BOs, species peak around 770-780 cm^{-1} with green dots line. Two types of Q^3 species are observed to exist in lithium germanate glass, they are Q^{32} (tetrahedral [GeO_4] with 3 BOs connected with Q^2) and Q^{33} species (tetrahedral [GeO_4] with 3 BOs connected with same Q^3), respectively [15,16]. The Q^{32} and Q^{33} species peaks are located around 830-850 cm^{-1} and 850-880 cm^{-1} marked pink dots line [15].

Figure 3.7 displays the relative amount of each germanate unit in products synthesized by Ge contents. The relative amounts of each unit can be estimated based on the assumption that the total number of Raman scattering gives rise to the area under the peaks [17]. Estimated result demonstrates that isolated GeO_4^{4-} percentage occupies the highest point in Li/Ge of 4:1 around 49%, then decreases with Ge molar content increasing because a higher amorphous degree is achieved. Increased Ge molar content results in more Li_2GeO_3 synthesized due to the higher Ge molar amount. The percentage of Q^2 specie is lower than Q^3 in synthesized nanoparticles. Since "germanate anomaly" in lithium germanate glass, the Q^n specie distribution is different with lithium silicate glass [16]. The Q^2 percentage reaches the maximum of around 20 % of total Q^n at 10 mol% lithium content, then declines with lithium increase. The Q^3 percentage experiences the same increase tendency as the Q^2 percentage with Li content increasing to 10 mol%. A continuous enhancement is observed in Q^3 percentage with Li content continuously increasing higher than 10 mol%, while the Q^2 percentage displays an opposite tendency. Therefore, lithium germanate glass with high Li content (Li≥10 mol%) shows a higher value of Q^3 percentage [18].

The above results demonstrate that Ge as the glass former in lithium germanate glass has a positive effect both on amorphous Li_4GeO_4 and high temperature phase Li_4GeO_4 generation. This phenomenon is influenced by topology of tetrahedron [GeO_4] and the reason will be discussed in the section 3.3.2 and 3.3.3.

3.2.2 Effect of Quenching Gas

Quenching rate effect is also studied due to the enhanced quenching rate having a positive effect on amorphous nanoparticles synthesis [19]. **Figure 3.8 (a)-(d)** displays the TEM images with electron diffraction of nanoparticles synthesized by different quenching gas flow rates. The red square is the focus of the electron beam on product. The halo in electron diffraction image demonstrates amorphous structure. The agglomerated state is also observed in products. The particles indexed by the orange circle show the diameter of 20-30 nm, indicating that quenching gas utilization allows tinier particle generation. This is because quenching gas injection decreases temperature obviously, and more nuclei are generated. The vapor consumption of each nucleus would be declined because the total amount of vapor is constant. Thus, the smaller nanoparticles are obtained with quenching gas injection.

The XRD spectra of the products synthesized by different quenching gas flow rates are shown in **Fig. 3.9**. The main product is crystalline α-Li_4GeO_4 in the case without quenching gas. Crystal peak intensity decreases with quenching gas flow rate increasing to 10 L/min, simultaneously, the α-Li_4GeO_4 peaks disappear. Only the γ-Li_4GeO_4 peaks are observed due to the enhanced quenching rate. The Li_2CO_3 peaks are detected as another by-product besides Li_2GeO_3. The raw material would be totally evaporated and decomposed in high temperature region, and the vapor reactions occur. The C vapor would be reacted with O vapor to form CO_2 and CO vapor above 4000 K based on thermodynamic equilibrium composition in section 3.3.1. The Gibbs energy

change of Li_2CO_3, CO and CO_2 synthesis is shown in **Fig. 3.10**, indicating the Gibbs energy change of CO_2 and CO synthesis is negative and is much lower than Li_2CO_3 above 4000 K. The CO_2 and CO are synthesized preferentially contrasted to Li_2CO_3 at high temperature. These synthesized CO_2 and CO vapor exhaust from system by the vacuum pump as soon as they generate. The lithium germanante nanoparticles are synthesized under 1700 K based on the formation mechanism. Namely, the CO_2 cannot take part in the reaction and Li_2CO_3 would not be synthesized during plasma process. Since the enhanced quenching rate impairs Li_2O condensation and accelerates Li_2O solidification, the unreacted Li_2O would be reserved in products. These Li_2CO_3 are synthesized by unreacted Li_2O with H_2O and CO_2 in atmosphere after plasma process during collection.

Main product gradually changes to Li_2GeO_3 in crystal part with the quenching gas flow rate continuously increasing to 20 L/min. This situation is associated with the supersaturation ratio for each compound in Li-Ge-O system, more details will be discussed in section 3.3.1 after formation mechanism investigation.

Figure 3.11 presents the estimated amorphous Li_4GeO_4 degree of product synthesized by different quenching gas flow rates. Amorphous Li_4GeO_4 degree increases to around 65% after 10 L/min quenching gas injection. However, this value declines to around 57% and 36 % with quenching gas flow rates increasing to 15 L/min and 20 L/min, respectively. This situation relates to the composition of the final product, the enhanced quenching rate impairs Li_4GeO_4 synthesis. The less total amount of Li_4GeO_4 in 15 L/min and 20 L/min cases results in the relative amount of amorphous Li_4GeO_4 also experiencing a decrease. Thus, the maximum of amorphous Li_4GeO_4 is achieved in the 10 L/min case. More details will be discussed in section 3.3.1 after the formation mechanism.

The products synthesized by different quenching gas flow rates consist of GeO_4^{4-}, GeO_3^{2-}, Q^2,

and Q^3 based on Raman analysis. **Figure 3.12** shows the quantified result of Raman spectra. The GeO_4^{4-} percentage shows a declining trend with the rise of quenching gas flow rate. An obvious increase is observed in GeO_3^{2-} from 7% to 18% with flow rate increasing from 0 L/min to 20 L/min. This tendency is consistent with XRD results. The Q^3 percentage presents a rise with quenching gas flow rate increase, while the Q^2 percentage has an opposite tendency. This situation demonstrates fewer non-bridge oxygen NBO bonds in the amorphous part of products at high flow rate of quenching gas. Since the enhanced quenching rate impairs Li_2O dominant condensation, meaning less Li_2O participates in reactions and more BO bonds are preserved in high flow rate cases. The relationship between quenching gas flow rate and condensation rate will discuss in the section 3.3.1.

The above results reveal quenching gas injection benefits amorphous Li_4GeO_4 generation and high temperature phase preservation. However, the excessive quenching gas flow rate prevents Li_4GeO_4 generation.

3.2.3 Effect of Carrier Gas

Rapid quenching rate is a significant factor for amorphous nanoparticle synthesis. Besides counter-flow quenching gas injection and addition of O_2 into sheath gas, enhancement of carrier gas flow rate also allows particles to pass through plasma faster. Namely, high carrier gas flow rate reduces the particle residence time and accelerates particle solidification. Thus, the effect of carrier gas flow rate was investigated. The raw material was injected into plasma by 3 L/min, 4.5 L/min and 6 L/min Ar carrier gas, the feeding rate was fixed at 300 mg/min. The Li/Ge molar ratio in raw material was 4:1, no quenching gas injection during plasma process.

Figure 3.13 displays the XRD spectra of nanoparticles synthesized by different carrier gas flow rates. The spectra demonstrate that no α-Li_4GeO_4 synthesized in 4.5 and 6 L/min cases rather than

γ-Li_4GeO_4 peaks are observed in crystalline part. Meanwhile, the Li_2GeO_3 peaks gradually become dominant with carrier gas flow rate increase. The amorphous peak is observed obviously in 4.5 and 6 L/min cases, meaning more amorphous nanoparticles are obtained in high flow rate cases. The estimated amorphous Li_4GeO_4 degree is presented in **Fig. 3.14**, indicating the amorphous degree increases to 54% in 6 L/min case. The enhanced flow rate of carrier gas leads to the particles passing through the high temperature region more rapidly, which reduces the duration time of liquid state and prevents the structure transformation from disorder to order. Hence, the enhanced flow rates benefit amorphous nanoparticles synthesized due to shortening residence time.

The Raman spectra indicate four germanate structure units GeO_4^{4-}, GeO_3^{2-}, Q^2, and Q^{33} and Q^{32}, in products. **Figure 3.15** is the results of qualified Raman spectra, indicating the percentage of GeO_4^{4-} and Q^2 experience a downward tendency with flow rate increase. This is because less Li_2O takes part in the reaction and more BOs are preserved. In addition, the Li_2GeO_3 percentage presents an increase, resulting from the promoted GeO dominant condensation which is achieved in high flow rate cases. More details will be discussed in section 3.3.1.

Above results reveal that the short duration time in thermal plasma benefits amorphous and high temperature phase Li_4GeO_4 synthesized, while also resulting in the by-product Li_2GeO_3 being synthesized.

3.2.4 Effect of Lithium Content in Raw Material

The above experiment results present that Li_2GeO_3 with a Li/Ge molar ratio of 2 exists in products, while the Li/Ge molar ratio is 4 in raw material. Lithium loss occurs during the plasma process. Hence, the experiment on excess Li in raw material was conducted. The Li/Ge molar ratio was 4:1, 4.25:1, and 4.5:1, respectively. The raw material was injected into plasma at 300

mg/min. There was no quenching gas utilization during plasma process.

Figure 3.16 shows the XRD spectra of nanoparticles synthesized by different Li contents. The main product in crystal part is Li_2GeO_3, the Li_4GeO_4 exists as high temperature phase γ-Li_4GeO_4. In addition, another by-product Li_2CO_3 is observed. By-product Li_2CO_3 is considered synthesized by CO_2 in the atmosphere and unreacted Li_2O during collection time according to section 3.2.2 discussion. The detection of Li_2CO_3 means there is still some Li_2O not taking part in reaction during plasma process.

The increased Li content in raw material allows Li_2O to achieve supersaturation earlier. The Li-rich Li_4GeO_4 is mainly synthesized at the early stage of condensation, the earlier achievement of supersaturation leads to Li_4GeO_4 being synthesized at the higher temperature position. The synthesized and unstable Li_4GeO_4 would decompose into Li_2O, GeO and O_2 due to the high temperature, these decomposed Li_2O and GeO flow to the downstream region. Because the solidification temperature of Li_2O is higher than that of GeO, the Li_2O would earlier solidify at the downstream region than GeO. This phenomenon impairs the Li_2O participation of reaction and results in more GeO-rich Li_2GeO_3 being synthesized. The amorphous Li_4GeO_4 degree of products synthesized by different Li content is displayed in **Fig 3.17**, indicating there is no obvious discrepancy in three cases although the amorphous peak can be clearly observed in high Li content cases. This is because the total amount of Li_4GeO_4 decreases in high Li content cases.

The Q^n species distribution was estimated based on Raman spectra and shown in **Fig. 3.18**. The percentage of GeO_3^{2-} experiences an upward tendency while GeO_4^{4-} has an opposite trend, corresponding to XRD results.

3.2.5 Effect of Oxygen Flow Rate

Addition of diatomic O_2 into monoatomic Ar sheath gas can shrink plasma flow, this situation

prefers amorphous structure synthesis based on Chapter 2 results. Here, the O_2 flow rate effect was also studied. The value of molar ratio is shown in **Table. 3.1**. The Li/Ge molar ratio of raw material was 4:1, there is no quenching gas injection during the plasma process.

Figure 3.19 is the XRD spectra of nanoparticles synthesized by different O_2 flow rates. The main product of three conditions is α-Li_4GeO_4, the peak intensity of γ-Li_4GeO_4 and Li_2GeO_3 becomes obvious with O_2 flow rates increase. Plasma flow is shrunk by adding diatomic gas O_2 into Ar, the steeper temperature gradient is obtained due to the higher thermal conductivity of O_2. This phenomenon contributes to high temperature phase γ-Li_4GeO_4 being preserved. Meanwhile, the steeper temperature gradient allows following-stage condensation to be advanced and promotes GeO condensation. Increased Li_2GeO_3 is acquired at high O_2 flow rate cases.

Figure 3.20 displays the amorphous Li_4GeO_4 degree of nanoparticles synthesized by different O_2 flow rates. Since the steeper temperature gradient caused by O_2 addition, an increase tendency is observed in amorphous Li_4GeO_4 degree with O_2 flow rate rising. This result also indicates three conditions have low amorphous degree, the 5 L/min case occupies the highest amorphous degree of 25%.

3.3. Discussion

3.3.1 Formation Mechanism of Lithium Germanate Nanoparticles

The formation mechanism of amorphous nanoparticles synthesized by induction thermal plasma is investigated in order to understand the experiment results deeply and theoretically. Since the unique superiority of induction thermal plasma, the formation mechanism of this advanced fabrication method is different from the conventional method [6].

The raw materials evaporate and decompose immediately in high temperature region after injecting into thermal plasma. Atoms collide with each other to form small clusters (embryos)

containing a few molecules by vapor phase reactions or just by coalescence. Actually, most of these small clusters would disappear in a short time because most of them are thermodynamically unstable. Simultaneously, these small clusters are transported to lower temperature region. Vapor saturation pressure declines due to temperature decrease, the partial vapor pressure exceeds saturation pressure to reach supersaturation. Nuclei are generated under the size of embryos achieve critical crystal size and the vapor satisfies supersaturate. This supersaturation vapor is identified as the nucleation phase. Particles grow continuously by heterogeneous co-condensation which starts as soon as nucleus generation in plasma. Condensation phase is considered as the vapor participating in condensation except for nucleation vapor. Nucleation phase and condensation phase co-condense on the surface of nuclei and mix well in the liquid state before solidification. Various reactions occur to form different compounds during the condensation process. Subsequently, coagulation starts after compound particle solidification starts by colliding with each other randomly. Finally, nanoparticles are synthesized after nucleation, condensation, and coagulation [20,21].

Clarification of the nucleation and condensation phase during the plasma process is necessary according to above nanoparticle generation process. The nucleation temperature of each substance in Li-Ge-O system is investigated based on **Eqs. (2.3) - (2.6)**.

The nucleation temperatures for Li and Ge are 974 K and 2155 K under 300 mg/min feeding rate, respectively. Because the physical properties of oxides are limited and nucleation temperature is similar to melting point [22]. The melting point is regarded as the nucleation temperature for oxides in this study. **Figure 3.21** presents the nucleation temperature of the Li, Ge and the boiling point, melting point of oxides in Li-Ge-O system. Melting point and boiling point are obtained from Lang's Handbook of Chemistry [23]. **Figure 3.21** demonstrates that Ge occupies the highest nucleation temperature and should nucleate first in Li-Ge-O system.

The homogenous nucleation also strongly depends on the saturation ratio besides the nucleation temperature. Thermodynamic equilibrium composition for Li-Ge-O system from 1000 K to 5000 K is investigated aiming to understand the partial vapor pressure of different species around their nucleation temperature. The nuclei cannot stably exist at high temperature because the high temperature would result in generated nuclei decomposing. The nucleation phase and condensation phase would be solidified below 1000 K in Li-Ge-O system. The thermodynamic equilibrium composition is estimated with a temperature range of 1000-5000 K. The estimated result is shown in **Fig. 3.22**. This result was developed by *FactSage* 7.2 with following conditions. Raw material feeding rate is fixed at 300 mg/min. Sheath gas flow rates for Ar and O_2 are 57.5 L/min, and 2.5 L/min, respectively. The nuclei cannot stably exist at high temperature because the high temperature would result in generated nuclei decomposing. The nucleation phase and condensation phase would be solidified below 1000 K in Li-Ge-O system. The thermodynamic equilibrium composition is estimated with a temperature range of 1000-5000 K, the ion content is very low in this temperature region. Thus, the ion effect can be negligible.

This result demonstrates that Ge vapor is consumed by the reaction with O vapor to form into GeO vapor below 4000 K. Partial vapor pressure of Ge is too low to support Ge nucleation around 2155 K. Germanium is not the nucleation phase in Li-Ge-O system. Meanwhile, there is an obvious deviation in the Li_2O boiling point. This is because Li mainly exists as Li vapor and LiO vapor at high temperature, the Li_2O cannot achieve saturation state caused by the low partial vapor pressure. The Li_2O nucleates around 1700 K following Ge according to **Fig. 3.21**. Moreover, the vapor pressure of Li_2O is also sufficient to satisfy supersaturation around its nucleation temperature. Therefore, the nucleation phase can be identified as Li_2O in Li-Ge-O system.

The formation mechanism is put forward based on thermodynamic analysis and experiment results. The process is shown in **Fig. 3.23**. The mixture of GeO_2 and Li_2CO_3 decomposes

completely in high temperature region, then particles react with each other in vapor phase. The GeO and Li_2O vapor are synthesized during this period. Continuously produced Li_2O vapors flow to downstream with lower temperature. Homogeneous nucleation starts when the saturation ratio of Li_2O achieves unity. Vapor of GeO and Li_2O start to heterogeneously co-condense on Li_2O nucleus subsequently. The Li-Ge-O particles are generated in this period.

Condensation is driven by the saturation ratio during the plasma process [24]. The Li_2O-rich particles Li_4GeO_4 are synthesized at early stage of condensation ascribing to a higher saturation ratio of Li_2O than GeO. **Equation (3.1)** is the dominant reaction at the early stage. The dominant reaction is replaced gradually by **Eq. (3.2)** with Li_2O vapor consumption and GeO vapor starts to achieve supersaturation. The GeO-rich particles Li_2GeO_3 are synthesized mainly at the following stage. The synthesized Li_4GeO_4 and Li_2GeO_3 particles grow continuously by coagulation after solidification starts. Finally, particles reach filter and wall of inner chamber.

$$GeO\ (g)+2Li_2O\ (l)+\frac{1}{2}O_2(g)\rightarrow Li_4GeO_4(s) \tag{3.1}$$

$$GeO\ (g)+Li_2O\ (l)+\frac{1}{2}O_2(g)\rightarrow Li_2GeO_3(s) \tag{3.2}$$

The rapid quenching rate impedes the order growth of particles during plasma process [25]. Amorphous structure is achieved due to the chaotic structure being preserved. This impedance can be intensified by high quenching rate. Thus, enhanced amorphous degree is achieved after quenching gas injection.

The formation mechanism can explain the composition variation of products synthesized by different quenching gas and carrier gas flow rates. The synthesis of Ge-rich Li_2GeO_3 is mainly driven by GeO dominant condensation at the following condensation stage based on the formation mechanism. Promoted GeO condensation results in more Li_2GeO_3 synthesis. The duration of Li_2O

dominant condensation is shortened after quenching gas injection and carrier gas enhancement. Because synthesized particles earlier reach low temperature region due to the sharper temperature gradient caused by enhanced quenching gas and carrier gas flow rate. Saturation ratio of GeO is risen simultaneously ascribing to lower temperature, which allows the GeO dominant condensation to be advanced. These phenomena promote GeO condensation and GeO-rich Li_2GeO_3 generation. The recirculation zone is also suppressed by the quenching gas injection, resulting in the reduction of particle growth time. There is no adequate time for Li_2O to condense on the nucleus. These unreacted Li_2O is transported to low temperature region for solidification, further contacting with H_2O and CO_2 to form Li_2CO_3 during collection time. Hence, the percentage of Li_2GeO_3 rises with the quenching gas and carrier gas flow rate increase, moreover, the Li_2CO_3 is detected as the by-product in high quenching gas flow rate cases. The declined amorphous Li_4GeO_4 degree was observed in 15 L/min and 20 L/min quenching gas cases resulting from the less Li_4GeO_4 synthesis under excessive quenching gas.

3.3.2 Short-range Order in Amorphous Lithium Germanate

The amorphous material shows topological disorder in structure [26,27]. The short-range order (SRO), in the range 2-5 Å, of amorphous lithium germanate is quantified by distribution of intratetrahedral O-Ge-O angle [28]. **Figure 3.24 (a)** shows the illustration of intratetrahedral O-Ge-O angle. The O-Ge-O angle ranges from 80 to 160 degrees at high temperature, while this range shrinks to 90 to 110 degrees at room temperature [29]. The rapid quenching rate allows broad intratetrahedral O-Ge-O angle distribution to be preserved after the plasma process. These chaotic angles increase the disorder of product in SRO, which benefits amorphous structure formation. Enhanced quenching rate facilitates preservation of broad angle distribution. The more chaotic state is obtained in SRO. Therefore, the higher amorphous Li_4GeO_4 degree is acquired

after quenching gas injection.

The intratetrahedron O-Ge-O angular excursion is also enlarged with Ge composition increase. Increased Ge molar amount broadens intratetrahedral O-Ge-O angle distribution in germanate glass [30]. Since the increase of Ge composition inevitably leads to Ge-Ge homopolar bonds occurring, further leading to more small rings generation in amorphous [31,32]. These small rings allow amorphous transforms to stressed rigid phase which occupies the high network connectivity. Asymmetric bending motions in [GeO_4] tetrahedron occur as the additional cross-links force to soften interactions in order to adapt and break the corresponding constraint [33]. This phenomenon leads to the broader O-Ge-O angle distribution and higher SRO chaos degree. Increased amorphous Li_4GeO_4 degree is obtained because more chaotic state is achieved in SRO in high Ge molar amount case. Therefore, an increase tendency in amorphous degree is observed with Ge molar content increase in raw material.

The enhanced intensity of γ-Li_4GeO_4 peaks is also observed with Ge molar content increase, this situation is also associated with the intratetrahedral O-Ge-O angle distribution. The high temperature phase γ-Li_4GeO_4 occupies a wider angular distribution than low temperature phase α-Li_4GeO_4 [29]. Thus, enlarged O-Ge-O angle distribution also facilitates γ-Li_4GeO_4 synthesis in high Ge content cases.

3.3.3 Intermediate-range Order in Amorphous Lithium Germanate

Intermediate-range order (IRO) in the range 5-20 Å is another index of topological order to describe the amorphous structure. The intertetrahedral angle Ge-O-Ge distribution represents IRO in amorphous lithium germanate [34]. The illustration is presented in **Fig. 3.24 (b)**. Tetrahedrons [GeO_4] are linked with each other through corner-sharing rather than edge-sharing in amorphous lithium germenate. This phenomenon allows the most conformational flexibility in the relative

rotational orientation among [GeO_4] tetrahedrons, which contributes to amorphous structure formation. The angle distribution of Ge-O-Ge is also affected by temperature. The increasingly broader angular distribution is observed with temperature rise [29]. Transformation of the Ge-O-Ge angle into a constant can be prevented by the fast quenching rate during the plasma process, further achieving the disorder in product and obtaining amorphous nanoparticles.

Enhanced quenching rate benefits the preservation of broader Ge-O-Ge angle distribution. This phenomenon increases the chaotic state in IRO of products. The quenching rate increases from 3.2×10^4 K/s without quenching gas to 1.3×10^5 K/s after 20 L/min quenching gas injection [20]. Thus, the increased amorphous Li_4GeO_4 degree can be achieved after quenching gas injection ascribing to the higher IRO chaos. The quenching gas injection benefits high disorder both in SRO and IRO simultaneously, further achieving the higher amorphous degree of lithium germanate.

3.4. Conclusion

Amorphous Li_4GeO_4 nanoparticles were synthesized by induction thermal plasma successfully first time. The formation mechanism was investigated based on thermodynamic analysis and experiment results. Effect of short-range and intermediate-range order on product composition, structure and amorphous degree is studied.

The chemical discrepancy was presented in lithium germanate nanoparticles synthesized at different stages of heterogeneous condensation. Lithium-rich nanoparticles Li_4GeO_4 are mainly synthesized at early stage of condensation because of more rapid condensation rate of Li_2O than GeO. By-products Li_2GeO_3 are mainly synthesized at the following condensation stage which GeO condensation is dominant. Duration time of Li_2O dominant condensation is pressed by steeper temperature gradient which is caused by counter quenching gas injection. Hence, more

Li_2GeO_3 are synthesized under quenching gas with high flow rate. Angle distribution of intratetrahedral O-Ge-O and intertetrahedral Ge-O-Ge is wider in high temperature. Increased quenching rate prevents the flexible angles transform to the fixed value. The disorder in SRO and IRO is preserved, and an enhanced amorphous degree is achieved, the increased quenching rate contributes to high amorphous degree due to impairment of particles growth in order in long range.

Increased glass former Ge content in raw material benefits amorphous Li_4GeO_4 and high temperature phase γ-Li_4GeO_4 formation. Because more Ge allows intratetrahedral O-Ge-O angle achieves enlarged angular distribution which enhances product disorderly in SRO. Simultaneously, this extended angle distribution which is reserved by rapid quenching rate allows more γ-Li_4GeO_4 remain in products after plasma processing.

Reference:

[1] B.B. Owens, P.M. Skarstad, Ambient temperature solid state batteries, Solid State Ion. 53–56 (1992) 665–672. https://doi.org/10.1016/0167-2738(92)90444-T.

[2] K.N. A.M. Glass, Lithium ion conduction in rapidly quenched Li_2O-Al_2O_3 Li_2O-Ga_2O_3 and Li_2O-Bi_2O_3 glasses, Functional Oxides. 3756 (1980) 119–202. https://doi.org/10.1002/9780470686072.ch3.

[3] T. Heitmann, G. Hester, S. Mitra, T. Calloway, M.S. Tyagi, A. Miskowiec, S. Diallo, N. Osti, E. Mamontov, Probing Li ion dynamics in amorphous $xLi_2SO_4 \cdot (1-x)\ LiPO_3$ by quasielastic neutron scattering, Solid State Ion. 334 (2019) 95–98. https://doi.org/10.1016/j.ssi.2019.02.004.

[4] Murphy, D.W., Broadhead, J., Steele, B.C.H. Materials for Advanced Batteries. Plenum Press: New York, 1980.

[5] M.T. Swihart, Vapor-phase synthesis of nanoparticles, Curr Opin Colloid Interface Sci. 8 (2003) 127–133. https://doi.org/10.1016/S1359-0294(03)00007-4.

[6] S. Samal, Synthesis of TiO_2 Nanoparticles from Ilmenite Through the Mechanism of Vapor-Phase Reaction Process by Thermal Plasma Technology, J Mater Eng Perform. 27 (2018) 2622–2628. https://doi.org/10.1007/s11665-017-3060-5.

[7] S. Wan, S. Zhang, X. Gong, Y. Zeng, S. Jiang, J. You, Structural investigations on two typical lithium germanate melts by: In situ Raman spectroscopy and density functional

theory calculations-supplyment, CrystEngComm. 22 (2020) 701–707. https://doi.org/10.1039/c9ce01512d.

[8] J.M.C.W. bin Xu, Methods for Determining Relative Crystallinity of Plant Starch X-ray Powder Diffraction Spectra, Chinese Bulletion of Botany. 47 (2012) 278–285. https://doi.org/10.3724/SP.J.1259.2012.00278.

[9] Y. Yoneda, M. Shigeno, T. Kimura, K. Nagao, C. Hotehama, A. Sakuda, M. Tatsumisago, A. Hayashi, Preparation and characterization of hexagonal Li_4GeO_4-based glass-ceramic electrolytes, Solid State Ion. 363 (2021) 115605. https://doi.org/10.1016/j.ssi.2021.115605.

[10] L. Li, T. Meng, J. Wang, B. Mao, J. Huang, M. Cao, Oxygen Vacancies Boosting Lithium-Ion Diffusion Kinetics of Lithium Germanate for High-Performance Lithium Storage, ACS Appl Mater Interfaces. (2021). https://doi.org/10.1021/acsami.1c04200.

[11] L.G. Soltay, G.S. Henderson, Structural differences between lithium silicate and lithium germanate glasses by Raman spectroscopy, Physics and Chemistry of Glasses. 46 (2005) 381–384.

[12] G.S. Henderson, The Germanate Anomaly: What do we know?, J Non Cryst Solids. 353 (2007) 1695–1704. https://doi.org/10.1016/j.jnoncrysol.2007.02.037.

[13] S. Wan, S. Zhang, X. Gong, Y. Zeng, S. Jiang, J. You, Structural investigations on two typical lithium germanate melts by: In situ Raman spectroscopy and density functional theory calculations, CrystEngComm. 22 (2020) 701–707. https://doi.org/10.1039/c9ce01512d.

[14] S. Zhang, S. Wan, Y. Zeng, S. Jiang, X. Gong, J. You, In Situ Raman Spectroscopy and DFT Studies of the Li_2GeO_3 Melt Structure, Inorg Chem. 58 (2019) 5025–5030. https://doi.org/10.1021/acs.inorgchem.9b00051.

[15] O.N. Koroleva, M. v. Shtenberg, T.N. Ivanova, The structure of potassium germanate glasses as revealed by Raman and IR spectroscopy, J Non Cryst Solids. 510 (2019) 143–150. https://doi.org/10.1016/j.jnoncrysol.2019.01.017.

[16] G.S. Henderson, L.G. Soltay, H.M. Wang, Q speciation in alkali germanate glasses, J Non Cryst Solids. 356 (2010) 2480–2485. https://doi.org/10.1016/j.jnoncrysol.2010.03.023.

[17] P. Unifantowicz, S. Vaucher, M. Lewandowska, K.J. Kurzydłowski, Structural changes of silicon upon high-energy milling investigated by Raman spectroscopy, Journal of Physics Condensed Matter. 20 (2008). https://doi.org/10.1088/0953-8984/20/02/025205.

[18] L.G. Soltay, G.S. Henderson, The structure of lithium-containing silicate and germanate glasses, Can Mineral. 43 (2005) 1643–1651. https://doi.org/10.2113/gscanmin.43.5.1643.

[19] X. Zhang, Z. Liu, M. Tanaka, T. Watanabe, Formation mechanism of amorphous silicon nanoparticles with additional counter-flow quenching gas by induction thermal plasma, Chem Eng Sci. 230 (2021) 116217. https://doi.org/10.1016/j.ces.2020.116217.

[20] A. Vorobev, O. Zikanov, P. Mohanty, A co-condensation model for in-flight synthesis of metal-carbide nanoparticles in thermal plasma jet, Journal of Thermal Spray Technology. 17 (2008) 956–965. https://doi.org/10.1007/s11666-008-9240-y.

[21] M. Shigeta, T. Watanabe, Effect of precursor fraction on silicide nanopowder growth under thermal plasma conditions: A computational study, Powder Technol. 288 (2016) 191–201. https://doi.org/10.1016/j.powtec.2015.11.005.

[22] H. Sone, T. Kageyama, M. Tanaka, D. Okamoto, T. Watanabe, Induction thermal plasma synthesis of lithium oxide composite nanoparticles with a spinel structure, Jpn J Appl Phys. 55 (2016). https://doi.org/10.7567/JJAP.55.07LE04.

[23] Speight, James G., Ed. Lange's Handbook of Chemistry. McGraw-Hill Education: New York, USA, 2017.

[24] M. Shigeta, T. Watanabe, Numerical analysis for co-condensation processes in silicide nanoparticle synthesis using induction thermal plasmas at atmospheric pressure conditions, J Mater Res. 20 (2005) 2801–2811. https://doi.org/10.1557/JMR.2005.0351.

[25] Y. Wang, X. Zhang, B.-I. Min, M. Tanaka, T. Watanabe, Synthesis of amorphous Li_3BO_3 nanoparticles as solid electrolyte for all-solid-state battery by induction thermal plasma, J Solid State Chem. (2022) 123775. https://doi.org/10.1016/j.jssc.2022.123775.

[26] J. C. Phillips, Topology of covalent non-crystalline solids I: Short-range order in Chalcogenide alloys, J Non Cryst Solids. 34 (1979) 153–181. https://doi.org/10.1016/0921-4526(95)00390-U.

[27] Prabhat K. Gupta, Rigidity, Connectivity, and Glass-Forming Ability, Journal of the American Ceramic Society. 76 (1993) 1088–1095.

[28] S.R. Elliott, Medium-range structural order in covalent amorphous solids, Nature. 354 (1991) 445–452. https://doi.org/10.1038/354445a0.

[29] K. v. Shanavas, N. Garg, S.M. Sharma, Classical molecular dynamics simulations of behavior of GeO2 under high pressures and at high temperatures, Phys Rev B Condens Matter Mater Phys. 73 (2006) 1–12. https://doi.org/10.1103/PhysRevB.73.094120.

[30] M. Bauchy, M. Micoulaut, M. Celino, S. le Roux, M. Boero, C. Massobrio, Angular rigidity in tetrahedral network glasses with changing composition, Phys Rev B Condens Matter Mater Phys. 84 (2011) 1–9. https://doi.org/10.1103/PhysRevB.84.054201.

[31] S. le Roux, A. Bouzid, M. Boero, C. Massobrio, Structural properties of glassy Ge_2Se_3 from first-principles molecular dynamics, Phys Rev B Condens Matter Mater Phys. 86 (2012). https://doi.org/10.1103/PhysRevB.86.224201.

[32] S. le Roux, P. Jund, Ring statistics analysis of topological networks: New approach and application to amorphous GeS_2 and SiO_2 systems, Comput Mater Sci. 49 (2010) 70–83. https://doi.org/10.1016/j.commatsci.2010.04.023.

[33] M. Micoulaut, A. Kachmar, M. Bauchy, S. le Roux, C. Massobrio, M. Boero, Structure, topology, rings, and vibrational and electronic properties of Ge_xSe_{1-x} glasses across the rigidity transition: A numerical study, Phys Rev B Condens Matter Mater Phys. 88 (2013) 1–23. https://doi.org/10.1103/PhysRevB.88.054203.

[34] S.R. Elliott, Amorphous Materials: Medium-range Order, Encyclopedia of Materials: Science and Technology. (2001) 215–219. https://doi.org/10.1016/b0-08-043152-6/00046-2.

Table 3.1. Experimental conditions for induction thermal plasma system.

Parameter	Condition
Input power [kW]	20
Pressure [kPa]	101.3
Frequency [MHz]	4
Sheath gas rate [L/min]	60 (Ar+O_2)
Inner gas rate [L/min]	5 (Ar)
Carrier gas rate [L/min]	3, 4.5, 6 (Ar)
Quenching gas rate [L/min]	0, 10, 20 (Ar)
Feed rate [mg/min]	300
Ar/O_2 molar ratio [-]	59:1, 57.5:2.5, 55:5
L/Ge molar ratio [-]	4:1, 4:1.25, 4:1.5, 4.25:1, 4.5:1

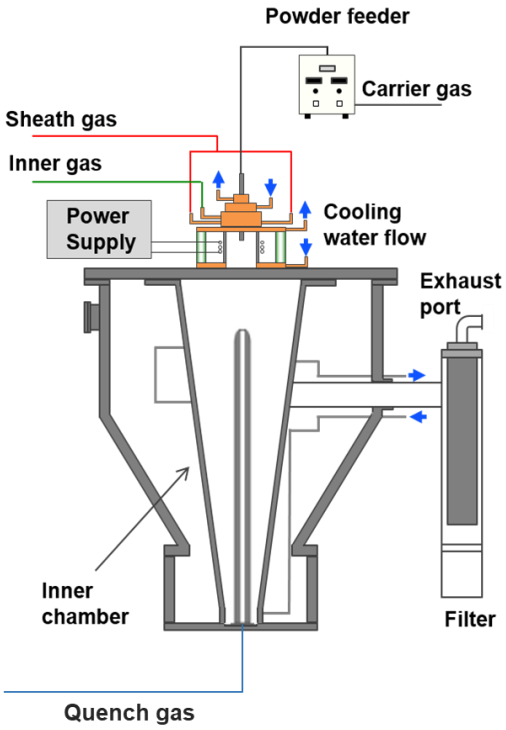

Fig. 3.1. Schematic diagram of amorphous Li_4GeO_4 synthesized by induction thermal plasma.

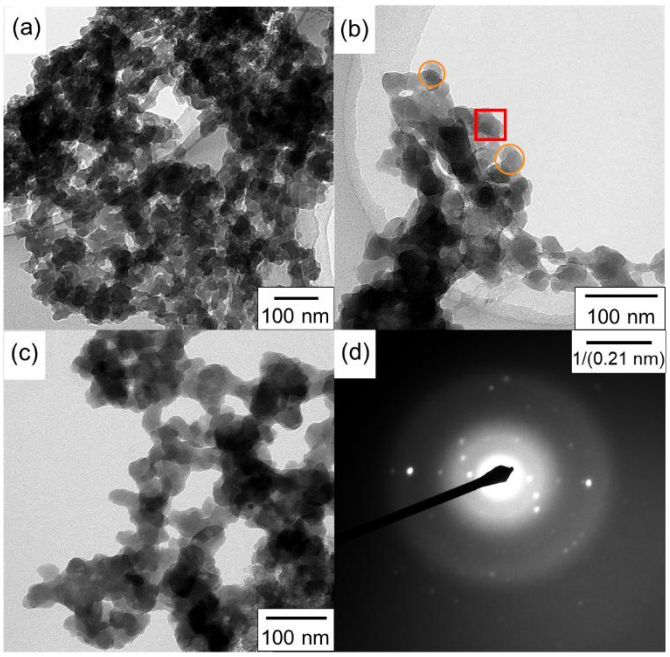

Fig. 3.2. TEM images of products synthesized by (a) 4:1, (b) 4:1.25, (c) 4:1.5 Li/Ge molar ratio. The red square is the focus of the electron beam on product. The corresponding diffraction pattern is shown in (d).

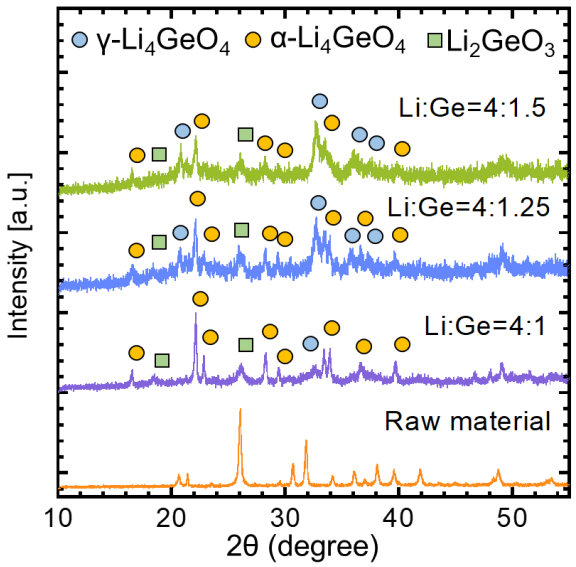

Fig. 3.3. XRD spectra of products synthesized by 4:1, 4:1.25, 4:1.5 Li/Ge molar ratio. Blue round, yellow round, green square represents γ-Li_4GeO_4, α-Li_4GeO_4, and Li_2GeO_3, respectively.

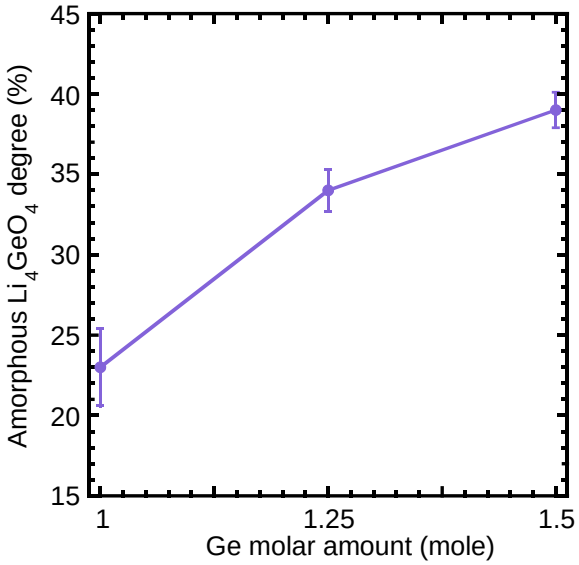

Fig. 3.4 Estimated amorphous Li_4GeO_4 degree of product synthesized by different Li/Ge molar ratios. The error bars represent the standard errors of the corresponding average.

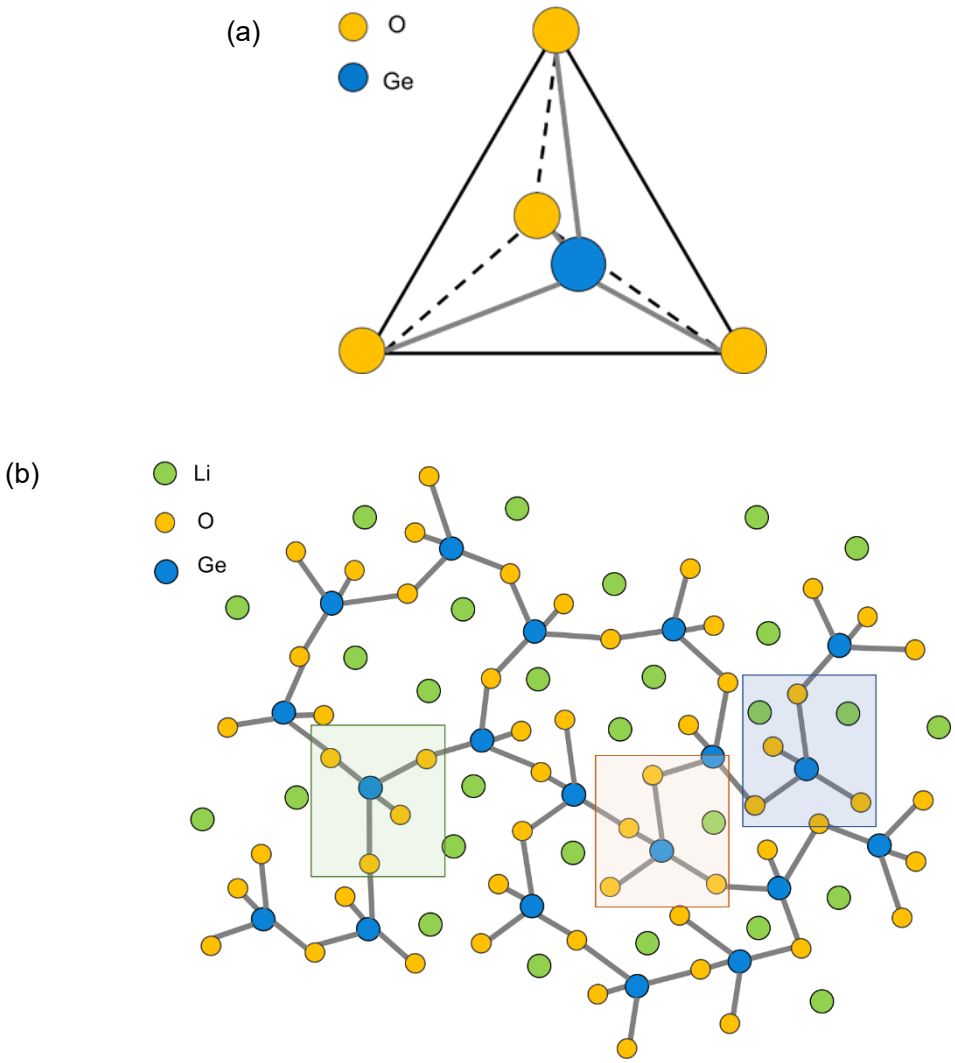

Fig. 3.5. Schematic diagram of (a) [GeO_4] tetrahedron, (b) Q^n species in Li-Ge-O system. The Q^2, Q^{32}, and Q^{33} is illustrated by blue, green, and orange rectangle, respectively.

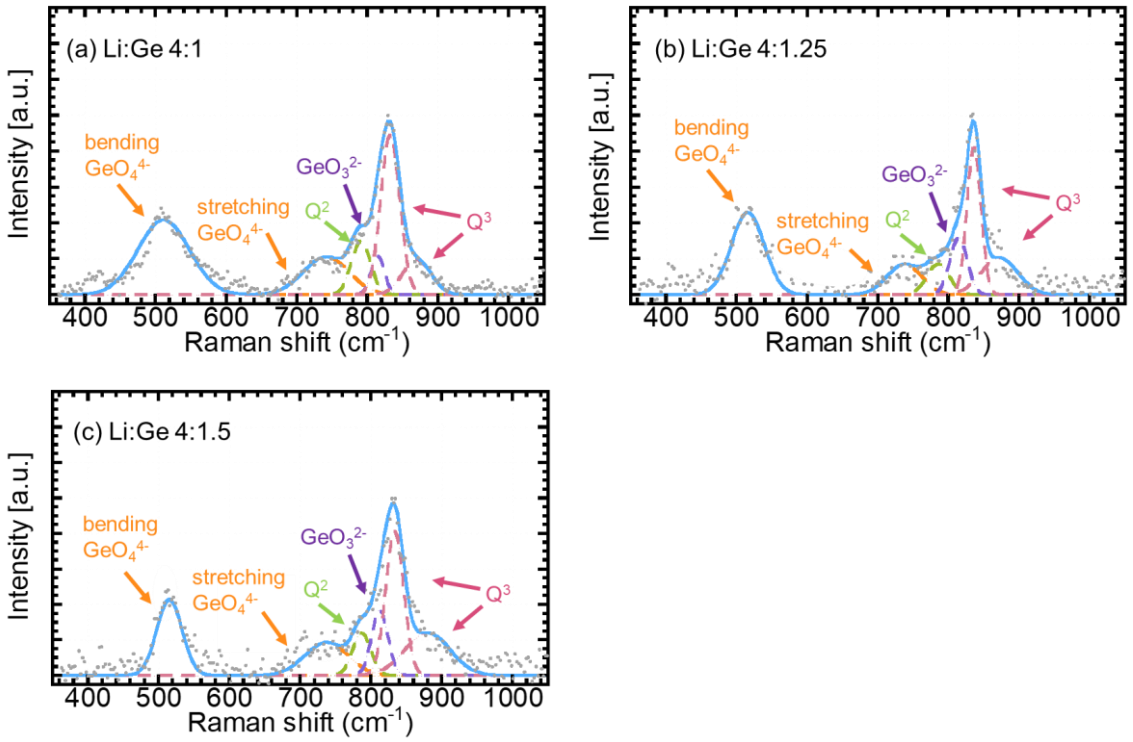

Fig. 3.6. Raman spectra of products synthesized by different Ge contents. (a) 4:1, (b) 4:1.25, (c) 4:1.5. Gray dots line is the experimental results, the blue line is the cumulative fitting.

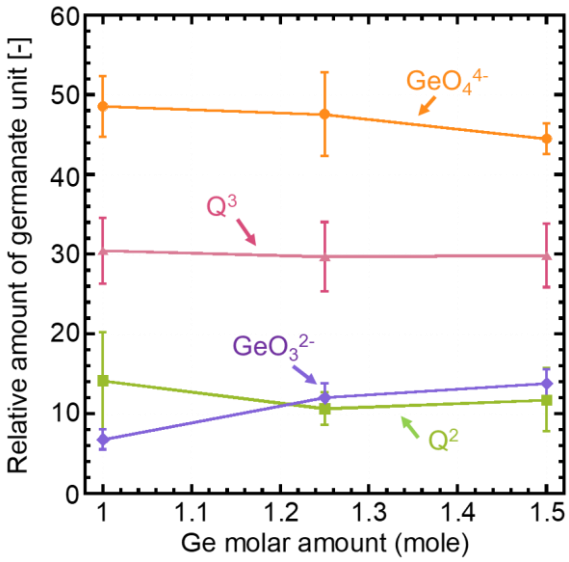

Fig. 3.7. Relative amount of different germanate units of products synthesized by different Ge contents. The error bars represent the standard errors of the corresponding average.

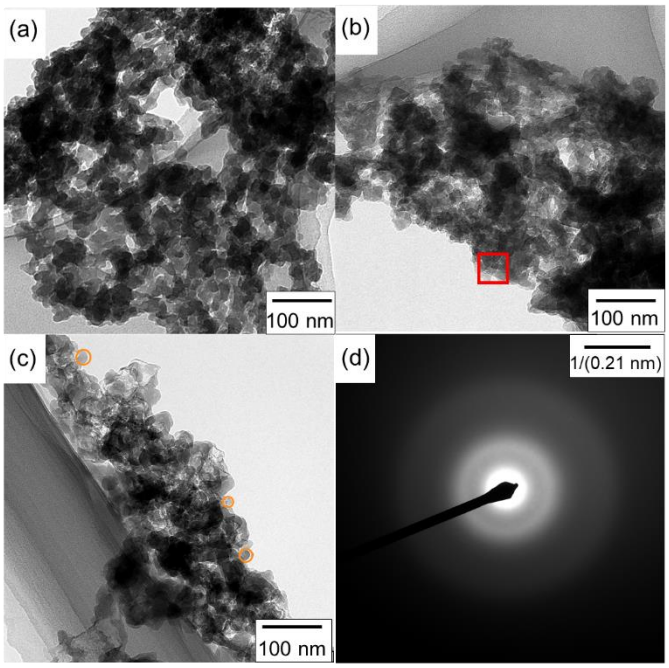

Fig. 3.8. TEM images of products synthesized by (a) 0 L/min, (b) 10 L/min, (c) 20 L/min Ar quenching gas. The red square is the focus of the electron beam on product. The corresponding diffraction pattern is shown in (d).

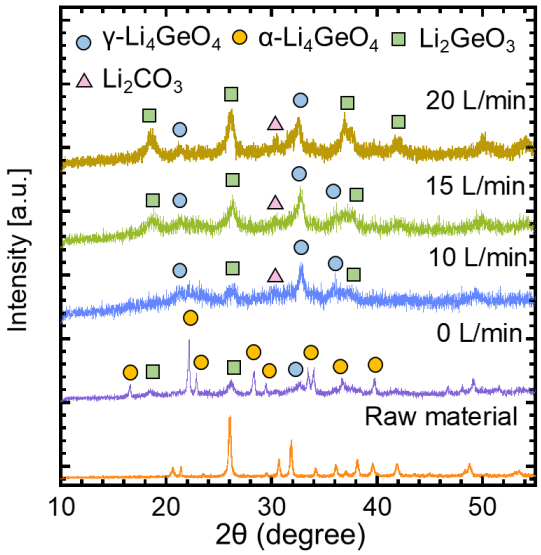

Fig. 3.9. XRD spectra of products synthesized by different quenching gas flow rates. Blue round, yellow round, green square and pink triangle represents γ-Li_4GeO_4, α-Li_4GeO_4, Li_2GeO_3 and Li_2CO_3, respectively.

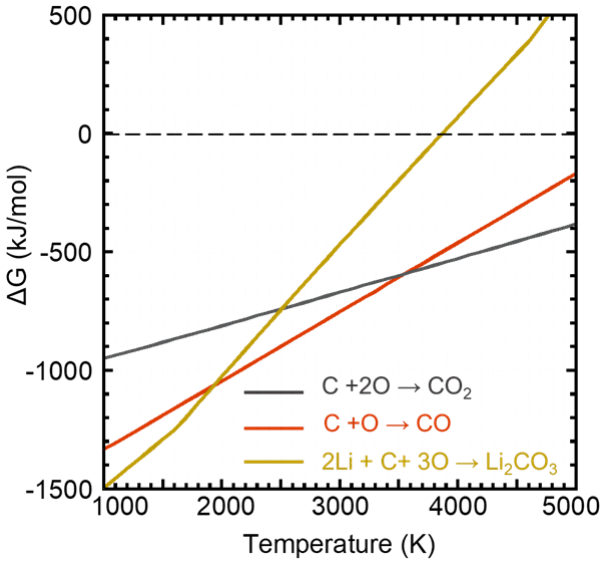

Fig. 3.10. Gibbs energy change of Li_2CO_3, CO_2 and CO with temperature region of 1000-5000 K.

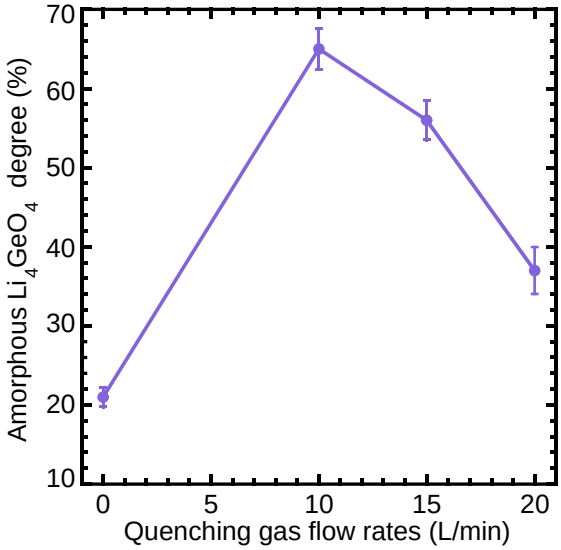

Fig. 3.11. Estimated amorphous Li_4GeO_4 degree of product synthesized by different quenching gas flow rates. The error bars represent the standard errors of the corresponding average.

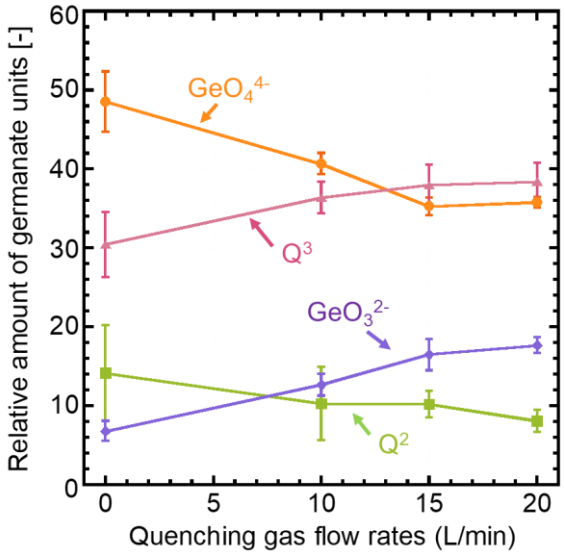

Fig. 3.12. Relative amount of different germanate units of products synthesized by different quenching gas flow rates. The error bar represents the standard errors of the corresponding average.

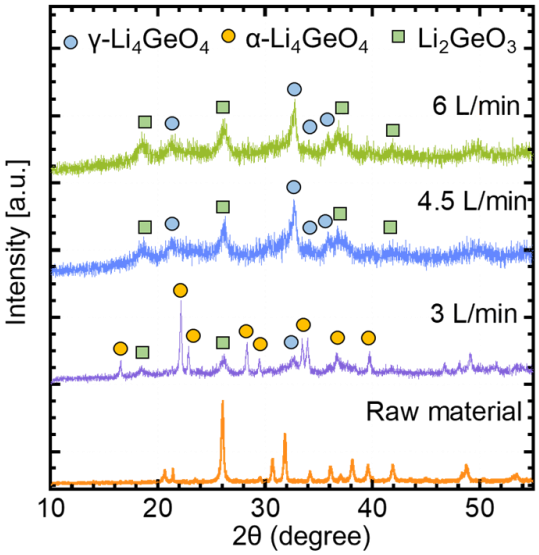

Fig. 3.13. XRD spectra of products synthesized by different carrier gas flow rates. Blue round, yellow round, and green square represents γ-Li_4GeO_4, α-Li_4GeO_4, and Li_2GeO_3, respectively.

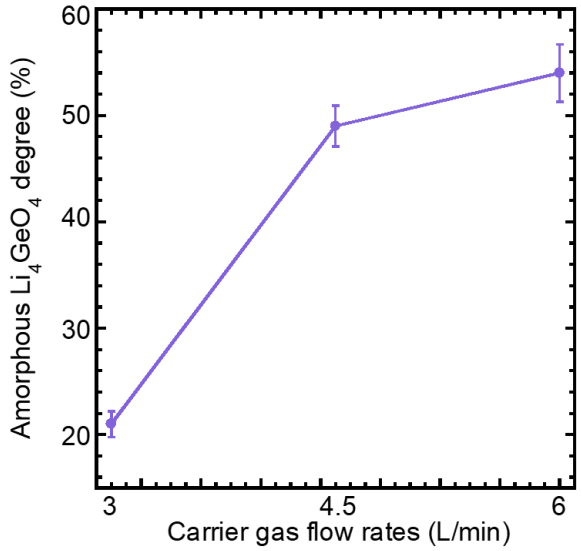

Fig. 3.14. Estimated amorphous Li_4GeO_4 degree of product synthesized by different carrier gas flow rates. The error bars represent the standard errors of the corresponding average.

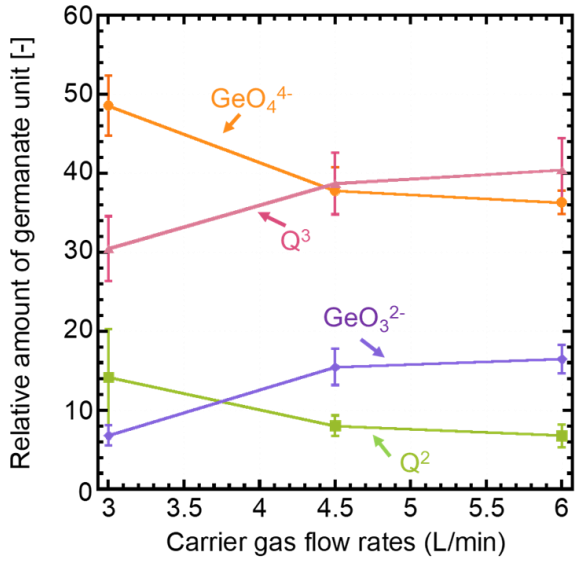

Fig. 3.15. Relative amount of different germanate units of products synthesized by different carrier gas flow rates. The error bar represents the standard errors of the corresponding average.

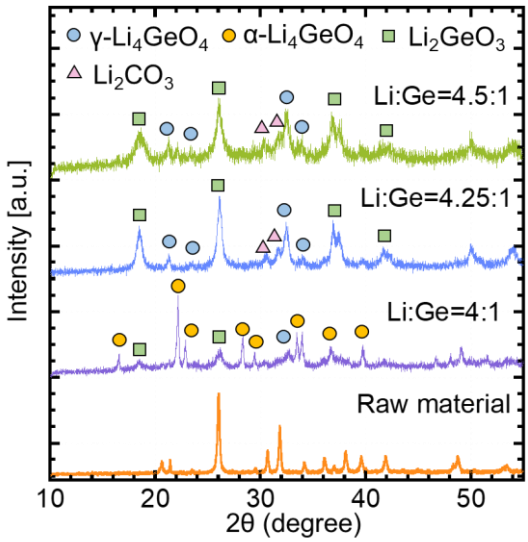

Fig. 3.16. XRD spectra of products synthesized by 4:1, 4.25:1, 4.5:1 Li/Ge molar ratio. Blue round, yellow round, green square and pink triangle represents γ-Li_4GeO_4, α-Li_4GeO_4, Li_2GeO_3, and Li_2CO_3, respectively.

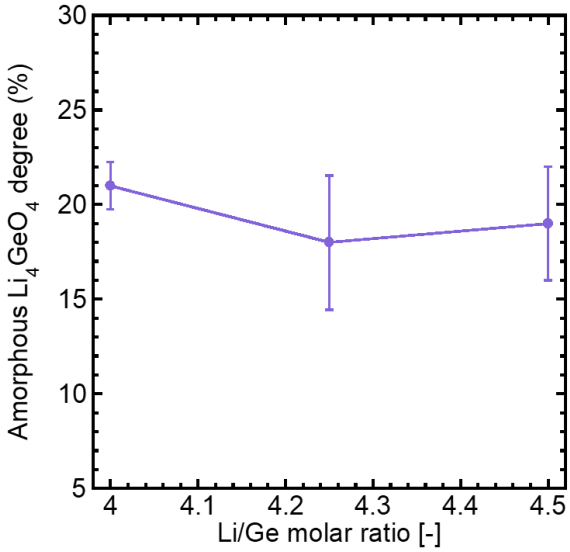

Fig. 3.17. Estimated amorphous Li_4GeO_4 degree of product synthesized by different Li contents. The error bars represent the standard errors of the corresponding average.

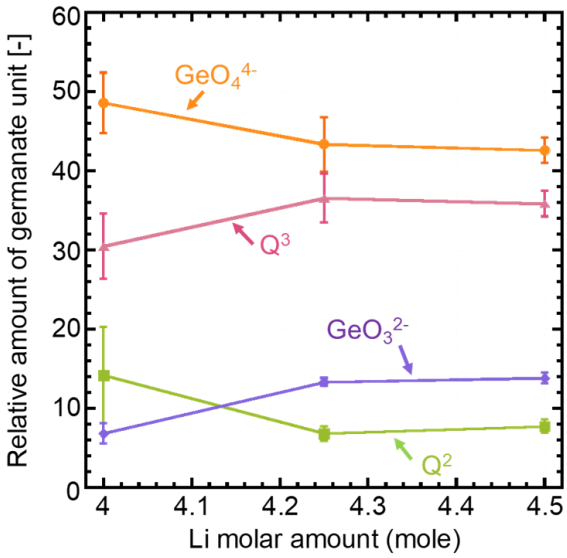

Fig. 3.18. Relative amount of different germanate units of products synthesized by different Li contents. The error bar represents the standard errors of the corresponding average.

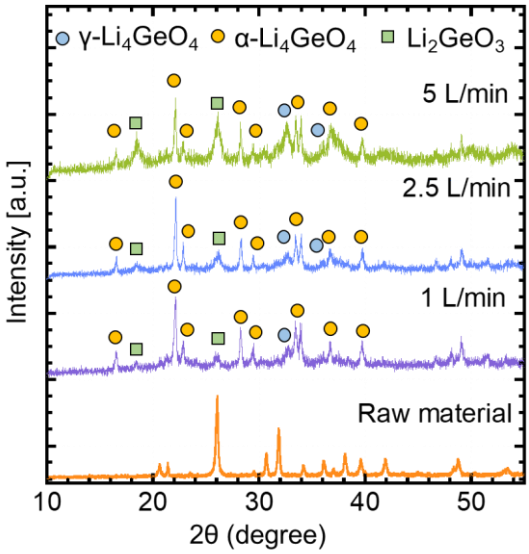

Fig. 3.19. XRD spectra of products synthesized by different O_2 flow rates. Blue round, yellow round, and green square represents γ-Li_4GeO_4, α-Li_4GeO_4, and Li_2GeO_3, respectively.

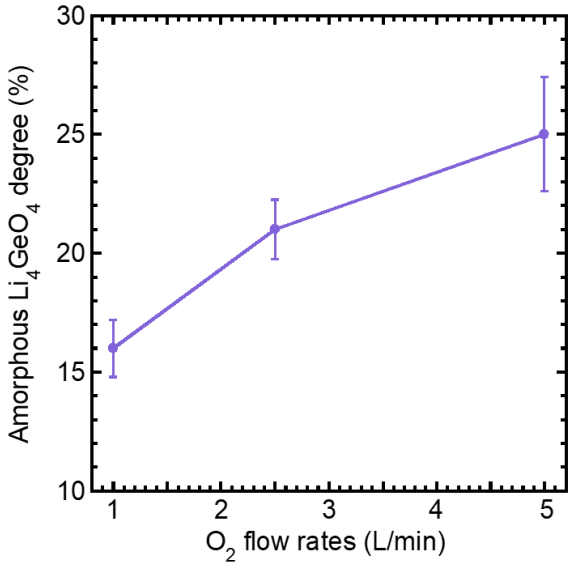

Fig. 3.20. Estimated amorphous Li_4GeO_4 degree of product synthesized by different O_2 flow rates. The error bars represent the standard errors of the corresponding average.

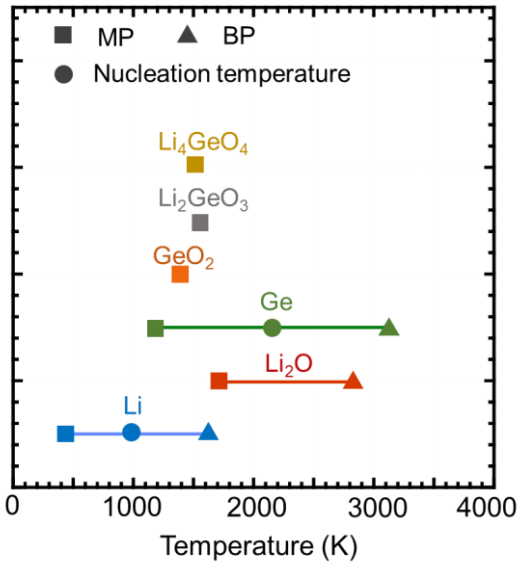

Fig. 3.21. The melting, boiling, and nucleation temperature of Ge, Li, and oxides.

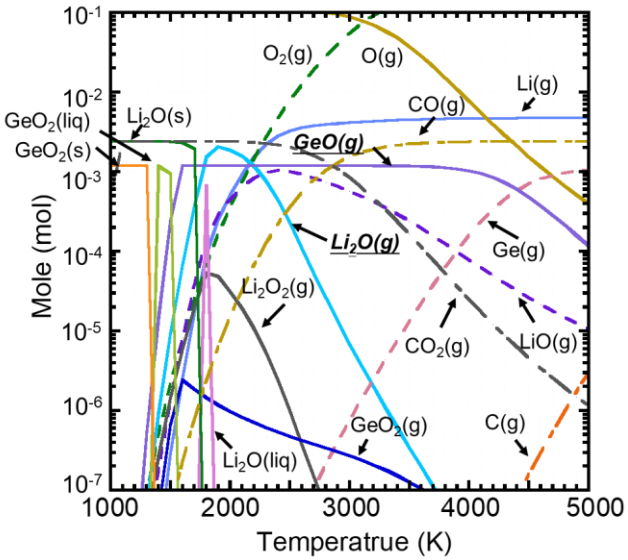

Fig. 3.22. Thermal equilibrium of the Li-Ge-O system. Feeding rate is 300 mg/min with Li/Ge molar ratio 4/1, Ar/O_2 is 57.5/2.5.

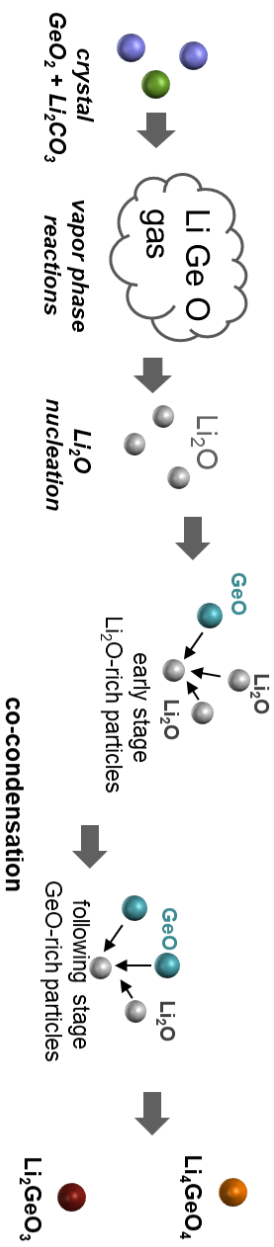

Fig. 3.23. Formation mechanism of Li-Ge-O nanoparticles by induction thermal plasma.

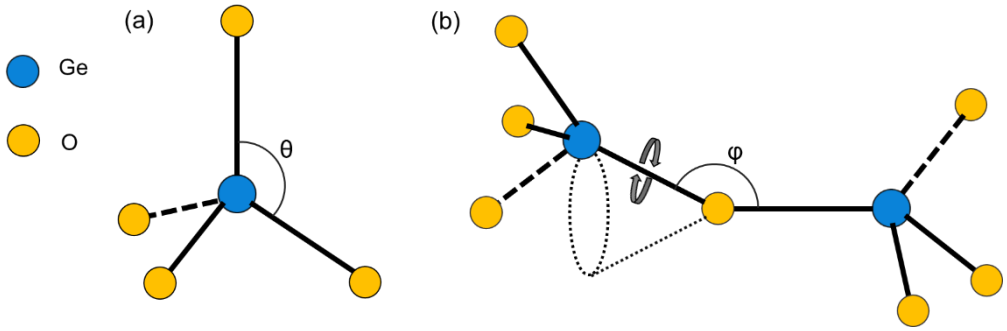

Fig. 3.24. Illustrations of short-range order and intermediate-range order in Li_4GeO_4. (a). Short-range order is defined in terms of 4-coordination tetrahedron and θ is the O-Ge-O angle; (b). Intermediate-range order is defined in terms of the connection of tetrahedrons and φ is the Ge-O-Ge angle.

4. Synthesis of Amorphous Li_5AlO_4 Nanoparticles

Amorphous Li_5AlO_4 has a high ion conductivity and low electron conductivity at room temperature, these advantages satisfy the solid electrolyte requirements [1,2]. The high O/Al value of Li_5AlO_4 allows Al to function as the network former, although Al is a typical glass intermediate instead of the former. [3,4]. In addition, decreasing particle size to the nanoscale can provide a larger connection area between electrode and electrolyte. [5]. Hence, amorphous Li_5AlO_4 nanoparticles were selected as a target material.

This chapter focuses on the synthesis of amorphous Li_5AlO_4 nanoparticles by induction thermal plasma with different Ar quenching gas flow rates and Li/Al molar ratios. The Li content effect, quenching rate effect and formation mechanism were investigated based on thermodynamic analysis and experiment results.

4.1. Experiment

4.1.1 Experiment Configuration and Procedure

The experiment device consists of power supply, powder feeder, plasma torch, reaction chamber cooled by water, quenching tube and product

ion filter, the schematic illustration is shown in **Fig. 4.1**. Quench tube was placed 15 cm below plasma torch. Quenching gas was injected from bottom to offer a sharper temperature gradient. The mixture of Ar and O_2 with a molar ratio 57.5:2.5 was used as sheath gas with a total flow rate of 60 L/min. Raw material with feeding rate of 300 mg/min was injected into plasma by Ar. The experiment conditions are summarized in **Table. 4.1**.

Raw material consists of Li_2CO_3 (purity 99%, Honjo Chemical Corporation) and α-Al_2O_3 (purity 99.9%, Kojundo Chemical Laboratory). No quenching gas injection in different Li/Al molar ratios experiments. The Li/Al molar ratio was fixed at 5:1 in different quenching rates experiments.

4.1.2 Analysis Method

The phase identification of prepared nanoparticles was detected by X-ray diffraction (XRD, Rigaku Multifle) with a Cu Kα source (λ = 0.1541 nm). The continue scan was conducted in a 2θ range of 10°-90° at a scan speed of 1°/min. Aluminate unit structure was investigated by Raman spectrometer (Raman, LabRAM ARAMIS), the laser source wavelength fixed at 532 nm. The morphology of prepared nanoparticles was observed by transmission electron microscopy with an accelerating voltage of 200 kV (TEM, JEOL JEM-2100HCKM). There were three software, *JAED* 6.5 (Material Data, USA), *Image J* (National Institutes of Health, USA), and *Factsage* 7.2 (Centre for Research in Computational Thermochemistry, Canada; GTT-Technology, Germany) were used to estimate amorphous degree, diameter distribution of products and thermodynamic composition during plasma process, respectively.

4.2. Experiment Results

4.2.1 Effect of Quenching Gas

Figure 4.2 shows the TEM images and diffraction pattern images of nanoparticles synthesized by different quenching gas flow rates. The focus of electron beam in product is depicted as red square in **Fig. 4.2 (c)**, corresponding diffraction pattern image is shown in **Fig. 4.2 (d)**. There are no regular diffraction spots and rings in **Fig. 4.2 (d)**, indicating the product exists as amorphous structure. The nanoparticles synthesized without quenching gas present spherical morphology which is indexed by the orange circle in **Fig. 4.2 (a)**. Diameter distribution was estimated by *Image J*. More than 200 different particles were countered to obtain results based on TEM images, the estimated result is presented in **Fig. 4.3**. The diameter of nanoparticles ranges from several nanometers to tens of nanometers with an average diameter of 15 nm.

Agglomerates rather than isolated spherical particles are observed in the 10 L/min and 20 L/min quenching gas cases. Spherical particles are produced at high temperature due to coalescence-dominant, while agglomerate occurs at low temperature caused by the dominant coagulation [6,7]. The temperature gradient is sharpened by quenching gas injection, and results in particles growing at lower temperature. Thus, agglomerates are observed in the quenching gas case.

Phase identification of products was investigated by XRD, and the XRD spectra are shown in **Fig. 4.4**. The Li_2CO_3 and high temperature phase $LiAlO_2$ (γ-$LiAlO_2$) are detected as by-products in crystalline parts, meanwhile, amorphous peak emerges in XRD spectra. The phase transition can be prevented by the rapid quenching rate of thermal plasma, the γ-$LiAlO_2$ is preserved in products. Since the total decomposition of raw material, the C vapor reacts with O vapor to form CO_2 and CO vapor before nucleation. The thermodynamic equilibrium composition result is presented in section 4.3.1. Synthesized CO_2 vapor exhaust from the system by vacuum pump, and does not participate in nanoparticle synthesis process [8]. The Li_2CO_3 is considered synthesized by CO_2 in atmosphere with unreacted lithium or lithium oxide after plasma process [9]. The crystal peak intensity becomes weak with quenching gas increase, simultaneously, amorphous peak becomes obvious. The XRD spectra indicate that more amorphous nanoparticles were obtained at high quenching gas flow rate.

The amorphous degree of product is estimated by *JADE* 6.5 based on XRD spectra using **Eqs. (2.1) - (2.2)**. The black line in **Figure 4.5** is the estimated amorphous degree of products synthesized by different quenching gas flow rates. The amorphous degree is around 50% without quenching gas injection, increasing to around 82% and 90% after 10 L/min and 20 L/min quenching gas injection, respectively.

The aluminate units and connectivity of these units play significant roles in the amorphous structure [10]. Octahedron [AlO_6] and tetrahedron [AlO_4] are the two main structure units for lithium aluminate, corresponding illustration is shown in **Fig. 4.6**. The Li_5AlO_4 is built by [AlO_4] tetrahedrons [11,12]. Transformation from [AlO_6] to [AlO_4] is influenced by temperature distribution and O/Al molar ratio [13]. Raman spectrometer was conducted in order to understand the unit structure and distribution in products, further understand the effect of different experiment conditions.

Figure 4.7 (a) - (c) are the Raman spectra of products synthesized by different quenching gas flow rates. Gray dots line and blue line represent experiment spectrum and cumulative fitting, respectively. There are six characteristic peaks identified after fitting by Gaussian function in products. The peak located around 480-500 cm^{-1} belongs to AlO_2^- [14]. Peaks sited to around 500-

520 cm^{-1}, 600 cm^{-1}, and 730-800 cm^{-1} are indexed to $[AlO_4]$ with bridge oxygens (BOs), $[AlO_6]$ and $[AlO_4]$ with non-bridge oxygens (NBOs), respectively [15,16]. The CO_3^{2-}peak is placed around 1100 cm^{-1} [17]. Because no peaks belonged to $[AlO_6]$ in XRD spectra, meanwhile, the $[AlO_6]$ is also detected in lithium aluminate glass [16,18]. The $[AlO_6]$ is considered to exist as amorphous in this experiment.

Figure 4.8 is the estimated relative amounts of different units for products synthesized by different quenching gas flow rates. This result is obtained based on the following assumption. The total number of Raman scattering gives rise to the area under the peaks, each Gaussian peak area should be related to the amount of corresponding structural unit [19,20]. The estimated result demonstrates that the by-products Li_2CO_3 and γ-$LiAlO_2$ decrease obviously after quenching gas injection. Percentage of CO_3^{2-} and AlO_2^- continually decrease to around 16% and 10% with flow rate increase to 20 L/min, respectively. Simultaneously, the percentage of $[AlO_4]$ with BOs also reduces to 23% in 20 L/min case. An opposite tendency is observed in the percentage of $[AlO_6]$ and $[AlO_4]$ with NBOs. These trends indicate aluminate transformation from $[AlO_6]$ to $[AlO_4]$ is impaired by quenching gas and fewer BO bonds exist in products. Above phenomena are related to condensation rate of different species during plasma process. The enhanced quenching gas flow rate allows more Li_2O to take part in reactions, the BO bonds are destroyed by these increased Li_2O and more NBOs are formed. The transformation time from $[AlO_6]$ to $[AlO_4]$ is shortened by enhanced quenching rate, and more $[AlO_6]$ are detected in products. Details will be discussed in the section 4.3.2.

The estimated amorphous Li_5AlO_4 degree can be obtained after understanding the relative amount of each unit. Four compounds are known in Li-Al-O system: $LiAl_5O_8$, $Li_2Al_4O_7$, $LiAlO_2$, and Li_5AlO_4 [21]. The first two compounds contain $[AlO_6]$ octahedrons, while the aluminate unit of the latter two is only $[AlO_4]$ tetrahedron [21]. Network supported by tetrahedrons more easily forms amorphous structure compared to octahedrons according to Zachariasen's rule [10]. Thus, the $LiAl_5O_8$ and $Li_2Al_4O_7$ prefer to form crystalline, while $LiAlO_2$ and Li_5AlO_4 prefer to form amorphous at the same quenching rate. The higher coordination number of Al results in harder amorphous formation [22]. The $LiAlO_2$ melt possesses higher Al coordination number compared

to Li_5AlO_4, indicating Li_5AlO_4 more easily acquires amorphous structure than $LiAlO_2$ [22]. Thus, all Li_5AlO_4 exists as amorphous while part of $LiAlO_2$ exists as amorphous.

The XRD spectra indicate that only γ-$LiAlO_2$ peaks are detected for lithium aluminate in crystal part, that is, no $LiAl_5O_8$ and $Li_2Al_4O_7$ are synthesized during the plasma process. Composition of products can be identified based on above description. Amorphous part contains Li_5AlO_4 and parts of $LiAlO_2$, crystalline part contains Li_2CO_3 and parts of $LiAlO_2$. Amorphous Li_5AlO_4 degree is estimated according to following equations:

$$W_a(Li_5AlO_4) = W_{amorphous} - W_a(LiAlO_2) \quad (4.1)$$

$$W_a(LiAlO_2) = W(LiAlO_2) - [DOC - W(Li_2CO_3)] \quad (4.2)$$

where $W_a(Li_5AlO_4)$ and $W_a(LiAlO_2)$ represent relative amount of amorphous Li_5AlO_4 and $LiAlO_2$, respectively. $W(LiAlO_2)$ and $W(Li_2CO_3)$ refer to relative amounts of $LiAlO_2$ and Li_2CO_3. The red line in **Fig. 4.5** shows the estimated amorphous Li_5AlO_4 degree of products synthesized by different quenching gas flow rates. Enhanced amorphous Li_5AlO_4 degree is achieved in high quenching rate condition, the value increases to around 82% at 20 L/min of quenching gas.

The above results indicate that high quenching rate benefits amorphous Li_5AlO_4 synthesis at Li/Al molar ratio 5:1. Meanwhile, the high quenching rate attributes to by-product reduction. The reason for this phenomenon is related to saturation ratio of different vapor phases, more details will be discussed in next section.

4.2.2 Effect of Li Content in Raw Material

The spherical particles are observed in products synthesized by different Li/Al molar ratios, the TEM images are shown in **Fig. 4.9**. The nanoparticles indexed by orange circles display a diameter of around 20 nm. Some particles indexed by blue square even have a very tiny diameter blew than 10 nm. Since the nucleation temperature is around 3000 K in Li-Al-O system, which allows the particles can grow in high temperature region. The nucleation temperature is discussed on the section 4.3.1. The coalescence among particles is more dominant than coagulate as previously discussed, leading to the formation of spherical particles.

The main products in the crystal part were identified as Li_2CO_3 and γ-$LiAlO_2$ according to the

XRD spectra, and the XRD spectra are shown in **Fig. 4.10**. Peak intensity of Li_2CO_3 and γ-$LiAlO_2$ becomes weaker with the Li/Al molar ratio value increasing, which reveals more amorphous were synthesized after Li/Al molar ratio rising. Amorphous degree of products was estimated based on **Eqs. (2.1) - (2.2)**, and the estimated results are presented in **Fig. 4.11**. The result indicates that the enhanced amorphous degree of products was obtained by the high Li content in raw material.

Aluminate unit distribution in products was also investigated by Raman spectrometer. Same characteristic peaks were detected in quenching rate effect experiments, the product consists of AlO_2^-, [AlO_4] with BOs, [AlO_6], [AlO_4] with NBOs, and CO_3^{2-}. **Figure 4.12** is the relative amounts of different units in products. Percentage of AlO_2^-, CO_3^{2-}, and [AlO_4] with BOs show a downtrend, while the percentage of [AlO_6] and [AlO_4] with NBOs have an opposite tendency. Estimated amorphous Li_5AlO_4 degree is presented in **Fig. 4.11** as the red line. Amorphous Li_5AlO_4 degree enhances to around 61% in Li/Al molar ratio of 5.75 indicating that amorphous Li_5AlO_4 nanoparticles prefer to synthesize in a condition that Li molar amount excesses of its stoichiometric ratio.

The above results demonstrate that excessive Li content in raw material promotes amorphous Li_5AlO_4 nanoparticles synthesis, simultaneously, preventing by-product generation. Details will be discussed in the next section.

4.3. Discussion

4.3.1 Formation Mechanism of Lithium Aluminate Nanoparticles

The structure and the chemical composition of products are closely related to chemical reactions and particle growth during plasma process. Investigation of formation mechanism is a powerful method to understand experiment condition effect. The formation mechanism of nanoparticles synthesized by induction thermal plasma has already been investigated by experiments and simulations [23,24]. Synthesis of nanoparticles by induction thermal plasma contains three main process including homogeneous nucleation, heterogeneous condensation, and coagulation.

Nucleation temperature of each species in Li-Al-O system is investigated in order to identify

the nucleation phase. There is no solid interface that exists during plasma process, the nucleation is considered homogeneous. Homogeneous nucleation temperature of elementary substance is estimated by **Eqs. (2.3) - (2.6)**.

The nucleation temperature of Al and Li is obtained based on above equations with 300 mg/min feeding rate. **Figure 4.13** presents the nucleation temperature, melting point, and boiling point of the main composition in Li-Al-O system. The melting point and boiling point are obtained from Lang's Handbook of Chemistry [25]. Nucleation temperature of aluminum and lithium are 1056 K and 1616 K, respectively. Melting point is regarded as the nucleation temperature of oxides because of the similar value of two temperature and the thermal data limitation of oxides [26]. The highest nucleation temperature is occupied by Al_2O_3 according to **Fig. 4.13**, indicating that Al_2O_3 is the nucleation phase in Li-Al-O system. In addition, homogeneous nucleation occurs when vapor achieves supersaturation. The nucleation phase is also affected by the partial pressure of each vapor during plasma process besides nucleation temperature.

Thermodynamic equilibrium composition of Li-Al-O system during the plasma process was investigated in order to understand partial vapor pressure. **Figure 4.14** is the estimated result of thermodynamic equilibrium composition of Li-Al-O system with following experiment conditions. The feeding rate and value of Li/Al are 300 mg/min and 5, sheath gas is the mixture of Ar and O_2 with molar ratio of 57.5:2.5. **Figure 4.14** demonstrates aluminum exists as AlO vapor and AlO_2 vapor in high temperature region. The Al_2O_3 is synthesized by AlO and AlO_2 vapor when temperature decreases to around 3000 K, the reaction is presented in **Eq. 4.3**. Simultaneously, the Al_2O_3 vapor achieves supersaturation and starts to nucleate. Lithium exists as Li vapor and LiO vapor at high temperature. The nucleation phase can be identified as Al_2O_3 around 3000 K combining the nucleation temperature with equilibrium composition.

$$AlO(g)+AlO_2(g)\rightarrow Al_2O_3(l) \quad (4.3)$$

The formation mechanism of lithium aluminate is put forward based on the above discussion, the illustration is presented in **Fig. 4.15**. Raw material consisting of Li_2CO_3 and α-Al_2O_3 is injected into plasma and decomposes immediately. Then the vapor phase reactions start among different vapors to form AlO, AlO_2, and LiO vapor. Particles collide with each other and flow to the

downstream region with lower temperature. The AlO reacts with AlO_2 to synthesize Al_2O_3 when temperature declines to around 3000 K, simultaneously, the Al_2O_3 achieves supersaturation and starts to nucleate. Heterogeneous co-condensation starts as soon as nuclei occur. Vapor of Li and LiO condense on the nuclei to synthesize into lithium aluminate during this process.

Various lithium aluminate nanoparticles are mainly synthesized at different stages of condensation due to the discrepancy in saturation ratios [27]. The Al-rich particle $LiAlO_2$ is mainly synthesized at early-stage of condensation owing to the higher saturation ratio of Al_2O_3. The Li and LiO condensation become dominant gradually with consumption of Al_2O_3 and temperature decrease. The Li and LiO vapor start to more rapidly condense on the Al-rich particle $LiAlO_2$ than Al_2O_3 vapor to form Li-rich particle Li_5AlO_4. Namely, the Li-rich particle Li_5AlO_4 is mainly synthesized at following-stage of condensation. **Equations 4.4** and **4.5** display the reactions for early- and following- stage of condensation, respectively. The condensation is terminated by solidification of all condensation phases in Li-Al-O system. Nanoparticles grow continuously by coagulation.

$$Al_2O_3(l)+LiO(g)+Li(g) \rightarrow 2LiAlO_2(l) \quad (4.4)$$

$$LiAlO_2(l)+2LiO(g)+2Li(g) \rightarrow 2Li_5AlO_2(l) \quad (4.5)$$

The rapid quenching rate prevents particle orderly grow during the plasma process, and the amorphous structure is achieved in products. Those unreacted LiO and Li vapor are oxidized into Li_2O and react with H_2O and CO_2 in atmosphere during collection, then form into by-product Li_2CO_3.

4.3.2 Transformation Between [AlO_6] and [AlO_4]

Octahedron [AlO_6] and tetrahedron [AlO_4] are two main aluminate units for lithium aluminate, they affect crystalline and amorphous structure of products. Structure of aluminate unit relates to O/Al molar ratio and temperature distribution closely [28]. The value of O/Al molar ratio is less than 2 in system, namely, oxygen is deficiency, the aluminate unit prefers to form face- or edge-shared [AlO_6] at a same temperature distribution [4,29]. These connection conditions result in the low flexibility of structure, further tending to order structure formation. The [AlO_6] transforms to

[AlO_4] with O/Al molar ratio increasing. The lower limit of O/Al is 2 for aluminate lithium consisted by corner-shared [AlO_4]. The higher flexibility and lower Al coordination number lead to the network consisting of [AlO_4] tetrahedron easily achieving disorder, further acquiring amorphous structure under rapid quenching rate. Therefore, promotion of [AlO_4] formation is beneficial to amorphous nanoparticle synthesis in Li-Al-O system.

Nucleation phase is Al_2O_3 in this experiment, the [AlO_6] is formed firstly due to the oxygen deficiency. The O/Al molar ratio increases with the LiO condensing on Al_2O_3 nuclei, allowing the [AlO_6] transforms to [AlO_4]. **Figure 4. 16** displays the aluminate transformation process with O/Al molar ratio increase in amorphous lithium aluminate. The aluminate experiences a transformation from [AlO_6] to [AlO_4] at initial to form $LiAlO_2$, then Li_5AlO_4 is synthesized by continuously LiO condensation. Promotion of LiO vapor condensation conducive to [AlO_4] and Li_5AlO_4 formation during condensation process. The product structure would possess higher flexibility owing to enhanced corner-shared [AlO_4] percentage and preserve the disorder after plasma process. Meanwhile, these more synthesized Li_5AlO_4 achieve the amorphous structure under the rapid quenching rate of thermal plasma. Improved LiO condensation can be achieved by high Li/Al molar ratio because of higher LiO saturation ratio. Thus, enhanced amorphous degree of products and Li_5AlO_4 are obtained in high Li/Al molar ratio cases.

Quenching gas injection sharps the temperature gradient, the quenching rate increases from 3.2×10^4 K/s to 1.5×10^5 K/s with quenching gas flow rate increasing from 0 L/min to 20 L/min. This steeper temperature gradient can advance and promote the following-stage of condensation. Because the duration of early-stage condensation would be suppressed by steeper temperature gradient, simultaneously, the LiO more early reaches supersaturation state and more LiO participate in reaction. Above phenomenon facilitates the Li-rich Li_5AlO_4 synthesis and reduces the Li_2CO_3 and $LiAlO_2$ formation. However, the steeper temperature gradient also shortens the transformation time from [AlO_6] to [AlO_4]. These untransformed [AlO_6] exist as amorphous in products due to the enhanced quenching rate. Therefore, more amorphous Li_5AlO_4 nanoparticles are obtained at higher flow rate of quenching gas, while, increased [AlO_6] is also detected.

Enhanced amorphous Li_5AlO_4 degree is achieved by high Li/Al molar ratio and quenching rate.

Because the improved LiO condensation contributes to [AlO_4] and Li_5AlO_4 formation.

4.4. Conclusion

Amorphous Li_5AlO_4 nanoparticles were synthesized by induction thermal plasma successfully. Formation mechanism, quenching gas effect and Li content effect were investigated based on experiment results and thermodynamic analysis.

Enhanced amorphous Li_5AlO_4 degree was obtained at high quenching gas flow rate and Li/Al molar ratio. The LiO-dominant condensation is promoted by the higher quenching gas flow rate and Li/Al molar ratio. This situation benefits transformation of aluminate from [AlO_6] octahedron to [AlO_4] tetrahedron and synthesis of Li-rich nanoparticle Li_5AlO_4. Enhanced [AlO_4] percentage allows product structure to own higher flexibility and more easily achieve amorphous structure after plasma process. Promoted Li_5AlO_4 achieves amorphous structure under the rapid quenching rate. While the excessive quenching gas flow rate shortens transformation time resulting in increased [AlO_6] existing in products.

Reference:

[1] K.N. A.M. Glass, Lithium ion conduction in rapidly quenched Li_2O-Al_2O_3 Li_2O-Ga_2O_3 and Li_2O-Bi_2O_3 glasses, Functional Oxides. 3756 (1980) 119–202. https://doi.org/10.1002/9780470686072.ch3.

[2] K. Nassau, M. Grasso, A.M. Glass, Quenched glasses in the systems of Li_2O with Al_2O_3, Ga_2O_3 and Bi_2O_3, J Non Cryst Solids. 34 (1979) 425–436. https://doi.org/10.1016/0022-3093(79)90028-0.

[3] S. Jahn, Atomic structure and transport properties of MgO-Al_2O_3 melts: A molecular dynamics simulation study, American Mineralogist. 93 (2008) 1486–1492. https://doi.org/10.2138/am.2008.2873.

[4] J.W.E. Drewitt, S. Jahn, V. Cristiglio, A. Bytchkov, M. Leydier, S. Brassamin, H.E. Fischer, L. Hennet, The structure of liquid calcium aluminates as investigated by neutron and high-energy x-ray diffraction in combination with molecular dynamics simulation methods, Journal of Physics Condensed Matter. 24 (2012) 099501. https://doi.org/10.1088/0953-8984/24/9/099501.

[5] S. Indris, P. Heitjans, H.E. Roman, A. Bunde, Nanocrystalline versus Microcrystalline Li_2O:B_2O_3 Composites: Anomalous Ionic Conductivities and Percolation Theory, Phys Rev Lett. 83 (2000) 2889–2892. https://doi.org/doi.org/10.1103/PhysRevLett.84.2889.

[6] S. Samal, Synthesis of TiO2 Nanoparticles from Ilmenite Through the Mechanism of

Vapor-Phase Reaction Process by Thermal Plasma Technology, J Mater Eng Perform. 27 (2018) 2622–2628. https://doi.org/10.1007/s11665-017-3060-5.

[7] M.T. Swihart, Vapor-phase synthesis of nanoparticles, Curr Opin Colloid Interface Sci. 8 (2003) 127–133. https://doi.org/10.1016/S1359-0294(03)00007-4.

[8] Y. Wang, B.-I. Min, M. Tanaka, T. Watanabe, Formation Mechanism of Amorphous Li_4GeO_4 Nanoparticles Synthesized by Induction Thermal Plasma for All-Solid-State Batteries. https://doi.org/10.1021/acs.jpcc.3c02465.

[9] Y. Wang, X. Zhang, B.-I. Min, M. Tanaka, T. Watanabe, Synthesis of amorphous Li_3BO_3 nanoparticles as solid electrolyte for all-solid-state battery by induction thermal plasma, J Solid State Chem. (2022) 123775. https://doi.org/10.1016/j.jssc.2022.123775.

[10] W.H.Zachariasen, The atomic arrangement in glass, J. Am. Chem. Soc. 54 (1932) 3841–3851.

[11] P.F. McMillan, W.T. Petuskey, B. Coté, D. Massiot, C. Landron, J.P. Coutures, A structural investigation of CaO-Al_2O_3 glasses via 27Al MAS-NMR, J Non Cryst Solids. 195 (1996) 261–271. https://doi.org/10.1016/0022-3093(95)00536-6.

[12] Q. Guan, X. Chen, T. Gao, C. Xiao, L. Zhao, J. He, X. Long, First-principles study of the structural, electronic, dynamical, and thermodynamic properties of Li_5AlO_4, Journal of Nuclear Materials. 465 (2015) 170–176. https://doi.org/10.1016/j.jnucmat.2015.05.015.

[13] M. Liška, J. Macháče, P. Perichta, O. Gedeon, J. Pilát, Thermochemical modelling and Ab initio molecular dynamics simulations of calcium aluminate glasses, Ceramics - Silikaty. 52 (2008) 61–65.

[14] Q. Hu, L. Lei, X. Jiang, Z.C. Feng, M. Tang, D. He, Li ion diffusion in $LiAlO_2$ investigated by Raman spectroscopy, Solid State Sci. 37 (2014) 103–107. https://doi.org/10.1016/j.solidstatesciences.2014.08.017.

[15] J. Yang, Q. Wang, J. Zhang, O. Ostrovski, C. Zhang, D. Cai, Effect of Al_2O_3/(B_2O_3+ Na_2O) Ratio on CaO-Al_2O_3-Based Mold Fluxes: Melting Property, Viscosity, Heat Transfer, and Structure, Metallurgical and Materials Transactions B: Process Metallurgy and Materials Processing Science. 50 (2019) 2794–2803. https://doi.org/10.1007/s11663-019-01711-z.

[16] P. McMillan, B. Piriou, Raman spectroscopy of calcium aluminate glasses and crystals, J Non Cryst Solids. 55 (1983) 221–242. https://doi.org/10.1016/0022-3093(83)90672-5.

[17] M.H. Brooker, J.B. Bates, Raman and infrared spectral studies of anhydrous Li_2CO_3 and Na $_2CO_3$, J Chem Phys. 54 (1971) 4775–4787. https://doi.org/10.1063/1.1674754.

[18] M. Licheron, V. Montouillout, F. Millot, D.R. Neuville, Raman and ^{27}Al NMR structure investigations of aluminate glasses: (1 - X) Al_2O_3 - x MO, with M = Ca, Sr, Ba and 0.5 < x < 0.75), J Non Cryst Solids. 357 (2011) 2796–2801. https://doi.org/10.1016/j.jnoncrysol.2011.03.001.

[19] P. Unifantowicz, S. Vaucher, M. Lewandowska, K.J. Kurzydłowski, Structural changes of silicon upon high-energy milling investigated by Raman spectroscopy, Journal of Physics Condensed Matter. 20 (2008). https://doi.org/10.1088/0953-8984/20/02/025205.

[20] M. Tatsumisago, M. Takahashi, T. Minami, M. Tanaka, N. Umesaki, N. Iwamoto, Structural Investigation of Rapidly Quenched Li_2O-B_2O_3 Glasses by Raman Spectroscopy, Yogyo Kyokai Shi/Journal of the Ceramic Society of Japan. 94 (1986) 464–469.

https://doi.org/10.2109/jcersj1950.94.1089_464.

[21] M.A. Kale, C.P. Joshi, S. v. Moharil, Combustion synthesis of some compounds in the Li_2O-Al_2O_3 system, International Journal of Self-Propagating High-Temperature Synthesis. 21 (2012) 19–24. https://doi.org/10.3103/S1061386212010062.

[22] E.T. Kang, S.J. Lee, A.C. Hannon, Molecular dynamics simulations of calcium aluminate glasses, J Non Cryst Solids. 352 (2006) 725–736. https://doi.org/10.1016/j.jnoncrysol.2006.02.013.

[23] M. Shigeta, T. Watanabe, Numerical analysis for co-condensation processes in silicide nanoparticle synthesis using induction thermal plasmas at atmospheric pressure conditions, J Mater Res. 20 (2005) 2801–2811. https://doi.org/10.1557/JMR.2005.0351.

[24] M. Shigeta, T. Watanabe, Two-directional nodal model for co-condensation growth of multicomponent nanoparticles in thermal plasma processing, Journal of Thermal Spray Technology. 18 (2009) 1022–1037. https://doi.org/10.1007/s11666-009-9316-3.

[25] James G. Speight, Lang's Handbook of Chemistry, Seventeenth, 2017.

[26] H. Sone, T. Kageyama, M. Tanaka, D. Okamoto, T. Watanabe, Induction thermal plasma synthesis of lithium oxide composite nanoparticles with a spinel structure, Jpn J Appl Phys. 55 (2016). https://doi.org/10.7567/JJAP.55.07LE04.

[27] M. Shigeta, T. Watanabe, Effect of saturation pressure difference on metal-silicide nanopowder formation in thermal plasma fabrication, Nanomaterials. 6 (2016). https://doi.org/10.3390/nano6030043.

[28] G. Gutiérrez, B. Johansson, Molecular dynamics study of structural properties of amorphous Al_2O_3, Phys Rev B Condens Matter Mater Phys. 65 (2002) 1–9. https://doi.org/10.1103/PhysRevB.65.104202.

[29] I. Daniel, P.F. McMillan, P. Gillet, B.T. Poe, Raman spectroscopic study of structural changes in calcium aluminate ($CaAl_2O_4$) glass at high pressure and high temperature, Chem Geol. 128 (1996) 5–15. https://doi.org/10.1016/0009-2541(95)00159-X.

Table 4.1. Experimental conditions for induction thermal plasma system.

Parameter	Condition
Input power [kW]	20
Pressure [kPa]	101.3
Frequency [MHz]	4
Sheath gas rate [L/min]	60 (Ar+O_2)
Inner gas rate [L/min]	5 (Ar)
Carrier gas rate [L/min]	3 (Ar)
Quenching gas rate [L/min]	0, 10, 20 (Ar)
Feed rate [mg/min]	300
Ar/O_2 molar ratio [-]	57.5:2.5
Li/Al molar ratio [-]	5:1, 5.25:1, 5.75:1

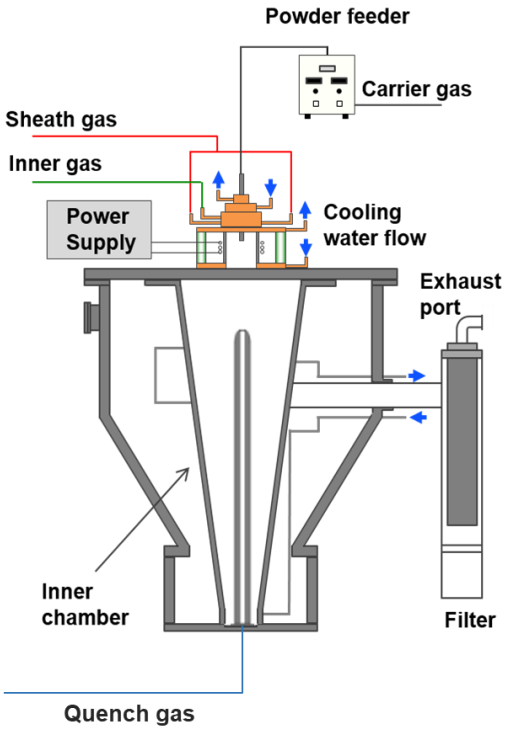

Fig. 4.1. Schematic diagram of amorphous Li_5AlO_4 synthesized by induction thermal plasma.

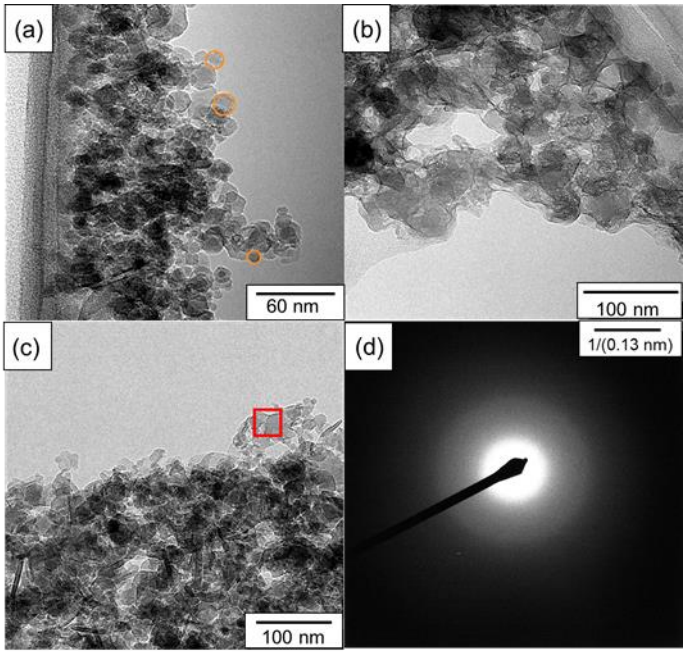

Fig. 4.2. TEM photographs of products synthesized by different quenching gas flow rates (a) 0 L/min, (b) 10 L/min, (c) 20 L/min. The red square is the focus of the electron beam on product. The corresponding diffraction pattern is shown in (d).

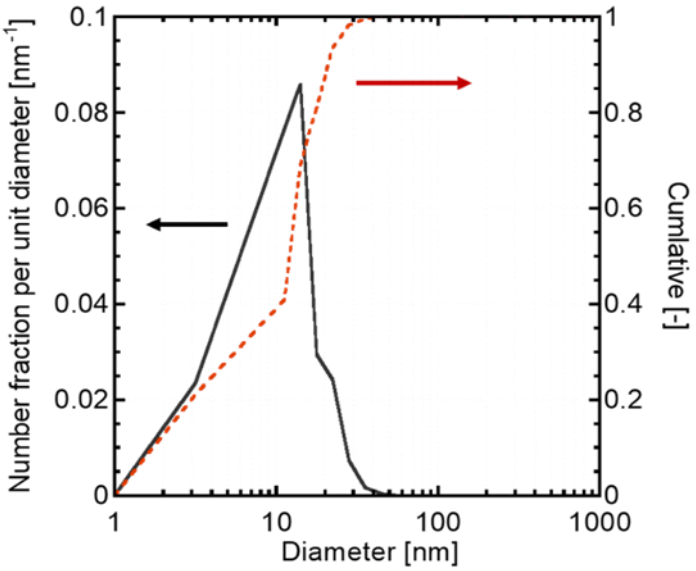

Fig. 4.3. Diameter distributions of products synthesized without quenching gas flow. Inserts indicate the average diameters of products estimated by countering more than 200 different particles.

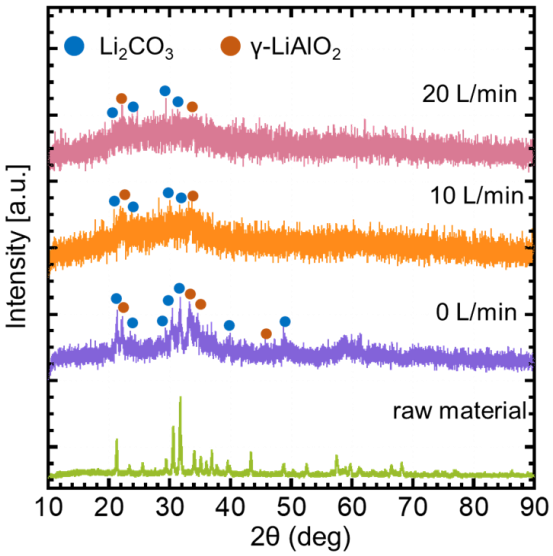

Fig. 4.4. XRD spectra of products synthesized by different quenching gas flow rates. Blue round, yellow round and orange square represent Li_2CO_3, Al_2O_3 and γ-$LiAlO_2$, respectively.

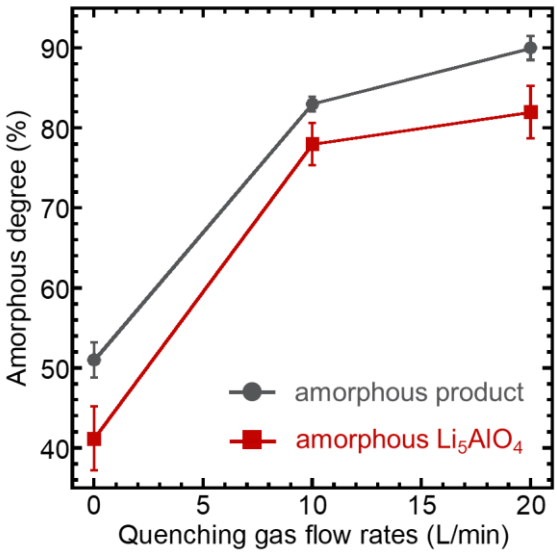

Fig. 4.5. Estimated amorphous degree of collected particles and Li_5AlO_4 synthesized by different quenching gas flow rates. The error bars represent the standard errors of the corresponding average.

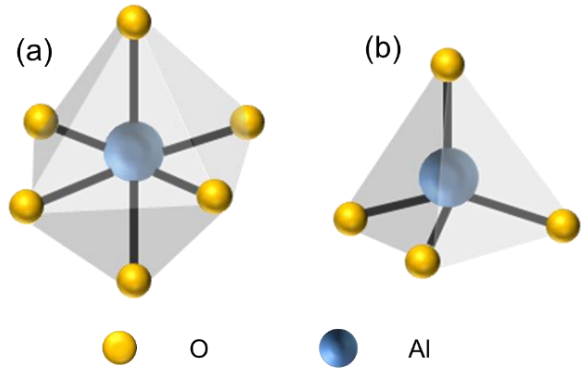

Fig. 4.6. Schematic diagram of (a) [AlO_6] octahedron and (b) [AlO_4] tetrahedron.

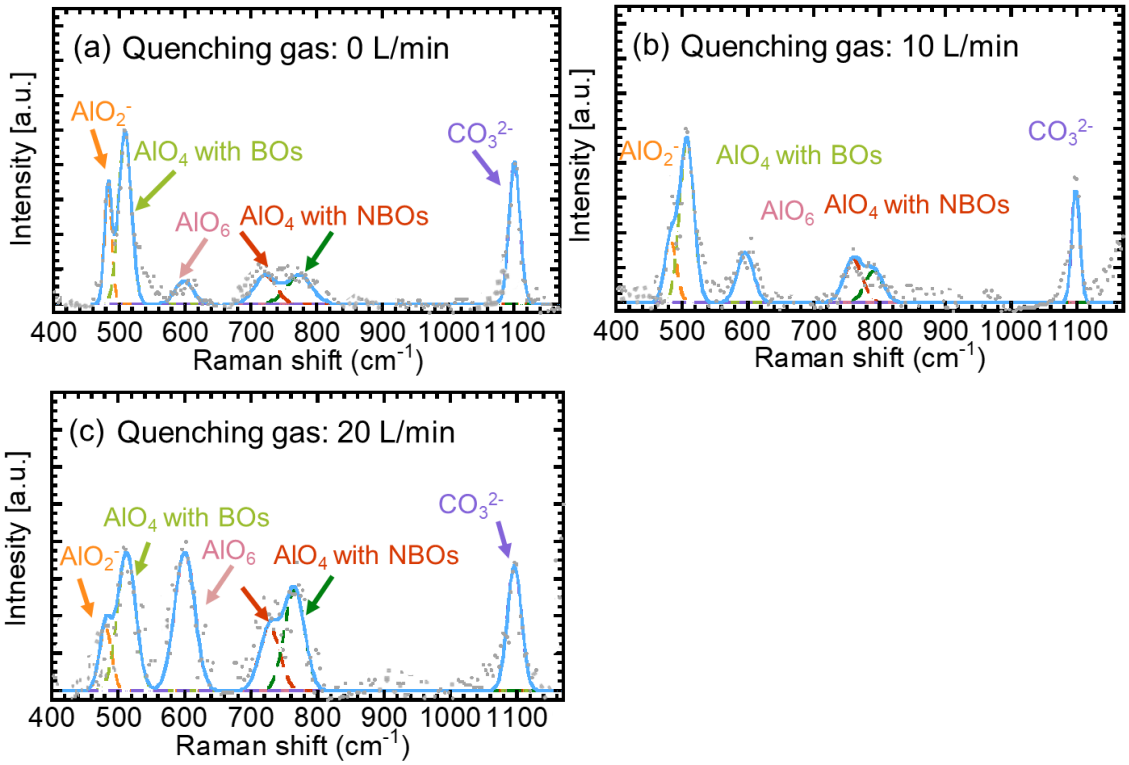

Fig. 4.7. Raman spectra of products synthesized by different quenching gas flow rates. (a) 0 L/min, (b) 10 L/min, (c) 20 L/min. Gray dots line is the experimental results, the blue line is the cumulative fitting.

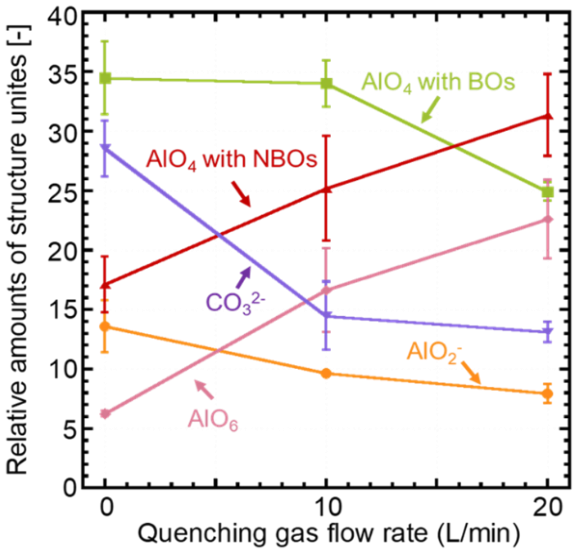

Fig. 4.8. The relative amounts of different aluminate units and CO_3^{2-} in products synthesized by different quenching gas flow rates. The error bars represent the standard errors of the corresponding average.

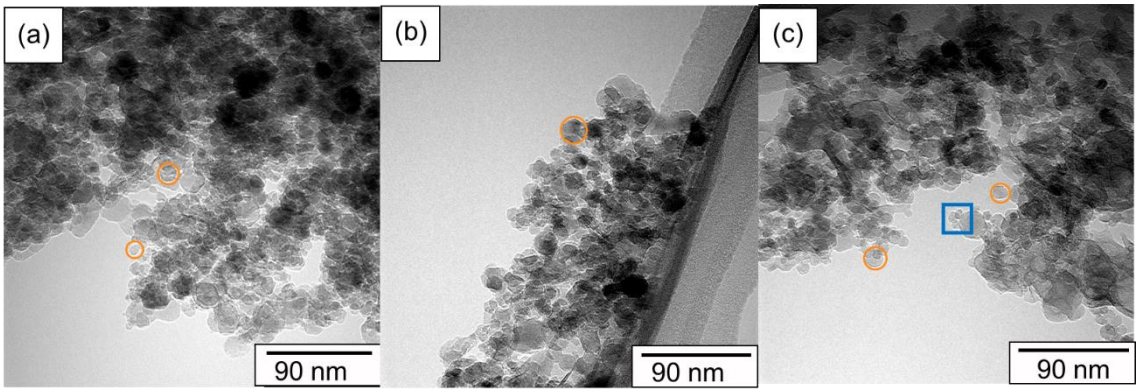

Fig. 4.9. TEM photographs of products synthesized by different Li content in raw material (a) Li:Al = 5:1, (b) Li:Al = 5.25:1, (c) Li:Al = 5.75:1.

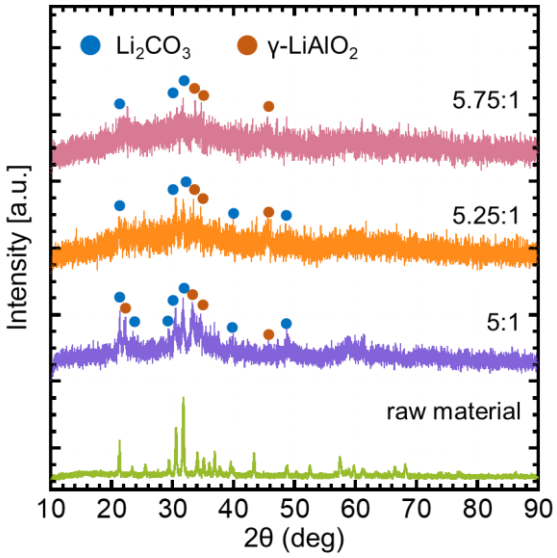

Fig. 4.10. XRD spectra of products synthesized by different Li contents in raw material. Blue round, yellow round and orange square represent Li_2CO_3, Al_2O_3 and γ-$LiAlO_2$, respectively.

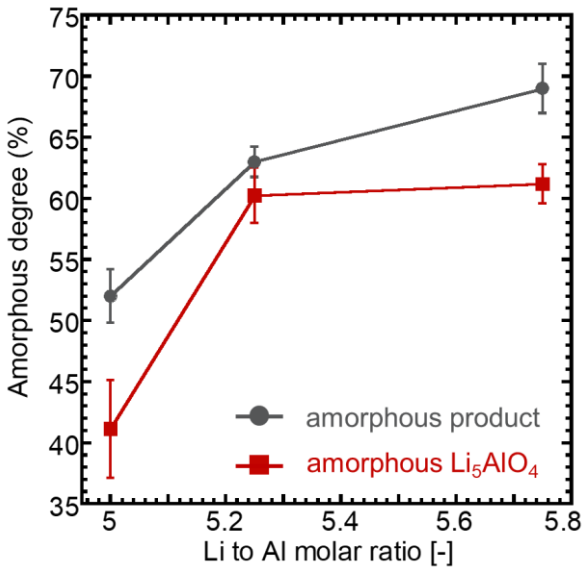

Fig. 4.11. Estimated amorphous degree of collected particles and Li_5AlO_4 synthesized by different Li content in raw material. The error bars represent the standard errors of the corresponding average.

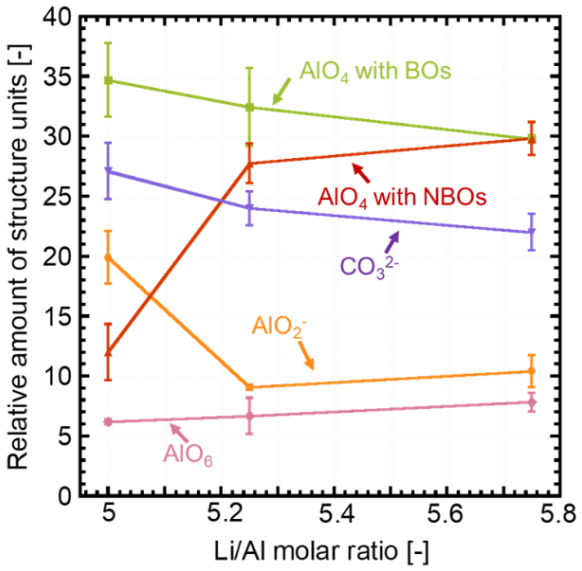

Fig. 4.12. The relative amounts of different aluminate units and CO_3^{2-} in products synthesized by different Li contents in raw material. The error bars represent the standard errors of the corresponding average.

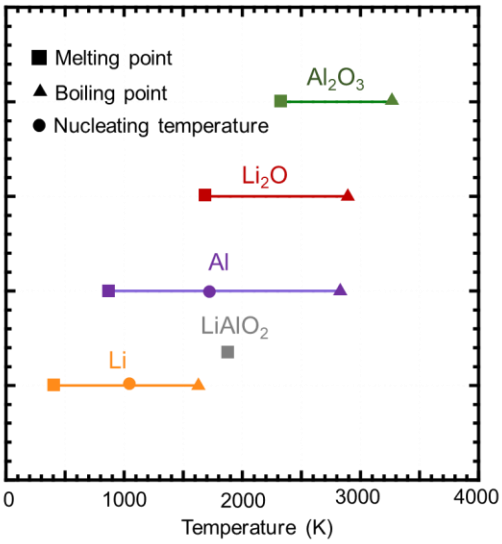

Fig. 4.13. The melting, boiling, and nucleation temperature of Al, Li, and oxides.

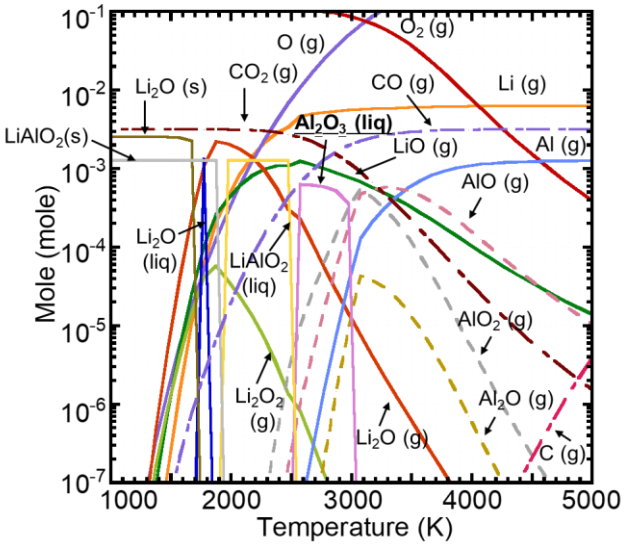

Fig. 4.14. Thermal equilibrium of the Li-Al-O system. Feeding rate is 300 mg/min with Li/Al molar ratio 5/1, Ar/O_2 molar ratio is 57.5/2.5.

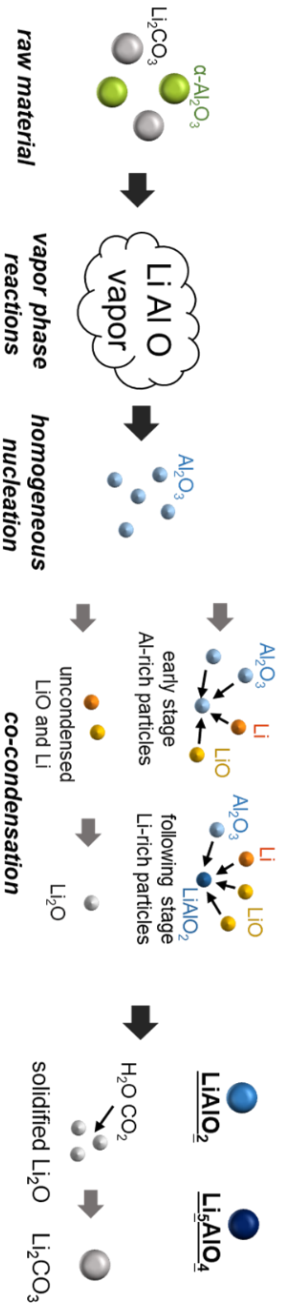

Fig. 4.15. Formation mechanism of lithium aluminate nanoparticles synthesized by induction thermal plasma.

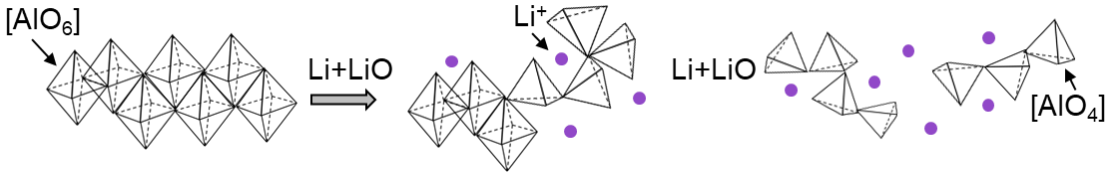

Fig. 4.16. Aluminate unit transformation process with O/Al molar ratio increase in amorphous lithium germanate.

5. Formation Ability of Amorphous Nanoparticles with High Li Content

Amorphous Li_3BO_3, Li_4GeO_4, and Li_5AlO_4 nanoparticles were synthesized successfully by induction thermal plasma. Since the physical and chemical properties of elements in three systems are different, further leading to the vapor reactions, nucleation phase, condensation phase, structure unit transformation and time lag of condensation are different. A huge discrepancy was observed in the experiment results of three systems at the same experiment conditions. The reason for this discrepancy should be studied in order to summarize the formation ability of amorphous nanoparticles synthesized by induction thermal plasma. The formation ability can be discussed from structure and chemical composition because the target materials possess amorphous structure and high Li content simultaneously in this experiment.

This chapter mainly focuses on investigating the formation ability of amorphous nanoparticles with high Li content. The formation ability was discussed from amorphous structure and chemical composition of products, based on summarization and comparison of the experiment results of three systems.

5.1 Summarized Experiment Results of Three Systems

Figure 5.1 (a)-(c) shows the summarized experiment results for Li-B-O, Li-Ge-O, and Li-Al-O systems. This result is obtained with the following experiment conditions. Raw material molar ratio of Li and glass former atom is stoichiometric with target material, sheath gas is the mixture of Ar and O_2 with molar ratio of 57.5:2.5, no quenching gas injection during plasma process.

Figure 5.1 (a) displays the amorphous degree of products in three systems. The Li-B-O system is the most easily to form amorphous nanoparticles among three systems, around 60% of product exist as amorphous structure. The amorphous degree of target compound for three systems is presented in **Fig. 5.1 (b)**, only around 20% of amorphous target compound is obtained in Li-Ge-O, showing the lowest value among the three systems. The Li-Al-O system occupies the highest

value in amorphous degree of target compound, although the Li-B-O system has a higher amorphous product degree. This phenomenon demonstrates more amorphous by-products existing in Li-B-O system. Chemical composition in products is also compared, and the result is shown in **Fig. 5.1 (c)**. The Li-Ge-O shows the highest uniformity in product chemical composition, around 90% of product is the target compound although most of them exist as crystalline.

5.2 Formation Ability of Amorphous Structure

5.2.1 Effect of Li content

The basic unit of network of amorphous nanoparticles is the oxide polyhedron which consists of a center atom and oxygen atoms. The center atom is usually glass former. These polyhedrons are connected randomly and disorderly by corner to form the network. The relative orientations between corner-shared polyhedrons vary within a wide range, which results in the long-range order absence in amorphous material [1]. Term topological disorder is used to describe such network structure, that is, the structure of amorphous material lacks periodic and orientational order in the long-range [2]. In addition, the polyhedrons that consisting network are regular, congruent and rigid due to the short-range order in amorphous [3]. Cations locate in the holes of topologically disorder networks, the cation refers to lithium in this dissertation. An illustration of topological disorder network is presented in **Fig. 5.2**.

Connectivity and network structure are broken gradually through nucleophilic substitution with lithium oxide addition, further, the amorphous structure is destroyed. [4]. **Figure 5.3** presents the process of breakdown of the bridge oxygen BO bond by nucleophilic substitution. Since the electronegativity between glass former and oxygen in polyhedron is different, the electronic cloud is closer to the oxygen atom. The chemical bond in polyhedrons is polar covalent bond. This phenomenon leads to the glass former atom showing positive valence and the oxygen showing negative valence. Lithium oxide as an ionic compound consists of Li^+ and O^{2-}. The O^{2-} in Li_2O more easily offers electrons for glass former compared to O in polyhedron. The glass former atoms are attacked by O^{2-} of Li_2O with Li_2O addition. A new bond between glass former and O^{2-} in Li_2O is formed, then a BO bond and a Li-O bond are broken. The leaving Li^+ combines with

leaving polyhedron to form a new ionic bond to achieve the system charge balance.

The material tends to form crystalline gradually with Li_2O addition due to the number of ionic bonds increasing. Because the ionic bond is non-directional, the activation energy of crystallization is low. Hence, crystal formation ability is enhanced with Li_2O content increasing, the compound with high Li content prefers to form crystalline structure. The rapid quenching rate can prevent the crystallization process and the amorphous structure is obtained in products.

5.2.2 Effect of Bond Strength

Maintenance of topological disorder network with Li_2O addition benefits synthesis of amorphous according to previously discussed. Namely, a strong network can decrease the fragility of amorphous.

The network skeleton is constructed by oxide polyhedrons. The strong bond allows the network to be rigid, and the system maintains a higher level of connectivity after Li_2O addition [5]. This situation leads to the molten occupying high viscosity, further impeding the diffusion of molecules in molten and enhancing the activation energy of crystallization. Amorphous nanoparticles with high Li content can be synthesized under above conditions. Thus, the bond strength is an index to describe the formation ability of amorphous structure.

Table 5.1 summarizes the polyhedrons and corresponding bond strength in three systems. The B-O bond in [BO_3] triangle occupies the highest value of 498 kJ/mol, a slightly lower value of 423 kJ/mol is observed in Al-O bond in [AlO_4] tetrahedron, while the Ge-O bond in [GeO_4] tetrahedron has an obviously lower bond strength of 340 kJ/mol [6,7]. This phenomenon indicates the topological disorder network in Li-Ge-O is the most fragile, and more difficult to obtain amorphous at the same quenching rate contrasted to Li-B-O and Li-Ge-O. The order of bond strength corresponds to the amorphous degree of collected powder.

5.2.3 Effect of Degree of Freedom

Since amorphous is characterized by topologically disorder, amorphous formation ability can be described as degrees of freedom of the infinite large network with topologically disordered [2].

This network should be composed of oxide polyhedrons connected by corners, edges, or faces.

Since the constraints of polyhedron rigidity and the requirement of connectivity at the vertices are severe, the topologically disordered network is difficult to achieve infinitely large. The net degree of freedom, *f*, per vertex is introduced to describe amorphous formation ability for different systems. The net degree of freedom per vertex is given by the discrepancy between network dimension, *d*, and number of constraints per vertex, *h*, based on the rigidity and connectivity of polyhedrons, and is expressed in **Equation 5.1**. Topologically disorder network with infinite large is constructed when *f* is nonnegative, that is, the amorphous structure can be obtained with nonnegative *f*.

$$f = d\text{-}h \tag{5.1}$$

here, the number of constraints per vertex *h* is given by

$$h = \delta V\text{-}\frac{\delta(\delta+1)}{2} \tag{5.2}$$

where δ is the dimensionally of polyhedrons, *V* is vertex number of per polyhedrons. The number of polyhedrons sharing a vertex, *C*, is referred to as the connectivity of network. Since the connectivity of vertexes is dependent on the number and types of connected polyhedrons. As previously discussed, there is only one kind of polyhedron in every system. Therefore, the *f* can be expressed by

$$f = d\text{-}C\left\{\delta\text{-}\left[\frac{\delta(\delta+1)}{2V}\right]\right\} \tag{5.3}$$

The state of system can be classified into three types according to the value of *f* [8]. If $f < 0$, the system is overconstrained and cannot form topologically disordered network. Because additional rigidity would result in localized stress, crystalline order is rapid arranged aiming to eliminate the localized stress. Isostatic state is achieved when $f = 0$, system is optimally constrained, meaning the system is rigid but free of stress. The condition for amorphous formation will be optimal when the network is isostatic. The system would gradually transform to floppy state with value of $f > 0$, the system shows disorder due to lack of constraints and the disordered structure can be maintained by the rapid quenching rate. However, the lack of constraints allows the atoms tend to arrange themselves into the crystalline order with minimum energy. Hence, the topologically

disordered network arrives in infinite large when value of *f* is nonnegative.

Table 5.2 presents the estimated results for Li-B-O, Li-Ge-O, and Li-Al-O systems. The Li-B-O system owns higher possibility to build topologically disordered network with infinite large contrasted to Li-Ge-O and Li-Al-O system. Hence, the Li-B-O system occupies the high amorphous degree of the collected powder among three systems at the same quenching rate.

5.2.4 Effect of Configuration Entropy

The structure discrepancy between melt and solid is another factor to amorphous formation ability. Amorphous more easily form in a region which there is an obvious configuration entropy between melt and solid. The increased configuration entropy can rise the energy barrier for crystallization, allowing the system to tend to form amorphous [9].

An enhanced amorphous formation ability is observed near the eutectic point in various systems [10]. There is a structure competition exist around eutectic point, and the higher configuration entropy is achieved. The enhanced crystallization energy barrier in the region near the eutectic point impairs crystallization and benefits amorphous formation. In addition, the large configuration entropy can decrease the melt fragility and amorphization dynamic becomes higher, which contributes to acquire amorphous [11]. Therefore, amorphous formation ability is increased near the eutectic point.

The phase diagram of Li-B-O, Li-Ge-O, and Li-Al-O systems is presented in **Fig. 5.4** [12,13]. The Li_5AlO_4 is near the eutectic point while the Li_3BO_3 is far away from the eutectic point. The amorphous Li_5AlO_4 is more easily obtained compared to amorphous Li_3BO_3 at the same quenching rate based on the configuration entropy viewpoint. In addition, the amorphous Li_5AlO_4 can be fabricated by the twin roller quenching method, while amorphous Li_3BO_3 cannot be obtained [14,15]. This situation also indicates the amorphous Li_5AlO_4 owns the lower critical quenching rate contrast to amorphous Li_3BO_3, and provides the powerful evidence to configuration entropy viewpoint.

5.3 Formation Ability of Li-containing Compounds

5.3.1 Effect of Condensation Time Lag

Synthesis of nanoparticles by induction thermal plasma is a bottom to top approach. The complete decomposition of raw material leads to various chemical reactions during plasma process compared to other synthesis methods. The compounds are majorly synthesized during co-condensation process according to formation mechanism. Namely, the chemical composition of product is mainly controlled by condensation during plasma process.

The products tend to own a uniform chemical composition when the time lag of condensation is small [16,17]. Condensation is driven by supersaturation ratio. There is a discrepancy among the various vapors in condensation rate at the same temperature because of the different supersaturation ratios [18]. The high supersaturation ratio of vapor leads to rapid condensation rate, further promoting more vapor to take part in chemical reactions. This dominant state will be replaced by the reduction in the supersaturation ratio caused by continued consumption and the attainment of supersaturation by other vapors. New chemical reactions will also replace the original ones. Hence, diverse compounds would be detected in the final product. The short time lag of condensation allows simultaneous condensation to occur among various vapors, the product consisting of the uniform compound is obtained due to the single chemical reaction.

The co-condensation starts as soon as nuclei are generated and terminated by the solidification of each species. **Figure 5.5** displays the condensation process of Li-B-O, Li-Ge-O, and Li-Al-O system, indicating the temperature ranges of co-condensation are 1700 K-1000 K, 1700 K-1300 K, and 3000 K-1700 K for Li-B-O, Li-Ge-O, and Li-Al-O systems, respectively. The shortest temperature range is occupied by Li-Ge-O system, indicating the Li-Ge-O system has the shortest time lag of condensation. This situation contributes to simultaneous condensation among different vapors, and uniform product is obtained. The chemical composition of Li-Ge-O system product would have the highest uniformity among three systems, which is corresponding to experiment result shown in **Fig. 5.1 (c)**.

5.3.2 Effect of Structure Unit Transformation

Figure 5.1 (a)-(c) reveals that more amorphous by-products exist in product in Li-B-O system

This situation can be explained by the structure unit transformation during condensation. Lithium content in a system affects the structure units that build the compounds. Since the target compounds in three systems contain the highest Li content in the corresponding system. The target compounds are all acquired after a series of unit transformation according to the formation mechanism. The unit transformation process for Li-B-O, Li-Ge-O, and Li-Al-O systems is presented in **Fig. 5.5**. The Li_3BO_3 is synthesized after a complex series of borate unit transformation with Li_2O increase. Borate units exist in the order of BO_2^-, $B_4O_9^{6-}$, $B_2O_5^{4-}$ to BO_3^{3-} with Li_2O addition. The Li_5AlO_4 is synthesized after experiencing the aluminate transformation from $[AlO_6]$ octahedron to $[AlO_4]$ tetrahedron with Li_2O increase. There is no structure unit transformation in Li-Ge-O system.

The rapid quenching rate results in parts of Li_2O solidification before condensation, the intermediates are synthesized due to the incomplete unit transformation. These intermediates are solidified by the rapid quenching rate and exist as by-products. The complex transformation in the Li-B-O system enhances the possibility of intermediates synthesis. The unit transformation process is accompanied by the old chemical bond breakdown and new chemical bond formation. The higher bond energy of B-O also increases the energy barrier for structure unit transformation. In addition, the by-products in Li-B-O are more easily to form amorphous compared target compound Li_3BO_3 due to the lower Li content. These by-products exist as amorphous in product, further reducing the amorphous Li_3BO_3 degree. Thus, more by-products were detected in the Li-B-O system.

5.4 Conclusion

The formation ability of amorphous nanoparticles with high Li content synthesized by induction thermal plasma was investigated from the amorphous structure and chemical composition. The topological disorder network is destroyed by nucleophilic substitution with Li_2O addition. Strong bonds contribute to the system forming amorphous structure under high Li content condition. Uniform product is achieved by the system with short time lag of condensation because of the simultaneous condensation of each species. The simple structure unit

transformation during condensation also reduces by-product formation.

Reference

[1] P.K. Gupta, J.C. Mauro, Composition dependence of glass transition temperature and fragility. I. A topological model incorporating temperature-dependent constraints, Journal of Chemical Physics. 130 (2009). https://doi.org/10.1063/1.3077168.

[2] Prabhat K. Gupta, Rigidity, Connectivity, and Glass-Forming Ability, Journal of the American Ceramic Society. 76 (1993) 1088–1095. https://doi.org/10.1111/j.1151-2916.1993.tb03725.x

[3] P.K. Gupta, A.R. Cooper, Topologically disordered networks of rigid polytopes, J Non Cryst Solids. 123 (1990) 14–21. https://doi.org/10.1016/0022-3093(90)90768-H.

[4] S. Wan, S. Zhang, X. Gong, Y. Zeng, S. Jiang, J. You, Structural investigations on two typical lithium germanate melts by: In situ Raman spectroscopy and density functional theory calculations, CrystEngComm. 22 (2020) 701–707. https://doi.org/10.1039/c9ce01512d.

[5] M.T. Dove, M.J. Harris, A.C. Hannon, J.M. Parker, I.P. Swainson, M. Gambhir, Floppy Modes in Crystalline and Amorphous Silicates, Physical Review Letter. 78 (1997) 1070–1073.

[6] K. -H Sun, Fundamental Condition of Glass Formation, Journal of the American Ceramic Society. 30 (1947) 277–281. https://doi.org/10.1111/j.1151-2916.1947.tb19654.x.

[7] V. Dimitrov, T. Komatsu, Average single bond strength and optical basicity of Na_2O-GeO_2 glasses, Journal of the Ceramic Society of Japan. 117 (2009) 1105–1111. https://doi.org/doi.org/10.2109/jcersj2.117.1105.

[8] K.A. Kirchner, J.C. Mauro, Statistical mechanical model of the self-organized intermediate phase in glass-forming systems with adaptable network topologies, Front Mater. 6 (2019). https://doi.org/10.3389/fmats.2019.00011.

[9] J. Russo, F. Romano, H. Tanaka, Glass Forming Ability in Systems with Competing Orderings, Phys Rev X. 8 (2018). https://doi.org/10.1103/PhysRevX.8.021040.

[10] C. Tang, P. Harrowell, Anomalously slow crystal growth of the glass-forming alloy CuZr, Nat Mater. 12 (2013) 507–511. https://doi.org/10.1038/nmat3631.

[11] Binder, Kurt, and Walter Kob. Glassy materials and disordered solids: An introduction to their statistical mechanics. World scientific, 2011.

[12] E.B. Ferreira, M.L. Lima, E.D. Zanotto, DSC method for determining the liquidus temperature of glass-forming systems, Journal of the American Ceramic Society. 93 (2010) 3757–3763. https://doi.org/10.1111/j.1551-2916.2010.03976.x.

[13] Murthy, M. Krishna, and J. Ip. "Studies in germanium oxide systems: I, phase equilibria in the system Li_2O—GeO_2." Journal of the American Ceramic Society 47.7 (1964): 328-331.

[14] M. Tatsumisago, M. Takahashi, T. Minami, M. Tanaka, N. Umesaki, N. Iwamoto, Structural Investigation of Rapidly Quenched Li_2O-B_2O_3 Glasses by Raman Spectroscopy, Journal of the Ceramic Society of Japan. 94 (1986) 464–469. https://doi.org/10.2109/jcersj1950.94.1089_464.

[15] K. Nassau, M. Grasso, A.M. Glass, Quenched glasses in the systems of Li_2O with Al_2O_3, Ga_2O_3 and Bi_2O_3, J Non Cryst Solids. 34 (1979) 425–436. https://doi.org/10.1016/0022-

3093(79)90028-0.

[16] Y. Cheng, M. Shigeta, S. Choi, T. Watanabe, Formation mechanism of titanium boride nanoparticles by RF induction thermal plasma, Chemical Engineering Journal. 183 (2012) 483–491. https://doi.org/10.1016/J.CEJ.2011.12.040.

[17] M. Shigeta, T. Watanabe, Effect of precursor fraction on silicide nanopowder growth under thermal plasma conditions: A computational study, Powder Technol. 288 (2016) 191–201. https://doi.org/10.1016/j.powtec.2015.11.005.

[18] M. Shigeta, T. Watanabe, Effect of saturation pressure difference on metal-silicide nanopowder formation in thermal plasma fabrication, Nanomaterials. 6 (2016). https://doi.org/10.3390/nano6030043.

Table 5.1 Bond energy for Li-B-O, Li-Ge-O and Li-Al-O systems.

Bond (polyhedron)	Bond energy (kJ/mol)
B-O ([BO_3] triangle)	498
Ge-O ([GeO_4] tetrahedron)	340
Al-O ([AlO_4] tetrahedron)	423

Table 5.2 The degree of freedom, *f*, in Li-B-O, Li-Ge-O, and Li-Al-O systems

polyhedron	δ	V	d	C	f
triangle (BO_3)	2	3	2	2	0
	2	3	3	3	0
	2	3	3	2	1
tetrahedron (GeO_4, AlO_4)	3	4	3	2	0
octahedron (AlO_6)	3	6	3	2	-1

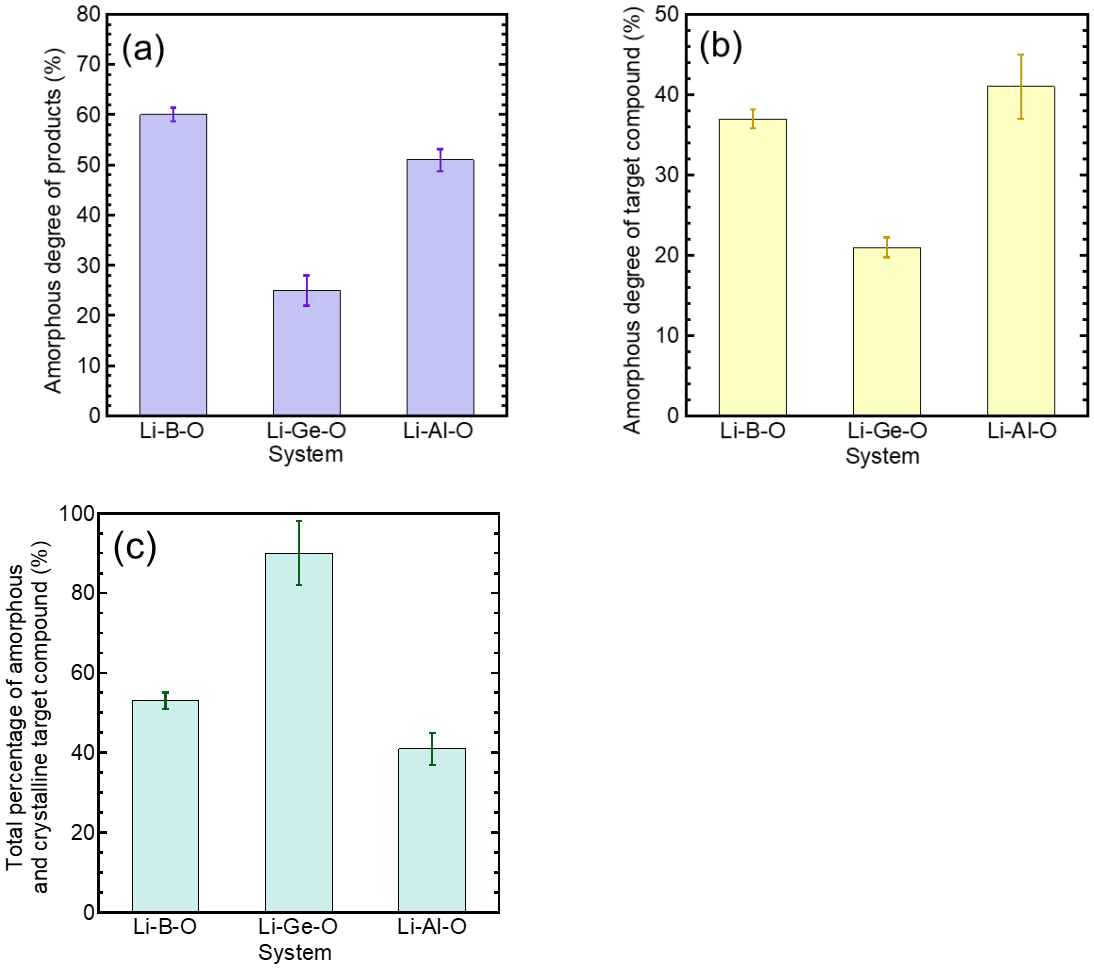

Fig. 5.1. Summarized experiment results for Li-B-O, Li-Ge-O, and Li-Al-O systems. (a) amorphous degree of products, (b) amorphous degree of target compound, (c) total percentage of amorphous and crystalline target compound.

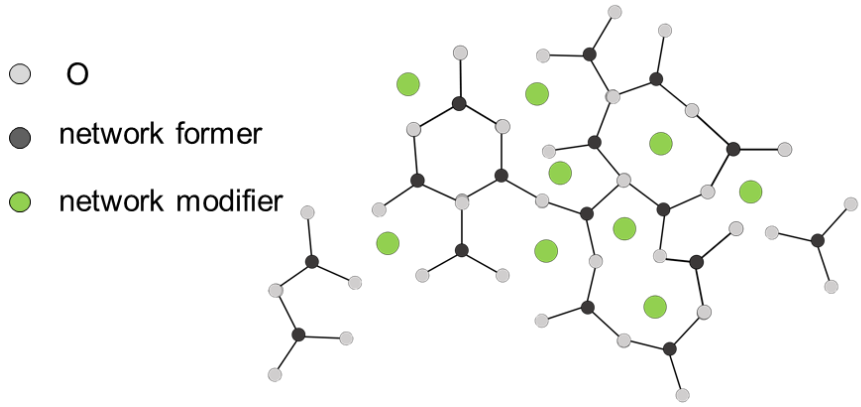

Fig. 5.2. Illustration of topological disorder network.

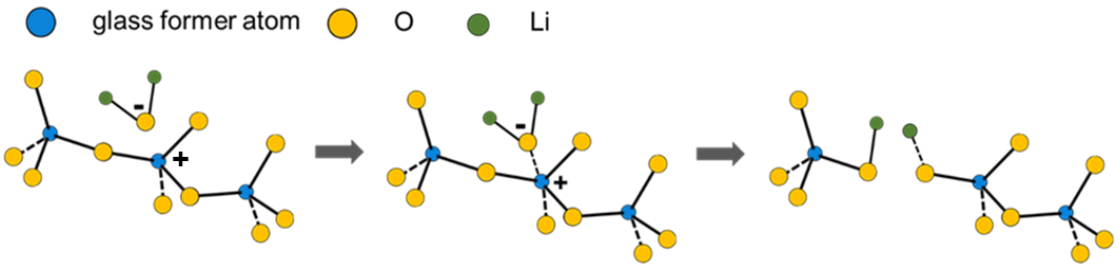

Fig. 5.3. Illustration of bridge oxygen bond breakdown with Li_2O addition.

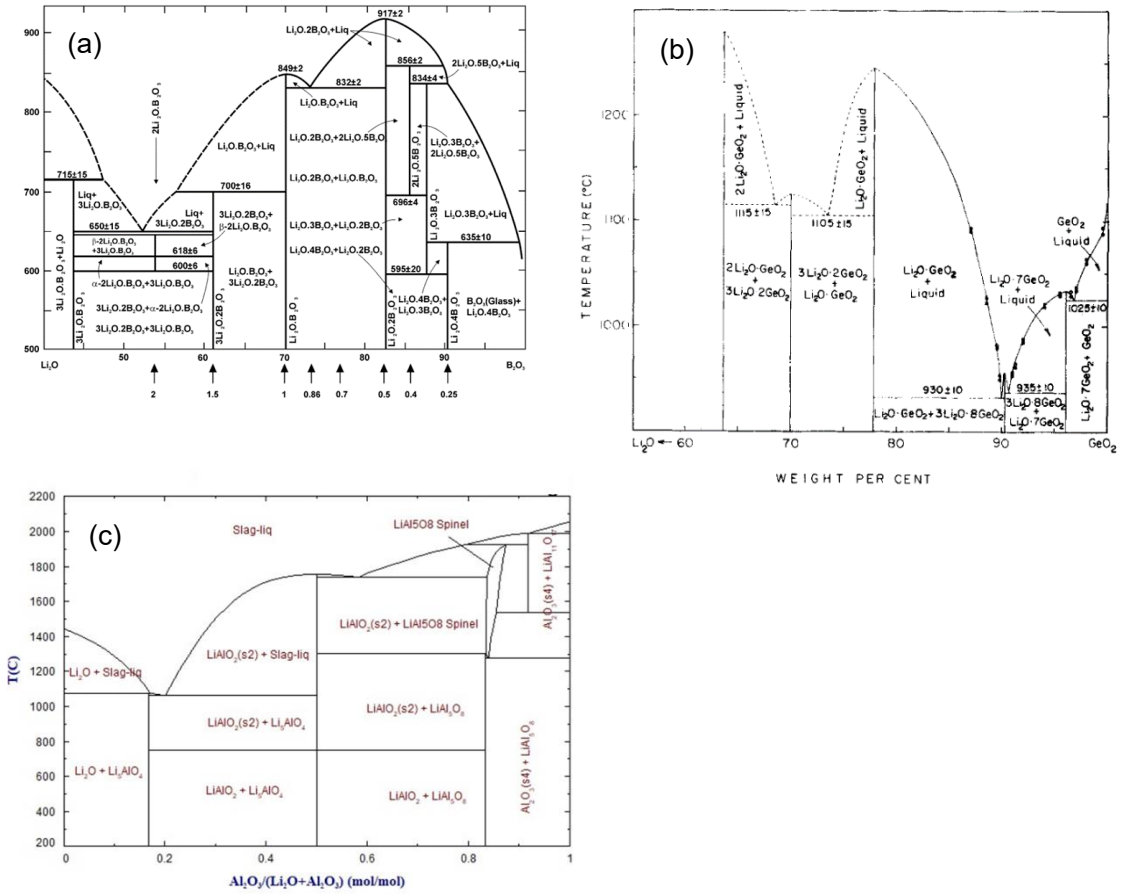

Fig. 5.4. Phase diagram for (a) Li-B-O, (b) Li-Ge-O, and (c) Li-Al-O system.

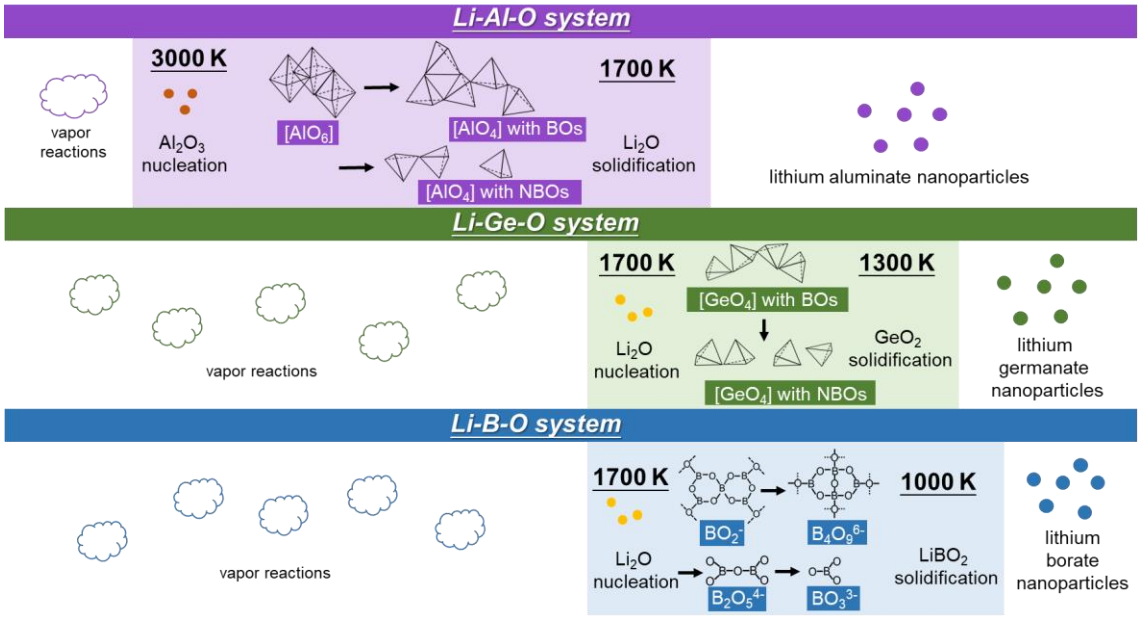

Fig. 5.5. Temperature range and unit transformation process of co-condensation for Li-B-O, Li-Ge-O, and Li-Al-O system.

6. Conclusions

6.1 Summary and Conclusion

This dissertation mainly concentrates on the synthesis of amorphous oxide nanoparticles as solid electrolytes by induction thermal plasma. The amorphous Li_3BO_3, Li_4GeO_4, and Li_5AlO_4 nanoparticles were selected as target material because of the good glass formers and high Li content. Various experiment conditions were implemented aiming to improve product properties. The products were analyzed with different analytic methods to characterize properties, including morphology, size distribution, phase identification, amorphous degree, structure unit distribution. Formation mechanism and experiment condition effect were investigated based on thermodynamic analysis, topological order, structure unit transformation and experiment results. Formation ability of amorphous nanoparticles with high Li content is summarized from the amorphous structure and chemical composition of products. The main conclusion remarks are drawn as follows:

In **chapter 1**, the characteristics and applications of thermal plasma were generally reviewed. All-solid-state battery and related battery materials were also introduced. The superiorities and shortcomings of different solid electrolytes have already been summarized and listed. The stable electrochemical property, sufficient structure defects and nanoscale allow amorphous oxide nanoparticles to outstanding out from other materials for solid electrolytes. However, the conventional fabrication methods for amorphous oxide nanoparticles are complex and time-consuming. Induction thermal plasma is considered an efficient and advanced method, the successful synthesis of various amorphous nanoparticles identified this consideration. Therefore, this dissertation aims to apply RF induction thermal plasma to synthesize amorphous oxide nanoparticles as solid electrolytes for all-solid-state battery.

In **chapter 2**, amorphous Li_3BO_3 nanoparticles were synthesized successfully by RF induction thermal plasma, the oxygen flow rate effect, quenching gas effect and formation mechanism were investigated based on thermodynamic analysis and experiment results. The amorphous Li_3BO_3

degree reaches around 41% and 42% with 5 L/min O_2 and 40 L/min Ar quenching gas, respectively. The sharper temperature gradient is achieved by higher O_2 and quenching gas flow rate. This phenomenon allows smaller size nuclei generation and prevents particles grow orderly, the enhanced amorphous Li_3BO_3 degree is achieved.

Lithium borate nanoparticles are obtained after Li_2O nucleation, Li_2O and $LiBO_2$ co-condensation, and coagulation. Target material Li-rich Li_3BO_3 is mainly synthesized at early stage of condensation after a series of borate unit transformation because of the supersaturation ratio discrepancy between Li_2O and $LiBO_2$. The by-product B-rich $Li_6B_4O_9$ and $Li_4B_2O_5$ are mainly synthesized at the following stage of condensation. Enhanced quenching rate impedes Li_2O condensation and completed borate unit transformation, further resulting in less synthesis of Li_3BO_3.

In **chapter 3**, amorphous Li_4GeO_4 nanoparticles were synthesized through various experiment conditions, including different O_2 flow rates, different Li/Ge molar ratios, different carrier gas, and quenching gas flow rates. The formation mechanism was investigated based on thermodynamic analysis and experiment results. There is a discrepancy in supersaturation ratio of Li_2O and GeO vapor at the same temperature region, the Li-rich Li_4GeO_4 and Ge-rich Li_2GeO_3 nanoparticles are mainly synthesized at early and following stage of condensation, respectively. While the excessive Ge content and quenching rate promote following stage of condensation, resulting in more by-product Li_2GeO_3 formation.

The topological order of prepared nanoparticles was discussed in short-range order (SRO) and intermediate-range order (IRO) based on O-Ge-O and Ge-O-Ge angle distribution, respectively. Increased Ge content and quenching rate contribute to high temperature phase γ-Li_4GeO_4 and amorphous Li_4GeO_4 synthesis. Amorphous Li_4GeO_4 degree is around 65% in 10 L/min quenching gas flow rate. The enhanced quenching rate allows the broaden intratetrahedron O-Ge-O and intertetrahedron Ge-O-Ge angle distribution to be preserved, which achieves more chaos in SRO and IRO. The increased Ge molar amount in raw material also enlarges the intratetrahedron O-Ge-O angle distribution and increases chaos in SRO. The increased disorder in SRO and IRO leads to higher amorphous Li_4GeO_4 degree.

In **chapter 4**, amorphous Li_5AlO_4 nanoparticles were prepared by induction thermal plasma by different quenching gas flow rates and Li/Al molar ratios in raw material. The formation mechanism was studied based on thermodynamic analysis and experiment results. The [AlO_6] octahedron and [AlO_4] tetrahedron transformation and distribution were understood according to O/Al molar ratio and temperature distribution. The Al_2O_3 nuclei occur as soon as the reaction between AlO vapor and AlO_2 vapor starts. The [AlO_6] octahedrons are formed first due to the low O/Al molar ratio. Target material Li-rich Li_5AlO_4 nanoparticles are mainly obtained at following stage of condensation with continued LiO condensation after aluminate transformation from [AlO_6] to [AlO_4].

Enhanced amorphous Li_5AlO_4 degree was acquired in high quenching rate and Li/Al molar ratio cases. The highest amorphous Li_5AlO_4 degree is around 82% in the 20 L/min quenching gas case. The higher quenching rate and Li/Al molar ratio benefit Li-rich Li_5AlO_4 synthesis due to the promoted LiO condensation. These synthesized Li_5AlO_4 achieve amorphous under rapid quenching rate. However, the transformation time of aluminate unit is shortened by higher quenching rate, resulting in more [AlO_6] octahedrons remaining in products.

In **chapter 5**, the formation ability of amorphous nanoparticles with high Li content synthesized by induction thermal plasma was studied. Amorphous structure and chemical composition of products were discussed to understand formation ability, based on the comparing and summarizing experiment results of Li-B-O, Li-Ge-O, and Li-Al-O systems. The amorphous nanoparticles are more easily obtained in a system containing strong chemical bonds. The topological disorder network in amorphous material is destroyed by nucleophilic substitution with Li_2O continued addition. The strong bonds in a system can resist the Li_2O attack, and decrease the destruction of topological disorder network. The products with higher uniformity are acquired by a system that has shorter condensation time lag and simple structure unit transformation. The short time lag of condensation leads to uniform chemical composition in product due to the simultaneous condensation of each species. The simple transformation of structure unit decreases the occurrence possibility of by-products and benefits target material formation.

In summary, the above experiment results provide a deep understanding for the synthesis of

amorphous oxide nanoparticles with high Li content by induction thermal plasma from the points of formation mechanism, experiment conditions effect and raw material property. This dissertation offers an advanced and efficient fabrication method for solid electrolytes and promotes the development of ASSBs with high-performance.

6.2 Future Works

Amorphous oxide nanoparticles were synthesized as solid electrolytes by induction thermal plasma in this dissertation, some improvements are put forward as follows aiming to elevate solid electrolytes development.

6.2.1 Decrease By-product Formation

The experiment results reveal the enhancement of amorphous degree accompanied by more by-product synthesis in Li-B-O and Li-Ge-O systems. The deeper study of operation parameters should be implemented in order to higher purity products. New attempts can be tried, such as adjustment of the ratio of tangential and radial gas flow rate in sheath gas. The plasma shape can be changed with different ratio values, which further affects temperature distribution in chamber. Other types of sheath gas are also considered as another improvement direction because the different thermal conductivity also leads to temperature distribution diversification.

The agglomerates were obtained in current experiments, which results in difficulty estimating diameter distribution. The rapid coagulation among nanoparticles causes agglomerate formation. New quenching gas configuration, such as radial-top quenching and radial-bottom quenching, can be attempted.

6.2.2 Effect of Mix Glass Former

High Li ion conductivity is a significant requirement for the high-performance solid electrolyte. The introduction of another type of glass former into system can increase the ion conductivity obviously. Heteroatom bonds would be formed in the system after the introduction of another glass former, which allows more BOs to occur. The formation of BOs bond can provide ionic

vacancies for Li ion migration, simultaneously, also can broaden the migration channels of Li ion. The density of amorphous solid electrolyte is reduced and the structure becomes loose, which is beneficial to Li ion migration in the system. In addition, the phase separation also occurs with Li content increase in system. The network that owns higher Li ion conductivity coats on the network with lower conductivity, this situation allows Li ions to migrate easily. Moreover, the enhanced conductivity can be achieved by addition of glass intermediate to lead to the ceramic-glass structure, because the formation of polyhedrons can modify the network.

In the future, the xLi_2O-yB_2O_3-$(1-x-y)GeO_2$ system and xLi_2O-yB_2O_3-$(1-x-y)Al_2O_3$ system can be selected as the target material due to the mixed glass former effect. The glass former effect can be investigated by adjusting the value of x and y according to amorphous degree and product composition, the temperature distribution effect can be investigated by adjusting quenching gas flow rates.

6.2.3 Electrochemical Property

The products in this dissertation are applied as solid electrolytes. The electrochemical property, such as ion conductivity at different temperatures, life-span, impedance, electrochemical stability, interface reactions, and so on, should be understood clearly. Characteristic of the properties of prepared nanoparticles for solid electrolytes through comparing the electrochemical performance, in order to decide the future research direction. Galvanostatic cycling test for the symmetric Li/prepared nanoparticle/Li to investigate the lithium dissolution and deposition to understand the electrochemical stability. Ion conductivity and impedance tests can be carried out by an electrochemical platform.

Acknowledgments

As I write here, my heart is filled with a myriad of emotions. I am grateful to those who have encouraged and supported me during my doctoral career at Kyushu University.

Firstly, I would like to express my sincere gratitude to my supervisor, Dr. Takayuki Watanabe, a Department of Chemical Engineering professor at Kyushu University. He taught me how to study and think, what to innovate and dedicate. He allowed me to make mistakes and gave me opportunities to correct them in research. I gained not only a wealth of knowledge but also advanced concepts under his guidance.

I also really appreciate the valuable suggestions from Dr. Ken Inoue and Dr. Masahiro Kishida, Professors of the Department of Chemical Engineering at Kyushu University, for my Ph.D. thesis revision. I can improve my dissertation with their assistance and constructive suggestions.

I am very grateful to Dr. Manabu Tanaka, Associate Professor of the Department of Chemical Engineering at Kyushu University, for his help in the analysis and discussion of the experiment results. He gave me useful suggestions when my research met troubles although he is very busy.

I also would like to thank members of the RF group, Dr. Xiaoyu Zhang, Mr. Byeong-il Min, Mr. Kaiwen Zhan, and Mr. Kohei Yamashita. I think I cannot finish my experiments without their help, and the time we spent together was happy.

It is necessary to mention that my cordial thanks should be given to all the staff and members of Lab. 5 for their cooperation and help. They gave me lots of help both in research and daily life. Especially, thank to Mrs. Mayumi Matsuzaki, a secretary of our lab, for her warm-hearted helps.

The financial support from the Japan Science and Technology Agency (JST) SPRING, is highly acknowledged.

Finally, my cordial thanks also go to my family and the people who love and care for me and whom I love and care about.

2023.07.03
王 怡冉